# Terrestrial laser scanning for forest monitoring

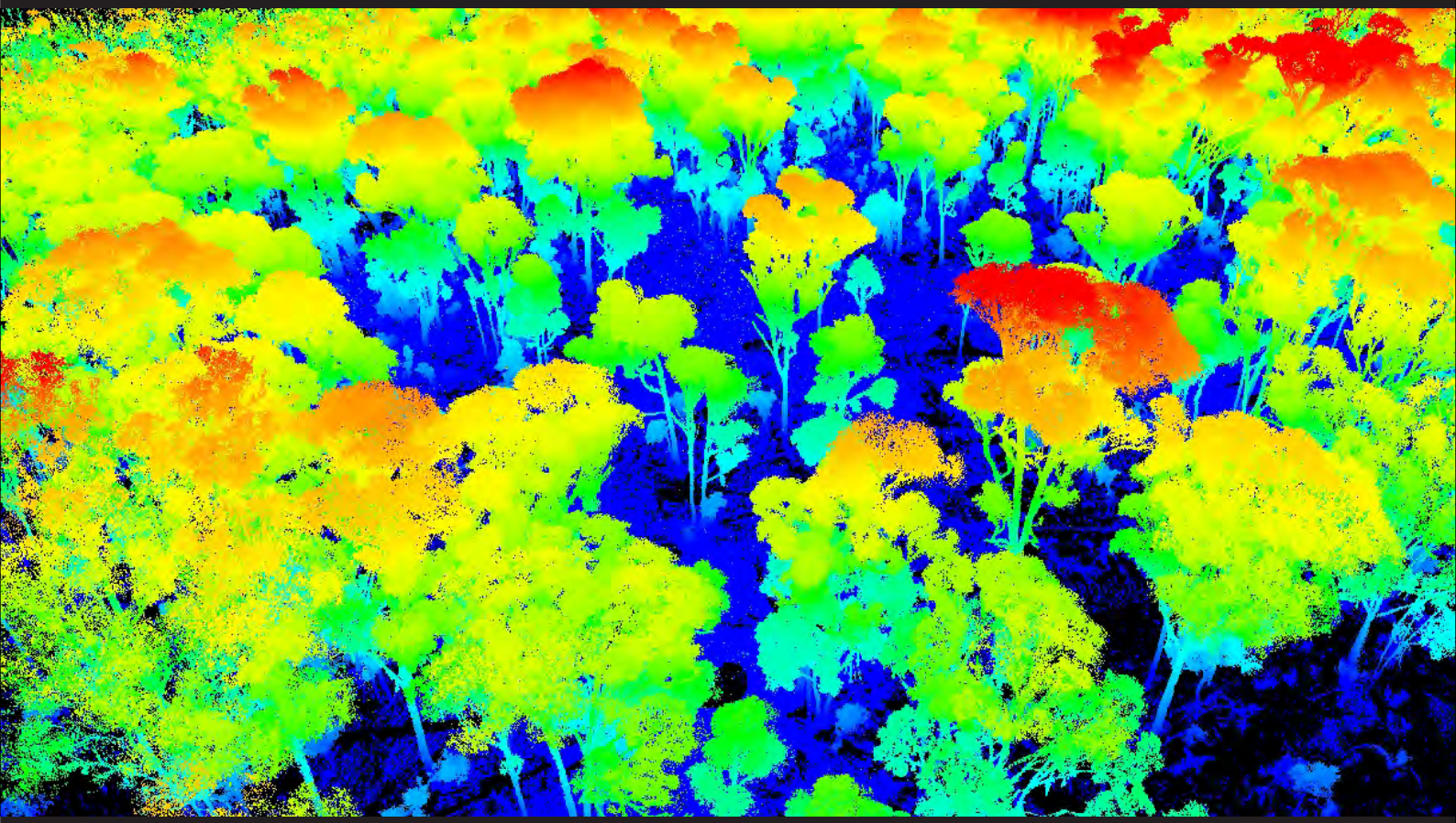

Kim Calders

# Terrestrial laser scanning for forest monitoring

Kim Calders

**Thesis committee**

**Promotor**
Prof. Dr M. Herold
Professor of Geo-information Science and Remote Sensing
Wageningen University

**Co-promotors**
Dr H. Bartholomeus
Assistant Professor, Laboratory of Geo-information Science and Remote Sensing
Wageningen University

Dr J. Verbesselt
Assistant Professor, Laboratory of Geo-information Science and Remote Sensing
Wageningen University

**Other members:**
Prof. Dr L. Poorter, Wageningen University
Prof. Dr A. K. Skidmore, University of Twente, The Netherlands
Prof. Dr B. Muys, KU Leuven, Belgium
Prof. Dr A. H. Strahler, Boston University, United States of America

This research was conducted under the auspices of the C.T. de Wit Graduate School of Production Ecology & Resource Conservation (PE&RC)

# Terrestrial laser scanning for forest monitoring

Kim Calders

**Thesis**
submitted in fulfilment of the requirements for the degree of doctor
at Wageningen University
by the authority of the Rector Magnificus
Prof. Dr M.J. Kropff,
in the presence of the
Thesis Committee appointed by the Academic Board
to be defended in public
on Friday 16 January 2015
at 1.30 p.m. in the Aula.

Kim Calders
Terrestrial laser scanning for forest monitoring
146 pages.

PhD thesis, Wageningen University, Wageningen, NL (2015)
With references, with summaries in English and Dutch

ISBN 978-94-6257-177-8

# Acknowledgements

This PhD thesis has been an amazing journey for me over the past four years. Over the course of my PhD I was fortunate enough to meet a lot of interesting people who gave me different insights into what science and laser scanning is about and, perhaps more importantly, what life outside science is about.

I would first like to express my gratitude to my promoter, Martin Herold. I am very thankful that you gave me the opportunity to undertake this research, and for always ensuring I stayed on track to submit my PhD on time. I am also grateful for your flexibility when it came to work-life balance, especially when that involved me being in Australia for a few months at a time.

To my daily supervisors, Jan Verbesselt and Harm Bartholomeus, thank you for helping me find my way in the scientific world. Harm, I remember how it all started for me at Wageningen when we took the laser scanner for a road trip to Switzerland to see what we could do with this "new toy". Jan, thank you for all the good times, especially during the fieldwork in Hallerbos: tracking phenology in 3D, searching for reflectors with a metal detector and visiting "het kriekske" for lunch.

The foundation for this PhD was laid during my MSc at UCL and I would like to thank Lewis and Mat for their support and guidance, both during my time at UCL and during my PhD. Thanks also to Andy, Aida and Jose for the good times in Gabon. Our campaign was quite ambitious, but we managed to collect an excellent dataset in the end. Pasi, thank you for all the help and patience with converting my point clouds to 3D models and biomass.

This thesis would have never been completed without help from my Australian colleagues. Thank you John, Glenn, Darius and Nick for teaching me all about laser scanning, and for the many good fieldtrips, beers and pies that were part of that process! I'd also like to thank Dan, Christian, Jaz, Kimberly, Anders, Neil, Jacqui and Sally for making me feel like I was part of the team during my research visits.

I was always lucky to have amazing office mates in Wageningen; thanks Daniela, Titia, Nandika, Loïc and Peter! I would also like to thank all my other colleagues in Wageningen for helping me with fieldwork when necessary, giving me advice or having a coffee; thanks

Richard, Roberto, Erika, Noriko, Arun, Laure, Rogier, Maria, Sidney, Johannes, Daniel, Valerie, Ben, Niki, Michi, Sarah, Yang, Brice, Valerio, Juha, Manos, Eliakim, Eskender, Giulia, Hans, Mathieu, Truus, Antoinette, Arnold, Sytze, Lammert, Ron, Jan Clevers, John and Aldo. A special thanks to Philip, for always being creative when I had another practical problem with fieldwork equipment or needed some new reflectors to be designed. Arend, thanks for helping me with the latex layout of the thesis. I would also like to thank my two MSc students, Simone and Tom; I had a good time working with you and your help contributed to my PhD as well.

Thanks to all my friends for the necessary distraction and mental support over the last four years. Ik zou ook graag mijn ouders, en Jelle en Nena bedanken voor hun onvoorwaardelijke steun, niet enkel tijdens mijn doctoraat, maar gedurende de afgelopen 29 jaar. Thanks also to Trisha, Courtney and Jacinta for all the love and support. Finally, I'd like to thank the most important person in my life. Brodie, even though I enjoyed most of my PhD, you made sure that I found the energy to keep going during the difficult moments. You were always there to help me with fieldwork when I couldn't find anyone else and your patience seemed never-ending when I asked you to read through another draft of something related to lasers. It's hard to express all my love and admiration for you in only a few sentences, but know that I couldn't have finished this without you.

# Contents

# Summary

Approximately one third of the world's land area is covered by forest ecosystems. Sir Francis Bacon wrote in 1597: "*ipsa scientia potestas est*" or "*knowledge itself is power*", a quote that is quite relevant to the monitoring of forests. The more we know about these forests, the better the decisions being made by natural resource managers or policy makers regarding forests will be. Monitoring forests is therefore important, and remote sensing data is considered to be one of the key data sources for monitoring these large areas of forests. Data retrieved through optical satellite and airborne remote sensing acquisition methods are a useful tool to obtain information about forest cover and forest land use changes because these data offer a synoptic view over large or inaccessible areas. However, such global satellite remote sensing products are presented in two dimensions only and their use is currently not supported by rapid and robust assessment of accurate ground reference data. Forests are complex ecosystems and the assessment of the full 3D forest structure for monitoring forests is essential.

Terrestrial laser scanning (TLS), also called terrestrial LiDAR (light detection and ranging), is a ground-based method that can retrieve the 3D vegetation structure with millimetre accuracy. It is an active remote sensing technique that can accurately measure distances by transmitting laser energy and analysing the reflected energy as a time or distance resolved signal. The main objective of this PhD thesis is to explore the potential of terrestrial LiDAR for forest monitoring and structural assessment and to develop methods to derive accurate in-situ reference data.

In this research, methods are developed to analyse TLS data to infer the vertical distribution of plant area index (PAI) and plant area volume density (PAVD) at plot level scales, as well as the above-ground biomass (AGB), height and diameter at breast height (DBH) of individual trees. TLS inferred DBH, tree height and AGB are validated against 65 destructively harvested trees and these TLS metrics are also compared with measures from traditional forest inventory data. Furthermore, assumptions made in crown archetypes, typically used in studies about airborne LiDAR, are found to result in significant errors in retrieved crown structural parameters, due to the fact that these assumptions do not correlate with the actual tree structure.

Chapters 2 and 3 use single scan TLS data to quantify and monitor forest structure.

These data are used to derive vertical plant profiles, which describe the plant area as a function of canopy height and characterise the 3D distribution of canopy elements. Chapter 2 demonstrates that not correcting for topography leads to significant errors in the vertical distribution of plant constituents. A local plane fitting approach to correct for topography is introduced and tested in five different Australian forest types. We demonstrate in chapter 3 that TLS measurements with high temporal resolution can effectively monitor spring phenology using PAI derived from vertical plant profiles.

Chapter 4 describes the use of multiple registered TLS scans to explicitly model tree volume using quantitative structure models. AGB is then derived from these volume estimates and basic density information. The main advantage of TLS point clouds over traditional field inventory AGB is the independence from indirect allometric relationships with tree parameters such as DBH and tree height. The key result of this chapter is that the error for TLS AGB estimates is not dependent on DBH, whereas the error for AGB estimates using allometric models increases exponentially with increasing DBH. The latter is not surprising since the performance of allometric models depends on the calibration data and large trees are often under-represented in these calibration data.

Chapter 5 investigates the assumptions of crown archetypes on inferring structural information from large footprint airborne/spaceborne LiDAR. Analytical expressions that describe the interaction of large footprint LiDAR signals with tree structure are formulated. The retrieval of leaf area index (LAI, as a proxy for forest structure) from crown archetypes is evaluated through inversion of the analytical expressions. The performance of the LiDAR signal inversion of realistic tree models is poor, suggesting that crown archetypes do not represent true architecture well. Terrestrial LiDAR provides detailed 3D information and holds large potential as input for realistic scene models using explicit tree models that are not dependent on crown archetype assumptions.

This PhD thesis contributes scientifically to the development and testing of new methods based on terrestrial LiDAR and explores their practical use. The latter is of importance, in particular for monitoring systems for REDD+ as TLS inferred metrics reduce uncertainties in ground reference data. Further testing of these methods in densely (tropical) forested environments is required in order to assess their true operational value.

# Samenvatting

Ongeveer een derde van het landoppervlak op de aarde bestaat uit bosecosystemen. Sir Francis Bacon schreef in 1597: "*ipsa scientia potestas est*" oftewel "*kennis is macht*", een uitspraak die zeer relevant is voor het monitoren van bossen. Een goede kennis over deze bossen is essentieel voor de beslissingen die gemaakt worden door natuurbeheerders of beleidsmakers. Het monitoren van bossen is daarom belangrijk en remote sensing data worden beschouwd als één van de belangrijkste databronnen voor het observeren van uitgestrekte bosgebieden. Optische sensoren aan boord van vliegtuigen of satellieten kunnen nuttige informatie verzamelen over de bosoppervlakte of de veranderingen hierin. Deze sensoren zijn uitermate geschikt om grote of ontoegankelijke gebieden te observeren en verzamelen informatie op globale schaal. Zulke satellietbeelden hebben echter slechts twee dimensies en het gebruik van deze beelden wordt momenteel niet ondersteund door snelle en objectieve metingen van accurate in-situ data. Bossen zijn complexe ecosystemen en het analyseren van de volledige 3D bosstructuur is essentieel voor het monitoren van bossen.

Terrestrische laserscanning (TLS), ook wel terrestrische LiDAR (*light detection and ranging*) genoemd, is een meettechniek die de 3D vegetatiestructuur met millimeter nauwkeurigheid kan opmeten. TLS is een actieve remote sensing techniek die nauwkeurig afstanden kan meten door het uitzenden van laserenergie en het analyseren van de gereflecteerde energie. Het belangrijkste doel van dit proefschrift is om het potentieel van terrestrische LiDAR voor het monitoren van bossen te onderzoeken en om methoden te ontwikkelen voor het afleiden van accurate in-situ referentiedata voor bos monitoring.

In dit onderzoek worden methoden ontwikkeld om TLS data te analyseren voor het berekenen van de verticale verdeling van de plant oppervlakte index (*plant area index*, PAI) en de plant oppervlakte volume dichtheid (*plant area volume density*, PAVD) op plot niveau en de bovengrondse biomassa (AGB), hoogte en diameter op borsthoogte (DBH) van individuele bomen. Boomhoogte, DBH en AGB op basis van TLS data worden gevalideerd met metingen van 65 gekapte bomen en worden vergeleken met traditionele bosinventarisaties. Dit proefschrift onderzoekt verder de aannames die gedaan worden omtrent kroon archetypes, die dikwijls gebruikt worden in LiDAR studies vanuit vliegtuigen en satellieten. Dit onderzoek toont aan dat kroon structuur die afgeleid is op basis van

deze aannames, significant fout kan zijn omdat deze aannames niet overeenkomen met de werkelijke boomstructuur.

In hoofdstuk 2 en 3 worden TLS scandata van één enkele locatie gebruikt voor het kwantificeren van de bosstructuur. Deze gegevens worden gebruikt voor het berekenen van verticale plant profielen, die de plant oppervlakte als functie van hoogte beschrijft en informatie verstrekt over de 3D verdeling van bladeren, takken en stammen. Hoofdstuk 2 toont aan dat het niet corrigeren van topografische effecten leidt tot significante fouten in de verticale distributie van deze plant profielen. Op basis van TLS data wordt het terrein benaderd met een vlak en de topografie gecorrigeeerd in de TLS data. Deze methode is getest in vijf verschillende bostypes in Australië. Hoofdstuk 3 laat zien dat TLS metingen met een hoge temporele resolutie uitermate geschikt zijn voor het opvolgen van fenologische veranderingen in het voorjaar door gebruik te maken van PAI waarden die afgeleid worden uit verticale plant profielen.

Hoofdstuk 4 beschrijft het gebruik van meerdere geregistreerde TLS scans voor het expliciet modelleren van boomvolume met behulp van kwantitatieve structuur modellen. AGB wordt in dit geval berekend op basis van deze volumes en dichtheid. Het belangrijkste voordeel van TLS puntenwolken ten opzichte van meer traditionele AGB inventarisaties is de onafhankelijkheid van indirecte allometrische relaties met boomparameters zoals DBH en hoogte. Het belangrijkste resultaat van dit hoofdstuk is dat de fout voor TLS AGB schattingen niet afhankelijk is van DBH, terwijl de fout voor AGB schattingen op basis van allometrische modellen exponentieel toeneemt voor grotere DBH. Dit is niet verwonderlijk aangezien de prestaties van allometrische modellen afhangt van de kalibratiedata en grote bomen vaak ondervertegenwoordigd zijn in deze kalibratiegegevens.

Hoofdstuk 5 onderzoekt de aannames in kroon archetypes voor het afleiden van boomstructuur met *large footprint* LiDAR sensoren aan boord van satellieten of vliegtuigen. De interactie tussen het LiDAR signaal en de boomstructuur wordt beschreven met analytische vergelijkingen. Het afleiden van de blad oppervlakte index (*leaf area index*, LAI) van kroon archetypes is geëvalueerd op basis van inversie van de analytische vergelijkingen. De prestaties van de LiDAR signaal inversie van realistische boom modellen is ondermaats, wat suggereert dat de kroon archetypes geen goede benadering zijn voor de boomstructuur. Terrestrische LiDAR geeft gedetailleerde 3D-informatie en kan potentieel dienen als input voor realistische expliciete boommodellen die niet afhankelijk zijn van de aannames die gemaakt worden in kroon archetypes.

Dit proefschrift draagt in wetenschappelijk opzicht bij aan de ontwikkeling van nieuwe methoden gebaseerd op terrestrische LiDAR en test hun praktisch gebruik. Dit laatste is belangrijk, bijvoorbeeld voor het monitoren van bossen in REDD+ context omdat TLS metingen de accuraatheid en precisie in referentiedata verhogen. Verder onderzoek van deze methoden in tropische bossen is noodzakelijk om de werkelijke operationele waarde van TLS data te bepalen.

# Chapter 1

# Introduction

## 1.1 Background

Forest ecosystems cover approximately 31% of the world's land area with a total forested area of approximately 4 billion hectares (FAO, 2010). Forests play an important role in today's society and serve as a source for the production of paper products, lumber and fuel wood. In addition, forests produce freshwater from mountain watersheds, purify the air, offer habitat to wildlife and offer recreational opportunities. To keep these productive, ecological and recreational functions balanced, accurate and precise information about forest structure and its biophysical parameters is needed (Warning & Running, 2007).

Many decisions made by natural resource managers or policy makers regarding forests are not linked with the spatial scales covered by conventional forest inventory methods. Remote sensing data is seen as one of the key data sources to fill forest monitoring data gaps that exist, particularly in many developing countries (Romijn et al., 2012). Data retrieved through remote sensing methods, in particular through satellite and airborne acquisition methods, can be a useful tool in obtaining this information because these data offer a synoptic view over large or inaccessible areas. The land usage of approximately 13 million hectares of forest ecosystems worldwide changes annually, making accurate forest monitoring an important task (FAO et al., 2009). About 17% of human induced greenhouse gas emissions are linked to these changes to forest land use, along with other forestry related activities (FAO et al., 2009). Global initiatives such as the Global Forest Resources Assessment (FAO, 2010) support global tree cover and forest land use monitoring. Monitoring programs implement a systematic framework to obtain information about changes in forest cover and forest land use changes on a global scale. The advances in satellite remote sensing allow higher spatial resolution forest cover maps to be produced. The first MODIS VCF (Moderate Resolution Imaging Spectroradiometer Vegetation Continuous Fields) product (Hansen et al., 2003) produced a global tree cover map with a spatial resolution of 500 m. The current MODIS VCF data set produced a global tree cover map at 250 m spatial resolution from 2000 to 2010 (DiMiceli et al., 2011). A global high resolution map of tree cover, loss and gain for the period from 2000 to 2012 at a spatial resolution of 30 m was derived from Landsat data by Hansen et al. (2013). Such high resolution maps provide the means to monitor the changes in forest cover that occur over time. However, the use of such global data sets is currently not supported by rapid and robust assessment of accurate ground reference data of 3D forest structure, nor by biophysical measurements for the monitoring of forest and land dynamics. More objective validation and calibration methods at plot level scales can potentially increase the accuracy of broad-scale monitoring applications.

LiDAR (light detection and ranging) can serve as an excellent tool to assess forest structure and the three-dimensional distribution of plant canopies at plot level and regional scales. It therefore has the potential to reduce uncertainty of in-situ measurements and

has been used in forest inventories since the 1980s (Lim et al., 2003). LiDAR is an active remote sensing method that can accurately measure distances by transmitting laser energy and analysing the reflected energy as a function of time. Ranging can be done by phase differencing or by pulsed ranging. LiDAR systems that apply the phase differencing method continuously emit light and are therefore often referred to as continuous wave (CW) scanners. The transmitted signal from CW scanners is modulated with a trigonometric function to derive the range (Wehr & Lohr, 1999). Numerous studies have utilised CW scanners to asses vegetation structure (Pueschel et al., 2014; Antonarakis, 2011; Balduzzi et al., 2011), but pulsed LiDAR, also called time-of-flight LiDAR, is used most frequently in vegetation studies (Tang et al., 2012; Ni-Meister et al., 2010; Jupp et al., 2009). Range is calculated by accurately measuring the pulse travel time from the transmitter to the intercepted object and back to the receiver of the LiDAR sensor (Jensen, 2007; Wehr & Lohr, 1999). The round trip time of travel, $t_L$, for a LiDAR pulse is:

$$t_L = 2\frac{R}{c} \tag{1.1}$$

where $R$ is the range and $c$ is the speed of light (approximately 3 x $10^8$ m $s^{-1}$). Based on this equation, the distance between the LiDAR sensor and the object can be derived as:

$$R = \frac{1}{2}ct_L \tag{1.2}$$

The incoming LiDAR pulse not only contain information about the range to the intercepted object, but can also provides intensity information, which indicates the strength of the return. In a forest environment, objects with high reflectance values generally refer to woody vegetation components, whereas LiDAR returns from leaves tend to have lower reflectance values (Yang et al., 2013; Yao et al., 2011). Two types of time-of-flight LiDAR systems are commonly used: discrete return and waveform. Discrete return LiDAR measures only a limited number of pulses returning from a particular object. Waveform LiDAR digitises the whole of the return signal and it can therefore provide additional information about the structure of vegetation (Strahler et al., 2008).

LiDAR can operate from spaceborne, airborne or terrestrial platforms, with each platform serving specific forest inventory needs (van Leeuwen & Nieuwenhuis, 2010). Spaceborne and airborne LiDAR can cover large areas and look at the forest ecosystem from above. Large-footprint LiDAR height metrics have, for example, been significantly related to above-ground biomass (AGB) at both footprint and plot levels (Lefsky et al., 2005; Drake et al., 2002). Lefsky et al. (2005) showed that AGB correlated with maximum forest height measures derived from combining large-footprint spaceborne LiDAR, GLAS (Geoscience Laser Altimeter System) onboard ICEsat (Ice, Cloud,and land Elevation Satellite), and SRTM (Shuttle Radar Topography Mission) data. Drake et al. (2002) demonstrated that height metrics derived from LVIS (laser vegetation imaging sensor), a large-footprint airborne LiDAR system, correlated to estimations of AGB across a spectrum of ecosystems

**Figure 1.1:** Illustration of terrestrial LiDAR data in a cylindrical projection. The data was captured in a Hallerbos (Belgium) and coloured according to returned intensity (blue is low intensity, red is high intensity).

ranging from abandoned pasture to dense primary tropical forest. Terrestrial LiDAR, also called terrestrial laser scanning (TLS), is a ground-based remote sensing technique that can retrieve the 3D vegetation structure with millimetre accuracy. Figure 1.1 shows an example of TLS data from a broadleaf forest in Belgium. Although TLS has a limited spatial coverage compared to airborne and spaceborne LiDAR, it has the potential to reduce uncertainties in calibration and validation data for large scale remote sensing products.

The remainder of this chapter describes the framework of the thesis. The following sections present the use of TLS to assess forest structure (section 1.2) and above-ground biomass (section 1.3). Section 1.4 provides an overview on how detailed TLS data can support upscaling to airborne and, potentially, spaceborne LiDAR. In section 1.5, the objectives and research questions are defined and the final section sets out the outline of this thesis.

## 1.2 Quantifying vertical forest structure using TLS

Forest structure impacts the microclimate and closely relates to several biological and physical processes. For example, respiration, transpiration, photosynthesis, carbon and nutrient cycles and rainfall interception heavily depend on the structural arrangement within the forest. The ground-based assessment of forest structure has been done with optical instruments (Parker et al., 1989), and, recently, terrestrial LiDAR instruments. The use of terrestrial LiDAR instruments offers opportunities for an objective assessment

of the forest structure (Hancock et al., 2014). The objective assessment of forest structure is essential for robust and repeatable measurements. This will, for example, improve the monitoring of temporal changes within the forest. Unlike passive optical instruments, LiDAR is not dependent on natural illumination conditions since it is an active instrument. Previous research has presented fully automated and objective methods to quantify forest structure from terrestrial LiDAR data (Newnham et al., 2012a; Lovell et al., 2011a; Jupp et al., 2009; Danson et al., 2007). This is of importance because optical methods, such as hemispherical photography, are more susceptible to methodological errors, which can occur at any stage of image acquisition and analysis (Jonckheere et al., 2004). The LAI-2000 (Li-Cor, Inc., Lincoln, NE) is another indirect optical method to assess forest structure. It is typically used to quantify the plant area index (PAI) and works on the principle of calculating transmittance based on the ratio of measurements below and outside the canopy (Jonckheere et al., 2004; Gond et al., 1999). PAI is defined as the one-sided area of plant material surface per unit of ground surface area. However, the coarse resolution of the LAI-2000 restricts detailed spatial analysis of the distribution of canopy constituents and PAI, and tends to underestimate PAI in heterogeneous canopies (Jonckheere et al., 2004).

Vertical profiles of gap fraction and plant area are important structural metrics when quantifying the canopy structure and can be used to derive various metrics, such as PAI, tree height, height of maximum density or the canopy base height (Jupp et al., 2009). Ni-Meister et al. (2010) and Jupp et al. (2009) used TLS data to derive vertical plant profiles,

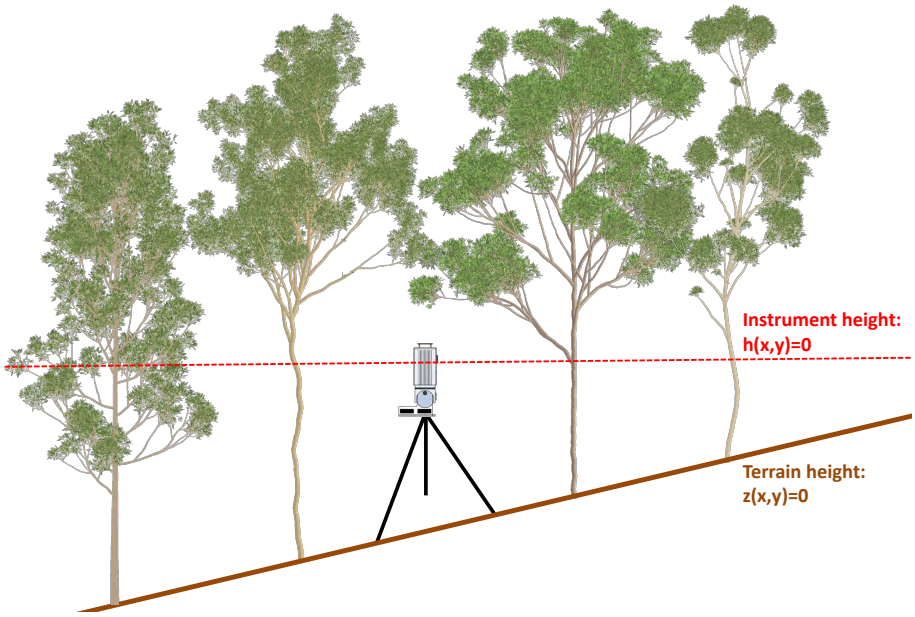


**Figure 1.2:** Illustration of terrestrial LiDAR height recordings on sloped terrain. Heights are recorded with respect to the origin of the instrument (red line) and not to the true topography (brown line).

which describe the plant area as a function of canopy height. The vertical distribution of plant area volume density (PAVD) was calculated through estimates of the vertically resolved gap fraction.

Topography, path length, clumping, leaf angle distribution, spatial sampling and sensor characteristics contribute to the uncertainty in gap fraction derived vertical plant profiles. Mild to moderate wind can potentially introduce some noise in the TLS data, and therefore influence derived gap fractions, due to the movement of branches, twigs and foliage (Côté et al., 2009). There is interaction between these error contributions and they are not independent. Previous work of España et al. (2008) has looked into issues of path length and Jupp et al. (2009) developed a method that attempted to minimise the sensitivity to clumping from single TLS scans. Most TLS studies that inferred canopy structural parameters from TLS used data collected over flat terrain (Ni-Meister et al., 2010) or did not state any topography correction (Zhao et al., 2012, 2011; Yao et al., 2011), although the importance of topographic effects on parameter retrieval was raised in these studies. Not correcting for topography will lead to propagation of error in canopy structure retrieval because heights are recorded relatively to the position and origin of the instrument and not to the true topography (figure 1.2).

## 1.3 Estimating above-ground biomass using TLS

Above-ground biomass (AGB) is a good proxy for forest productivity, carbon storage and sequestration of forests (Bi et al., 2004). Estimating changes in AGB and related carbon emissions is critical for Measurement, Reporting and Verification (MRV) systems in the context of REDD+. REDD+ is a climate change mitigation programme that is developed and supported by initiatives such as The United Nations Collaborative Programme on Reducing Emissions from Deforestation and Forest Degradation (UN-REDD) (United Nations, 2014; Herold et al., 2011).

Accurate ground data are needed for the calibration and validation of global satellite derived AGB datasets. Both Baccini et al. (2012) and Saatchi et al. (2011) published pantropical AGB maps using similar input data. Mitchard et al. (2013) found substantial differences in mapped AGB between these two maps and different spatial patterns when compared to field data distributed across the region (Mitchard et al., 2014). More emphasis on real plot level measurement of AGB is needed to improve the calibration and validation of these maps (Asner et al., 2013). Traditional field methods generally estimate AGB based on indirect relationships with tree parameters, such as diameter at breast height (DBH) and tree height (Chave et al., 2014; Bi et al., 2004). Chave et al. (2004) identified four types of uncertainty in AGB assessment using traditional forest inventory data: (i) errors in tree inventory, (ii) errors in the allometric equation, (iii) errors related to the size of the sampling plots, and (iv) errors related to the landscape-scale

representation of these sampling plots. Detailed 3D TLS data has the potential to reduce errors (i) and (ii) by improving the traditional field methods to estimate AGB. It can also provide insight into errors (iii) and (iv), which are related to the spatial variance of the forest and its structure.

The 3D point clouds generated from terrestrial LiDAR have the potential to give direct estimates of tree volume. These volume estimates can be converted to AGB and may support the reduction of uncertainties in estimating AGB. This is a promising development, however there are still some issues to overcome before a fully automated algorithm will be able to convert the LiDAR point cloud to a tree model. For example, the scanner is not able to identify which points to connect or which points belong to which part of the tree (Hancock, 2010). Côté et al. (2009) developed a robust method to reconstruct the 3D tree architecture from terrestrial LiDAR scans. This architectural model, called *L-Architect*, did not take into account the wind and occlusion induced artefacts, which are considered to be important error sources in terrestrial laser scanning, although multiple scan positions were used to decrease the level of signal obstruction by various vegetation components. *L-Architect* was designed to synthesise and quantify the spatial distribution of tree constituents from TLS point clouds (Côté et al., 2011, 2012). Raumonen et al. (2013) presented a tree reconstruction method using quantitative structure models (QSMs). The output of the reconstruction method is a cylinder model of the tree structure, which allows for straightforward tree volume calculations. The reconstruction method has two main steps: i) segmentation; and ii) surface reconstruction. Their method reconstructs the tree structure via an advancing collection of cover sets (i.e. small local point clouds) and does not require prior assumptions about tree architecture. The main limitation of both tree reconstruction models discussed above is the lack of true reference data for tree volume that is needed for the validation of such models. 3D computer generated tree models can be used for testing modelling approaches (Disney et al., 2012), because reference data can be calculated from the models. Validation on real plot data involves destructive sampling, which is expensive and impractical and, as such, can only be conducted on a limited basis.

## 1.4 Upscaling of TLS data

TLS is not a regional sampling tool but provides very detailed local 3D data, whereas airborne and spaceborne LiDAR sensors provide less-detailed 3D information that can be used at large scale.

Little work has been conducted on quantitative LiDAR signal interpretation and relating LiDAR data to the fundamental principles of the reflected signal. Crown archetypes are often used for estimating vegetation structure from air/spaceborne LiDAR signals (Ferraz et al., 2012; North et al., 2010; Ni-Meister et al., 2001; Sun & Ranson, 2000). These crown

archetypes are typically assumed to contain a turbid medium to account for within-crown scattering. However, such assumptions may make it difficult to relate derived structural parameters to measurable properties of the canopy. Analytical solutions to the scalar radiative transfer equation for a LiDAR signal for specific crown archetypes can be derived from a limited number of assumptions. Crown archetype assumptions can then be tested by inverting these analytical expressions in combination with 3D models of which all parameters are known. If these assumptions are valid, analytical expressions for LiDAR scattering would be preferred over empirical relationships, as analytical expressions will allow retrieval of crown parameters that are physically interpretable. If such crown archetype assumptions are proven to be flawed, the analytical solutions will give insight into why this is, and how terrestrial LiDAR data can potentially improve modelling of virtual forest stands. TLS provides very accurate and detailed measurement of the 3D forest structure at plot level scale, and therefore has the potential to be used as a tool for improving tree modelling by generating explicitly modelled forest plots which are not dependent on the assumptions made for crown archetypes. In this way, TLS data can then assist in the validation and calibration of airborne and spaceborne sensors through radiative transfer modelling.

This thesis focusses on simulating large footprint air/spaceborne LiDAR over virtual scene models, but this work can easily be transferred to simulating optical satellite data. This may, for example, give us more insight into and understanding of how forest structure affects the anisotropic scatting of vegetation in optical satellite data.

## 1.5 Objectives

The main objective of this thesis is to explore the potential of using 3D terrestrial LiDAR to monitor forests at plot level scale and to develop methods to derive accurate reference data. TLS inferred information can potentially contribute to more objective calibration and validation of remotely sensed measures from satellites by providing a better quantification of the 3D forest structure. To achieve this, this thesis investigates the following research questions:

1. How can we derive topography-corrected vertical plant profiles from terrestrial LiDAR?
2. How can we use TLS derived vertical plant profiles to monitor spring phenology?
3. How can we use TLS point clouds to estimate above-ground biomass?
4. How well do crown archetypes represent true crown architecture when inferring broad-scale forest structure?

## 1.6 Thesis structure

This thesis consists of six chapters, including this introductory chapter. Chapter 2 to 5 address the research questions presented in section 1.5.

Chapter 2 presents an automated approach that facilitates rapid and robust assessment of the vertical structure of vegetation from TLS data. Single scans and local plane fitting are used to correct for topographic effects in vertical plant profiles. The approach is tested in five different Australian forest types with different topography and understorey. (Research question 1)

Chapter 3 applies the method from chapter 2 to monitor phenological changes in a temperate broadleaf forest in the Netherlands. TLS measurements track seasonal dynamics with high temporal TLS measurements, starting at leaf-off conditions in winter to a fully developed canopy in summer. This chapter gives insight into the stability and repeatability of these TLS measurements. The start of the growing season (SOS) is inferred from structural changes derived from TLS time series data and is compared with SOS estimates from meteorological data driven models. (Research question 2)

Chapter 4 presents an approach to estimate above-ground biomass from TLS data. The approach does not require any prior information about allometry and derives AGB estimates from direct TLS volume estimates and basic density information. The TLS derived AGB estimates are compared against allometric biomass models and against destructively sampled estimates from two sites in Australia. (Research question 3)

Chapter 5 investigates assumptions of crown archetypes for modelling large-footprint airborne and spaceborne LiDAR. A new set of analytical expressions for modelling LiDAR signals is developed to test the impact of crown archetypes. The expressions are eventually tested against more realistic 3D representations of broadleaved deciduous (birch) and evergreen needle-leaved (Sitka spruce) tree crowns. This chapter gives some insight into using archetype and explicit tree models. This is of importance because terrestrial LiDAR provides detailed 3D information and has the potential to create explicit virtual forest stands that can assist in the calibration and validation of airborne and spaceborne sensors. (Research question 4)

Chapter 6 presents the main conclusions of this thesis and discusses the results in relation to the research questions, along with recommendations for further research.

# Chapter 2

# Vertical plant profiles

This chapter is based on:

Calders, K., Armston, J., Newnham, G., Herold, M. and Goodwin, N., 2014. Implications of sensor configuration and topography on vertical plant profiles derived from terrestrial LiDAR. *Agricultural and Forest Meteorology*, 194, 104-117.

***Abstract:*** The vertical distribution of plant constituents is a key parameter to describe vegetation structure and influences several processes, such as radiation interception, growth and habitat. Terrestrial laser scanning (TLS), also referred to as terrestrial LiDAR, has the potential to measure the canopy structure with high spatial detail and accuracy. Vertical plant profiles, which describe the plant area per unit volume (PAVD) as a function of height, are often used to quantify the vertical structure. However, most studies do not account for topography, use registered multiple TLS scans or use a detailed airborne LiDAR digital terrain model to account for this variation in ground height. Airborne LiDAR is often not available or expensive to acquire. Here, we present an approach that facilitates rapid, robust and automated assessment of the vertical structure of vegetation. We use single scans and local plane fitting to correct for topographic effects in vertical plant profiles and test our approach in five different Australian forest types with different topography and understorey. We validate our approach with topography-corrected vertical plant profiles with digital terrain models derived from airborne LiDAR. Our results demonstrate that not correcting for topography can lead to significant errors in the vertical distribution of plant constituents (CV(RMSE) up to 66.2%, typically ranging from 4.2% to 13.8%). This error decreases significantly when topography is accounted for with TLS plane fitting (CV(RMSE) up to 20.6%, typically ranging from 1.5% to 12.6%). We demonstrate that height metrics from vertical plant profiles that are not corrected for topography depart significantly from those that are inferred from the reference profile. The effect is most noticeable for canopy top height and the peak PAVD height. Correcting topography with a TLS plane fitting approach reduces the error in canopy top height by at least 77% and up to 100%, and reduces the error in peak PAVD height by 83.3% and up to 100%. We also show the advantage of a multiple return over a first return TLS instrument. The definition of the ground returns with a first return instrument might be problematic in environments with dense herbaceous understorey and there is an overall trend of lower height metrics compared to multiple return instruments. We present a data-driven approach that is based on single scan TLS data. The latter is of importance for large area sampling as it allows more sites to be sampled from existing resources and facilitate consistent processing of archived TLS data, which is often single scan data with no survey control.

## 2.1 Introduction

Data retrieved through remote and near sensing methods can be a useful tool to monitor forest ecosystems, with a currently increasing interest on human-induced forest disturbances and forest carbon stock changes (Herold & Skutsch, 2011; De Sy et al., 2012). There is a significant increase in the availability of different global satellite derived biophysical data sets for the monitoring of forest dynamics. The use of such data is currently not supported by rapid assessment of accurate and detailed in-situ biophysical measurements that can be repeated objectively or give efficient structural detail on the vertical dimension.

Vertical profiles of gap fraction and plant area are key structural metrics that explicitly describe the canopy structure and can be used to derive various metrics, such as tree height, height of maximum density or the canopy base height (Jupp et al., 2009). Gap fraction is defined as the probability of a beam with infinitesimal width being able to transmit through the canopy. Vertical profiles of plant area can be calculated through estimates of the vertically resolved gap fraction and describe the vertical distribution of plant area volume density (PAVD) as a function of height. The vertical distribution of canopy constituents has a big impact on the microclimate and influences processes such as radiation interception, growth and available habitat. Parker et al. (1989) used the vertical distribution of canopy leaves derived from ground-based optical measurements to describe the leaf stratification in a mixed deciduous forest. Wang & Li (2013) introduced a new canopy scale radiative transfer model that takes into account vertical heterogeneity within the canopy. Their model simulations indicated that accounting for the multiple-layer structure of the canopy is a prerequisite for correct reflectance simulations at canopy scale and not having information about the vertical heterogeneity may lead to biases in inferred directional reflectance. Previous studies also showed the relation of the vertical structure of vegetation with habitat heterogeneity. Tanaka et al. (2010) suggested that the spatial partitioning by ant assemblages on canopy trees is affected by differences in microenvironmental heterogeneity generated by the structure of constituents in the crowns. Holmes & Sherry (2001) found that an important factor affecting bird population was a temporal change in the vertical distribution of foliage. Different measures derived from large-footprint LiDAR (light detection and ranging) were related to bird species richness in Goetz et al. (2007). They found that the canopy vertical distribution was the strongest predictor of species richness.

The work of Stark et al. (2012) illustrated that vertical profiles of canopy leaf area are a good tool to monitor forest structural variation and carbon dynamics in the Amazon. Previously, metrics which could be derived from vertically projected PAVD profiles (hereafter referred to as vertical plant profiles) were used to estimate above ground biomass (AGB). Total tree height from traditional forest inventory was one of the parameters in the regression equations used by Brown et al. (1989) and Chave et al. (2005) to estimate AGB

of individual trees for tropical forests. Large-footprint LiDAR height measures, such as maximum forest height and height of the median energy (HOME) have been significantly related to AGB at both footprint and plot levels (Lefsky et al., 2005; Drake et al., 2002). The allometric relations in these studies are empirical and site-specific and large uncertainties are still present when applied over large areas. Ni-Meister et al. (2010) suggested a more physically based approach using data from field inventory, airborne LVIS (laser vegetation imaging sensor, footprint ∼20 m) and terrestrial LiDAR. The hemispherical scanning, full waveform digitized terrestrial LiDAR EVI (Echidna® validation instrument, Strahler et al. (2008)) was used to collect detailed canopy structure measurement from ground. Their analysis of LVIS metrics confirmed findings in Drake et al. (2002) and suggested that the HOME metric performed best because of the direct relationship with canopy height and gap fraction. Previous examples indicate that quantifying the vertical distribution of plant material is key. Even a small offset in height or the vertical distribution of canopy constituents might lead to significant errors in its application. The analysis of the ground-based EVI data in Ni-Meister et al. (2010) demonstrated that wood volume is an excellent biomass predictor. Basal area and tree height information were derived from the terrestrial LiDAR data and biomass could be estimated without having to use established allometric equations. Terrestrial laser scanning (TLS), also referred to as terrestrial LiDAR, offers the possibility to collect highly detailed measurements of the vertical distribution of plant constituents in the canopy. Height can then be easily derived from these vertical plant profiles. Jupp et al. (2009) and Ni-Meister et al. (2010) used Echidna® to derive gap probabilities. The results in their study demonstrated the consistency and reproducibility of LiDAR data to estimate vertical plant profiles.

Uncertainty in gap fraction derived plant area profiles is a function of terrain, path length, clumping, leaf angle distribution (LAD), spatial sampling and sensor characteristics. All these error contributions interact and they are not independent. Previous work of España et al. (2008) has suggested that path length only marginally influenced the estimation of effective LAI for low to medium slopes ($< 25°$). Jupp et al. (2009) developed a method that attempted to minimise the sensitivity to clumping by deriving solid angle weighted vertical plant profiles from single TLS scans. Ni-Meister et al. (2010) used TLS data collected over flat terrain and the topography of the study site was not detailed in Jupp et al. (2009), but the assumption of flat terrain was implied. Lovell et al. (2011b) used Echidna® data from a fixed viewpoint to identify the location and measure the diameter of tree stems within a forest without taking topographic effects into account. Many other studies that inferred canopy structural parameters from TLS did not mention any topography correction before analysis (Zhao et al., 2012, 2011; Yao et al., 2011), although the importance of topographic effects on parameter retrieval was raised in these studies. Not correcting for topography will lead to propagation of error in canopy structure retrieval because heights are recorded relatively to the instrument's position and origin and not to the true topography.

To correct for topography, a very high spatial resolution DTM can be used, but this is

often not available at an adequate spatial resolution. Ideally, an accurate digital terrain model (DTM) would be derived from the TLS data itself. However, ground returns from TLS data are often occluded by ground cover, vegetation, woody debris and topography itself (Newnham et al., 2012a). Zhang et al. (2003a) developed a progressive morphological filter to detect non-ground returns from airborne LiDAR so a DTM could be generated. This approach was adapted for use with TLS data by Newnham et al. (2012a) and Pirotti et al. (2013). The problem with morphological filtering is that it can only be applied in areas where data is collected. One solution to overcome the occluded areas in TLS data would be to work with multiple registered scan positions to generate a DTM (Hilker et al., 2012). Such an approach would result in a very detailed local DTM, but the data acquisition time in such a setup would significantly increase compared to a single scan because registration targets would have to be set-up. Zhao et al. (2013) confirmed the obvious effect of local topography on foliage profile retrieval. They used plane fitting through the ground points of multiple merged EVI scans to characterize local topography in foliage profiles retrieved from EVI point cloud data. Slope correction by means of fitting a plane to the prevailing slope and aspect was also suggested by Yao et al. (2011). The advantage of such an approach is that the DTM has no holes or gaps in spatial coverage and can easily be extrapolated to areas where no ground returns were collected. Using multiple scans also requires a voxel approach to generate vertical plant profiles, which can be sensitive to misregistration and wind effects. Jupp et al. (2009) presented a method to derive vertical plant profiles from single scans. This is of interest because using single scans only will increase the number of sampling plots that can be collected in a given time, which is potentially more important than highly accurate 3D reconstruction of the terrain. Other TLS applications, for example tree reconstruction (Calders et al., 2013b; Burt et al., 2013), require a full 3D representation of the forest plot. Occlusion can be problematic for these applications and will require a multiple registered scan approach (Yang et al., 2013; Van der Zande et al., 2009).

In this paper we suggest a technique that could be used for rapid assessment of the vertical structure. We will use single scans and local plane fitting to correct for topographic effects, with minimising sensitivity to understorey. We will validate the approach, which has important implications for large area sampling of AGB as it enables more sites to be sampled from existing resources. It will also facilitate consistent processing of archived data, which is often single scan data with no survey control. Our work is therefore focussed on a number of different environments and will also test different scanner configurations. The main objectives of this paper are:

1. The derivation of topography-corrected vertical plant profiles from a single TLS scan;
2. The validation of such topography-corrected vertical plant profiles with DTMs derived from airborne LiDAR; and
3. The demonstration of the robustness of this approach for rapid assessment of vertical

structure over different forest types and topographic conditions.

Although it may be considered sub-optimal to use single scans, we prefer not to merge multiple scans. Our approach supports the need for a rapid, robust and automated approach. As part of the first objective, we will also compare topographically corrected multiple return TLS data with first return TLS data for the assessment of vegetation structure. Lovell et al. (2011a) has shown that plant area profile methods developed for waveform data (Jupp et al., 2009) are applicable to discrete return data, but implications of single versus multiple return and pulse density are unclear. Recent work on sensor intercomparison (Newnham et al., 2012a,b) have multiple sensor and survey characteristics varying simultaneously. Here, we will compare first versus multiple return TLS data while keeping all the other sensor characteristics constant.

## 2.2 Study Area and Data Collection

### 2.2.1 Study area

Terrestrial LiDAR data were acquired in five different Australian forest types during the period March - December 2012. The sampling plots were located in Queensland and Victoria and the forest types are: (i) Banksia aemula low open woodland, (ii) mixed species notophyll vine forest, (iii) open forest (Eucalyptus spp.), (iv) Dry sclerophyll box-ironbark forest and (v) tall Eucalypt forest (Eucalyptus regnans) (Figure 2.1). The plots were selected so that they covered a range of forest types, understorey and topography. Characteristics of the different forest types can be found in table 2.1.

**Figure 2.1:** Overview of the different study sites. These photographs were taken on the day of TLS data acquisition. From left to right: Banksia aemula low open woodland [SUNS0104], Mixed species notophyll vine forest [SUNS0103], Open forest (Eucalyptus spp.) [GOLD0101], Dry sclerophyll box-ironbark forest [RUSH08] and Tall Eucalypt forest (Eucalyptus regnans) [WATT01].

**Table 2.1:** Characteristics of the different study areas located in Queensland and Victoria, Australia: forest type, slope & understorey characteristics, acquisition time and number of scan locations. The slope is the average slope of the individual scan locations derived from fitting a plane through the ground returns around each scan location (5 m extent, 1m resolution).

| Study area | Plot name | Forest type | Average slope [°] (sdev)[1] | Woody understorey | Herbaceous understorey | Acquisition time | # of scans |
|---|---|---|---|---|---|---|---|
| Cooloola National Park QLD | SUNS0104 | *Banksia aemula* low open woodland | 1.26 (0.18) | medium | dense | May 2012 | 5 |
| Cooloola National Park QLD | SUNS0103 | Mixed species notophyll vine forest | 3.39 (0.49) | medium | medium | April 2012 | 5 |
| D'Aguilar National Park QLD | GOLD0101 | Open forest (Eucalyptus spp.) | 7.65 (0.29) | little | dense | December 2012 | 4 |
| Rushworth Forest VIC | RUSH08 | Dry sclerophyll box-ironbark forest | 1.58 (0.83) | little | little | May 2012 | 5 |
| Watts Creek VIC | WATT01 | Tall Eucalypt forest (*Eucalyptus regnans*) | 6.30 (NA) | medium | dense | March 2012 | 1 |

[1] sdev = standard deviation; NA = not applicable

### 2.2.2 LiDAR data

Terrestrial LiDAR data were acquired with the RIEGL VZ-400 3D terrestrial scanner (RIEGL Laser Measurement Systems GmbH, Horn, Austria). This time-of-flight scanner provides fast data acquisition and has a range up to 350 m. The line scanning mechanism uses a fast rotating multi-facet polygonal mirror. This system leads to fully linear, unidirectional and parallel scan lines. The beam divergence is nominally 0.35 mrad and the scanner operates in the near infrared (wavelength 1550 nm). The instrument also collects information about the pitch and roll (through inclination sensors) and yaw (through an internal compass) (RIEGL, 2013). The scanner settings were the same across all plots and are summarised in table 2.2. The number of single scans per study site varied (see table 2.1) and figure 2.2 shows the different plot setups.

The RIEGL VZ-400 scanner records multiple return data (up to four returns per emitted pulse), with returns being derived from onboard waveform processing. The advantage of having multiple returns has been discussed by Lovell et al. (2003). They made note of the weaker response at greater canopy height with single return instruments, concluding that

**Table 2.2:** Riegl VZ-400 scanner settings for data acquisition.

| | |
|---|---|
| Beam divergence | 0.35 mrad |
| Pulse repetition rate | 300 kHz |
| Minimum range | 0.5 m (SUNS plots) - 1.5 m (other plots) |
| Azimuth range | 0° - 360° (0.06° angular sampling) |
| Zenith range | 30° - 130° (0.06° angular sampling) |
| Acquisition time | 1 minute 23 seconds |

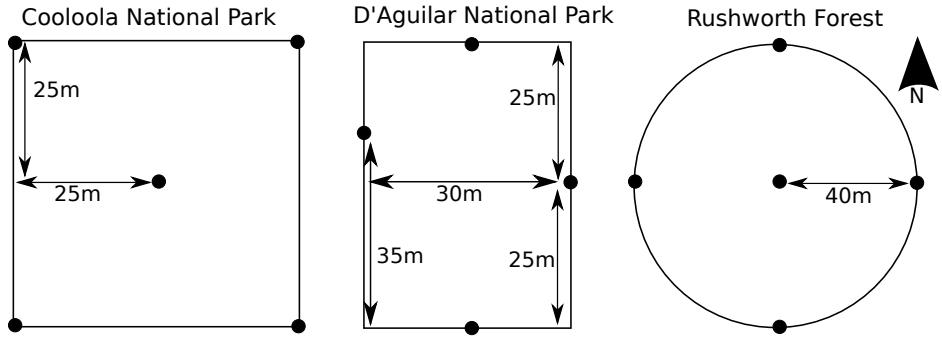


**Figure 2.2:** TLS plot setups for Cooloola National Park, D'Aguilar National Park and Rushworth Forest. Scan locations are indicated with a black dot. Only one scan position was used in Watts Creek.

multiple returns will lead to an improved vertical sampling. Throughout this work we will compare multiple return TLS data with first return TLS data for the assessment of vegetation structure, since most commercial discrete return TLS are first return instruments. The first return TLS data is a subset from the original multiple return RIEGL data, with only first returns included. Table 2.3 summarises the return distribution for each study area. The contribution of second to fourth return to the total number of returns ranges from 19.9% to 33.3%.

Airborne LiDAR (ALS) data were used as reference data for tree heights and to generate DTMs for the validation of topography-corrected vertical plant profiles from single scan TLS data. The ALS specifications for the different study areas are summarised in table 2.4.

The vertical accuracy of the ALS capture in D'Aguilar National Park was tested using a distribution of ten control points throughout this plot, the exact position and height of which were measured in the field. ALS heights were then derived and showed an RMSE of 0.125 m, with a residual mean of -0.0392 m and standard deviation of 0.1251 m (according to the ASPRS guidelines on reporting vertical accuracy for LiDAR data (Flood, 2004)).

**Table 2.3:** Distribution of the TLS LiDAR returns for each study area. The central scan location was used for all study areas, except for GOLD0101 (South location).

| | **Study area** | | | | |
|---|---|---|---|---|---|
| **LiDAR return** | **SUNS0104** | **SUNS0103** | **GOLD0101** | **RUSH08** | **WATT01** |
| First | 5,283,459 (80.1%) | 6,661,801 (66.7%) | 6,584,292 (70.0%) | 7,221,824 (79.4%) | 7,192,851 (76.1%) |
| Second | 1,121,355 (17.0%) | 2,457,575 (24.6%) | 2,085,190 (22.2%) | 1,430,086 (15.7%) | 1,865,470 (19.7%) |
| Third | 164,843 (2.5%) | 663,445 (6.6%) | 582 965 (6.2%) | 364,739 (4.0%) | 345,709 (3.7%) |
| Fourth | 27,147 (0.4%) | 202,411 (2.0%) | 157 897 (1.7%) | 76,346 (0.8%) | 51,287 (0.5%) |
| Total | 6,596,804 | 9,985,232 | 9,410,344 | 9,092,995 | 9,455,317 |

**Table 2.4:** Specifications of the ALS data acquisition for the different study areas.

| Study area | Sensor | Nominal altitude [m] | Acquisition time | Pulse density [pulses/m$^2$] | Swath overlap [%] | max. # returns/pulse | Reference |
|---|---|---|---|---|---|---|---|
| Cooloola National Park | RIEGL Q680i | 500 | April 2012 | 10 | 100 | 6 | ROAMES (2012) |
| D'Aguilar National Park | Leica ALS50-II | 1700 | December 2010 | 2 | 25 | 4 | DSITIA (2012) |
| Rushworth Forest | RIEGL Q560 | 300 | April 2012 | 20 | 50 | 6 | Airborne Research Australia (2012) |
| Watts Creek | RIEGL Q560 | 300 | April 2012 | 20 | 50 | 6 | Airborne Research Australia (2012) |

Despite our limited number of observations, our findings are in line with the metadata for this ALS capture that reports an RMSE of 0.15 m in open areas. Earlier work on vertical accuracy assessment for LiDAR data under eucalypt stands reported an RMSE of 0.15 m (Gomes Pereira & Gonçalves, 2010).

The Multi Station Adjustment (MSA) algorithm in the RiSCAN PRO software (provided by RIEGL) was used to spatially align the airborne and terrestrial scan data. The MSA algorithm modifies the orientation and position of each dataset in several iterations to calculate the best overall fit. The raw TLS data were converted to the sorted pulse data (SPD) format with the open source sorted pulse data software library (Bunting et al., 2013b,a) for further analysis.

## 2.3 Methods

### 2.3.1 Vertical plant profiles

The vertical vegetation structure at each study site was described by the plant area volume density (PAVD). Vertical profiles of plant area per unit volume, referred to as vertical plant profiles, can be calculated from terrestrial LiDAR data through estimates of the vertically resolved gap probability ($P_{gap}$). For consistency with the literature, we will use $L(z)$, the leaf area index (LAI) as a function of height, to formulate the equations. However, it is important to note that this is essentially the plant area index (PAI), which is interpreted as the one-sided area of plant material surface per unit ground surface area.

Newnham et al. (2012a) and Lovell et al. (2011a) approximated the vertically resolved gap probability from a multiple return scanner as:

$$P_{gap}(\theta, z) = 1 - \frac{\sum w_i(z_i{<}z, \theta)}{N(\theta)} \qquad (2.1)$$
$$w = 1/n_s$$

$\theta$ is the zenith angle of the laser pulse, $z$ is the height above the instrument optical centre ($z_0$). The numerator in equation 2.1 gives the number of returns that are below $z$ and the denominator is the total number of outgoing laser pulses for a finite zenith range centered around $\theta$. Here we will use zenith rings of five degrees within the 30 to 70 degree zenith

range. We assume that for a specific outgoing laser pulse each return equates to a beam area interception of $1/n_s$, where $n_s$ is the number of returns for that outgoing laser pulse. For a first return LiDAR instrument, $n_s$ and thus $w$ are 1. Armston et al. (2013a) used equation 2.1 with airborne RIEGL LiDAR data and showed it produced near unbiased estimates of $P_{gap}$.

Jupp et al. (2009) presented a method to derive vertical plant profiles from the vertically resolved gap probability ($P_{gap}$), which was also used by Zhao et al. (2013, 2011) and Lovell et al. (2012).

$$\begin{aligned} P_{gap}(\theta, z) &= e^{-G(\theta)L(z)/cos(\theta)} \\ L(z) &= \int_{z_o}^{z} f(z')dz' \end{aligned} \tag{2.2}$$

The vertical plant profile, $f(z)$, is the horizontally averaged PAVD as a function of height. $G(\theta)$ is the foliage orientation function and equals the projection of a unit area of plant constituents on a plane perpendicular to the direction $\theta$, averaged over elements of all orientations (Ross, 1981). Jupp & Lovell (2007) described a simple parametric model that can be used to model the foliage distribution and separate it in a vertical ($G_v$) and horizontal ($G_h$) component:

$$\begin{aligned} G_h(\theta) &= cos(\theta) \\ G_v(\theta) &= \frac{2}{\pi} sin(\theta) \end{aligned} \tag{2.3}$$

Introducing this concept in equation 2.2 allows a linear estimation of LAI as the sum of $L_h$ and $L_v$:

$$\begin{aligned} k(\theta)L(z) &= L_h(z) + X(\theta)L_v(z) = -log(P_{gap}(\theta, z)) \\ X(\theta) &= \frac{2}{\pi} tan(\theta) \end{aligned} \tag{2.4}$$

Component $k(\theta)$ equals $G(\theta)/cos(\theta)$ and is introduced to combine the leaf and view angle variation. The "hinge angle" is 57.5°, at which $G(\theta)$ is essentially invariant at 0.5 over different leaf angle distributions and LAI can be approximated as:

$$\begin{aligned} L(z) &\approx -1.1log(P_{gap}(57.5°)) \\ f(z) &= \frac{\delta L(z)}{\delta z} \end{aligned} \tag{2.5}$$

The zenith ring between 55° and 60° is often taken to approximate the hinge region (Jupp et al., 2009; Zhao et al., 2011). The vertical plant profile obtained using equation 2.5 shows the vertical structure but will be highly variable because it is using only a small zenith region. To overcome this, Jupp et al. (2009) suggested a solid-angle-weighted normalised

profile. This mean profile is largely independent of clumping and is defined as:

$$\begin{aligned} \frac{L(z)}{LAI} &= \frac{log(P_{gap}(\overline{\theta}, z))}{log(P_{gap}(\overline{\theta}, H))} \\ f(z) &= LAI \frac{\delta}{\delta z} \left( \frac{log(P_{gap}(\overline{\theta}, z))}{log(P_{gap}(\overline{\theta}, H))} \right) \end{aligned} \tag{2.6}$$

Here, $\overline{\theta}$ indicates that the normalised data are averaged over a zenith ring instead of being a mean angle. $H$ is the canopy height at which the LiDAR pulse exits the canopy.

### 2.3.2 Topography correction of vertical plant profiles

Before deriving the vertical plant profiles, the height values in the TLS data are corrected for topography. We suggest (i) an ALS DTM approach and (ii) a TLS plane fitting approach to achieve this. A more detailed outline of the effect of topography on $P_{gap}(\theta, z)$ can be found in appendix 2.A.

#### Topography correction with ALS DTM

First a terrain filter is applied to extract the terrain points from the ALS data. The filter works in a hierarchical manner and analyses the distances of points from an estimated ground surface. The Geospatial Data Abstraction Library (GDAL) library is then used to generate the DTM (GDAL Development Team, 2012). The nearest neighbour algorithm is applied to generate a regular grid with a spatial resolution of 1 m. The generated ALS DTM is then used to correct the height values in the TLS data for topographic effects.

#### Topography correction with TLS plane fitting

The horizontal range for a return is defined as the distance from the scanner multiplied by $\sin(\theta)$. There is some variation in the frequency distribution of horizontal ranges across the different forest types (figure 2.3). The frequency distribution depends on the vegetation structure and for the multiple return TLS data the 90th percentile ranges from 9 m (SUNS0104) to 46 m (GOLD0101 and RUSH08). Only one percent of the data is collected from distances further than 31 m (SUNS0104) to 109 m (RUSH08). For first return TLS data the 90th percentile range decreases and ranges from 6.8 m (SUNS0104) to 33 m (GOLD0101). A similar trend is observed for the 99th percentile, which ranges from 26 m (SUNS0104) to 86 m (RUSH08). The fitted plane can be described as $z = ax+by+c$, where $-c$ is the height of the instrument. The ground returns within a certain extent have to be identified to correct for topography with plane fitting. Only the last returns from

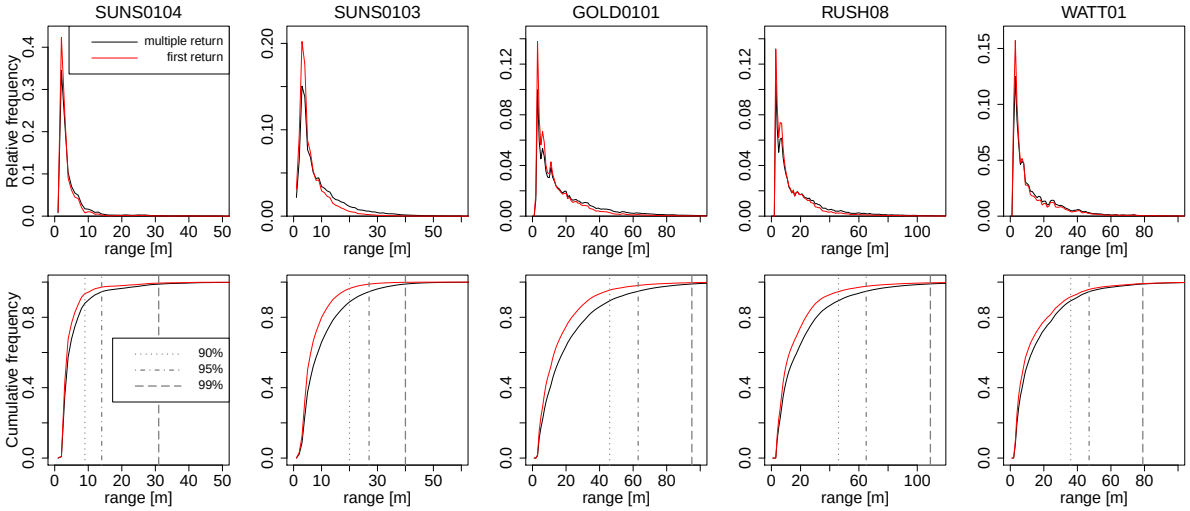


**Figure 2.3:** The frequency distribution of horizontal ranges returned in each forest type. The horizontal range for a return is defined as the distance from the scanner multiplied by $\sin(\theta)$. The 90th, 95th and 99th percentile for multiple return TLS data are indicated in the cumulative frequency plot.

the multiple return TLS data are selected and then the lowest points within a regular grid are classified as ground returns from this subset. Figure 2.4 shows the grid resolution as a function of RMSE. RMSE values are calculated between the reference ALS DTM and the fitted TLS plane. RMSE values in RUSH08 and SUNS0103 show very little sensitivity towards grid resolution. The other three sites have higher RMSE values for smaller grid resolutions, because non-ground returns are being classified as ground returns. Based on this sensitivity analysis, a 50 m by 50 m grid around the scan position with a 5 m resolution is robust for the scanner used in this study, but these remain heuristic values.

These classified ground returns are used in an iterative re-weighted least squares (IRLS) regression. We use the rlm function from the MASS package (Venables & Ripley, 2002) in R (R Development Core Team, 2011) to implement the IRLS regression using Huber's M-estimation. The initial weights are defined as 1/r, where r is the horizontal distance from the scanner. The initial weighting is used due to the gradual positive bias in TLS terrain height relative to the ALS reference DTM with increasing range from the scanner. Newnham et al. (2012a) observed a similar "bowl shape" when comparing TLS and ALS DTMs for a range of commercial TLS instruments. Most of the laser shots are intercepted at close range, which is particularly true for ground returns. Iterative re-weighted least squares regression is better suited for plane fitting of TLS data than ordinary least squares regression as it corrects for erroneous classified ground returns by iteratively re-calculating the residuals and adjusting the weights based on these residuals.

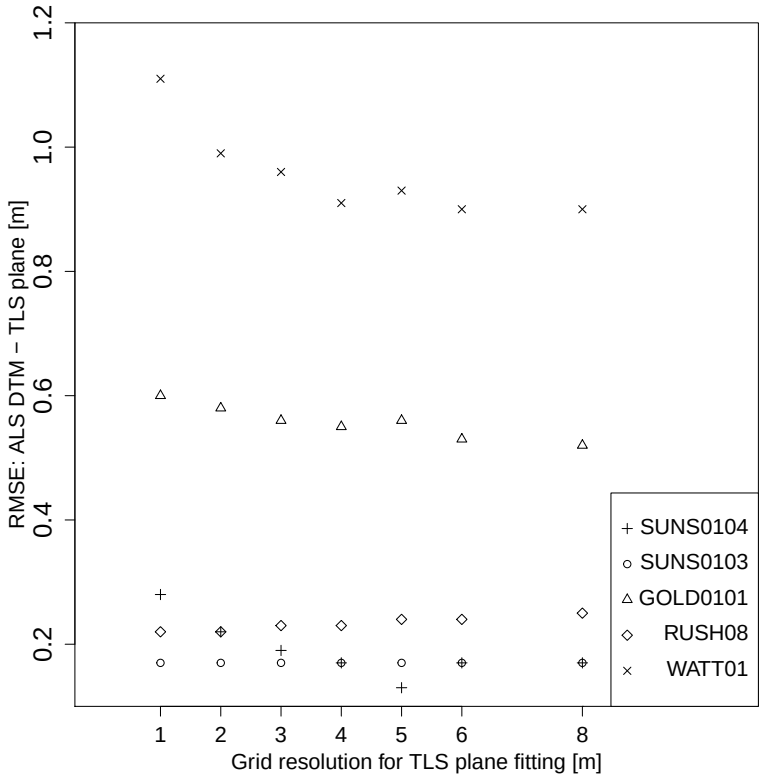


**Figure 2.4:** Sensitivity analysis for different grid resolutions to select ground returns for TLS plane fitting (for extent 50 m by 50 m). RMSE values are calculated between the reference ALS DTM and the fitted TLS plane (grid size is 1 m for both DTMs). This figure shows the results for the South scan location for GOLD0101 and the central scan location for the four other sites.

### Vertical plant profile comparison

The topography in the TLS data is (i) not corrected; (ii) corrected with TLS plane fitting; and (iii) corrected with an ALS DTM. We assume that the ALS DTM provides the best possible reference dataset for topography due to its near nadir scan angles. We therefore use the ALS DTM corrected vertical profile as the reference profile for comparing shape and derived height metrics. When no topography correction is applied, scanner height is still accounted for. The scanner is mounted on a tripod and therefore scanner height was added to all height values in the scan data. The exact scanner height was interpolated from the minimum heights (i.e. ground returns) within a 5 m extent centred around the scan location and at 1 m spatial resolution.

The different vertical plant profiles are evaluated by comparing the coefficient of variation of the root mean squared error, CV(RMSE). The CV(RMSE) is defined as the RMSE normalised to the mean of PAVD and was successfully used in Calders et al. (2013a) to evaluate different LiDAR waveforms. Unlike the RMSE, CV(RMSE) is unitless and this

allows values to be easily compared to one another. Additionally, three different height metrics are derived from each profile to evaluate the topography correction and sensor configuration. These height metrics are: peak PAVD height, 50th percentile and 99.9th percentile. The 50th percentile indicates the height of median PAVD, by analogy with the HOME metric that is commonly used in waveform processing. We define the top canopy height by the 99.9th PAVD percentile to account for, a limited number of, returns from the atmosphere (RIEGL, personal communication).

## 2.4 Results

### 2.4.1 Data registration

Spatial alignment between TLS and ALS was achieved by using the Multi Station Adjustment algorithm on the DTMs derived from both data sets, with a typical standard deviation of 0.05 to 0.07 m. Figure 2.5 shows the extent and registration of both LiDAR datasets for the Banksia aemula low open woodland and Tall Eucalypt forest (Eucalyptus regnans) site. The figure also illustrates the typical "bowl-shape" of the TLS data, with the number of laser shots defining the ground surface decreasing as distance from the scanner increases. This is generally true for most of the laser shots, with the bulk of LiDAR returns being closer to the scanner (horizontal range), as is illustrated in figure 2.3.

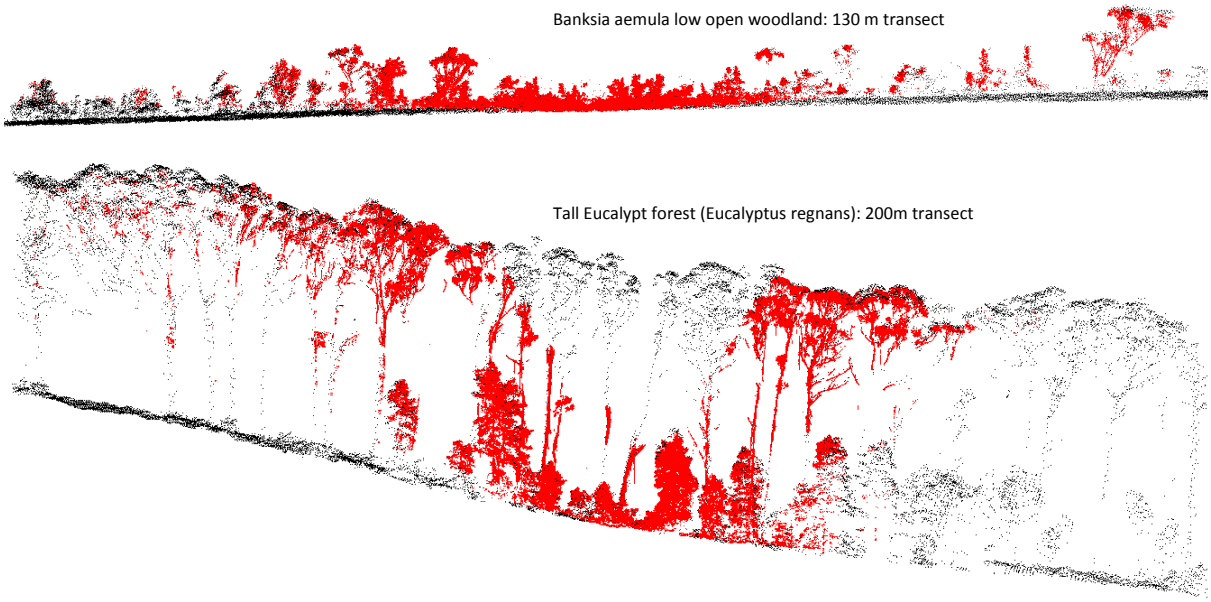


**Figure 2.5:** Cross-section of registered ALS (black) and multiple return TLS (red) data. (top) Banksia aemula low open woodland; (bottom) Tall Eucalypt forest (Eucalyptus regnans)

### 2.4.2 Vertical plant profile comparison

Three different vertical plant profiles are derived for each plot from the TLS data to study the effect of topography and understorey. Figure 2.6 visualises the absolute height offset compared to the ALS reference DTM for (i) no topography correction and (ii) TLS plane correction (for multiple return TLS data). The 90th, 95th and 99th percentile of the horizontal range distributions derived from figure 2.3 are indicated.

The plot average vertical plant profiles are derived by averaging the $P_{gap}(z)$ over all the

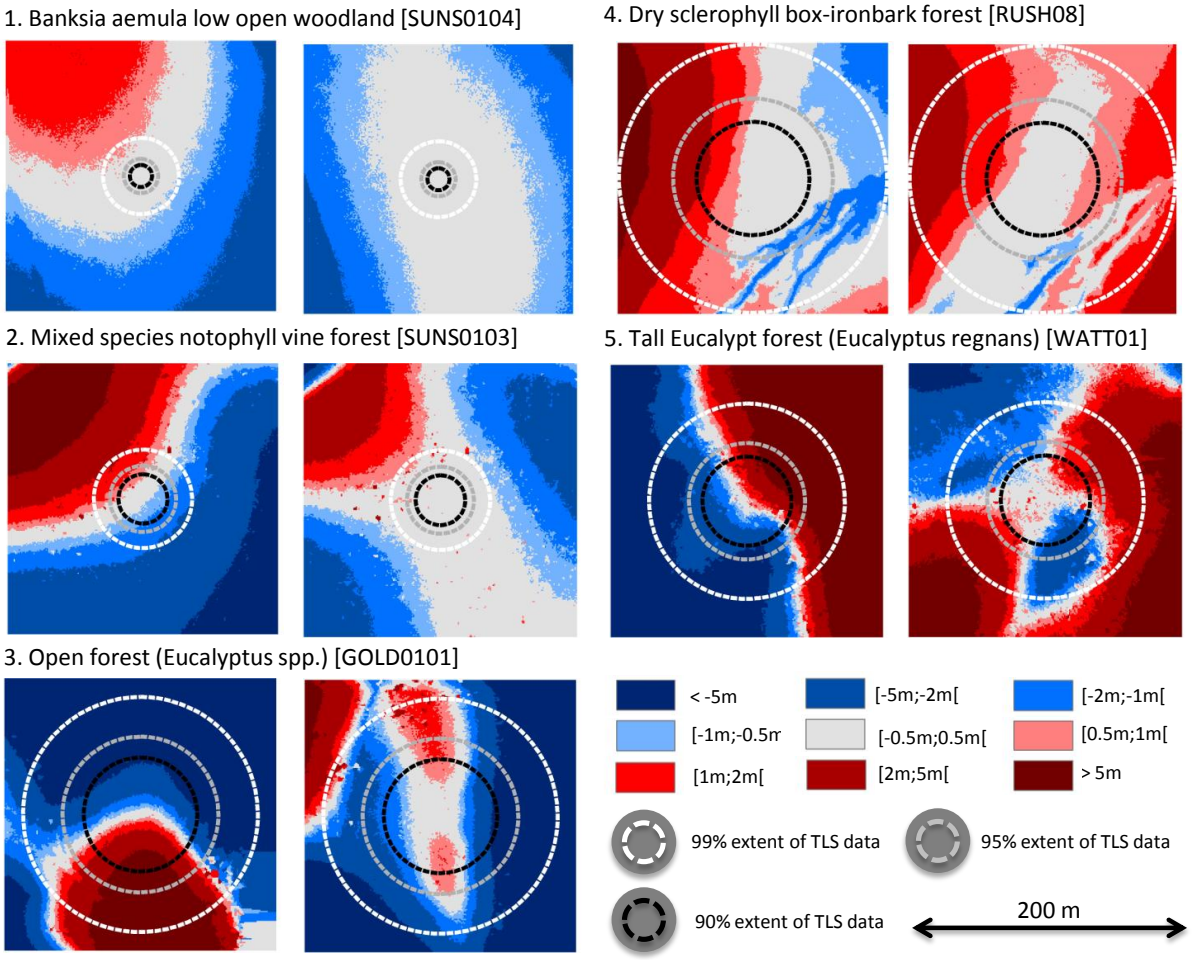


**Figure 2.6:** Difference DTMs visualising the absolute height offset compared to the ALS reference DTM: (left panel) No topography correction: difference DTM = ALS DTM + scanner height; (right panel) Topography corrected with TLS plane fitting: difference DTM = ALS DTM - plane DTM (from multiple return TLS). Grid size is 1 m for both ALS DTM and TLS plane DTM. The extent for each plot is 200 m x 200 m. Dotted lines delineate the 99th (white), 95th (gray) and 90th (black) percentile derived from the horizontal range distribution (see figure 2.3). This figure shows the results for the South scan location for GOLD0101 and the central scan location for the four other sites.

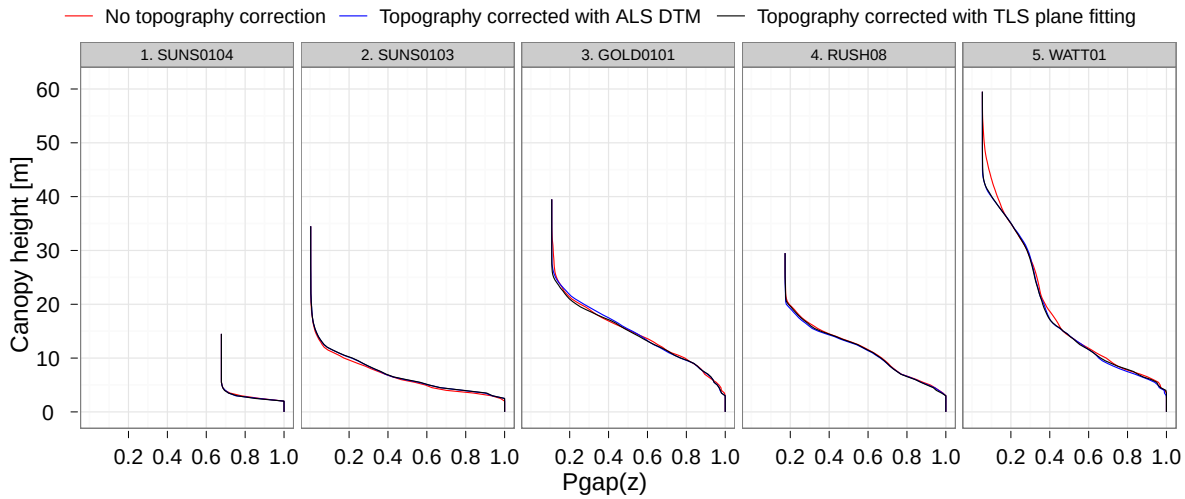


**Figure 2.7:** Plot average directional gap fraction, $P_{gap}(z)$, for hinge region (55°-60° zenith ring) as a function of height. This figure shows the results for the South scan location for GOLD0101 and the central scan location for the four other sites.

scan positions and calculating the vertical plant profile of the averaged $P_{gap}(z)$, which is similar to the approach in Strahler et al. (2008). Figure 2.7 shows $P_{gap}(z)$ for the hinge region zenith ring as a function of canopy height for multiple return TLS data for a single scan location. Apart from the SUNS0103 plot, $P_{gap}(z)$ will not approach zero, indicating that the laser pulse is able to escape the canopy.

Figure 2.8 shows the average vertical plant profiles for each forest type. The SUNS0103 and SUNS0104 plots are characterized by low slope and a significant amount of understorey is present. For the vertical plant profiles for these two sites, derived from multiple return TLS data, there is a positive effect of using a plane fitting topography correction compared to using no correction at all. CV(RMSE) decreases from 11.3% to 6.8% for SUNS0104 and from 6.6% to 1.5% for SUNS0103 (table 2.5). A similar trend is observed for the vertical plant profiles derived from first return TLS data for SUNS0103. However, for vertical plant profiles derived from first return TLS data for SUNS0104, a site with a dense herbaceous understorey, the CV(RMSE) increases from 8.0% to 22.0%.

**Table 2.5:** CV(RMSE) values [%] for comparing the ALS DTM corrected vertical plant profile with (i) the not corrected and (ii) the TLS plane corrected vertical plant profile.

| | | Study area | | | | |
|---|---|---|---|---|---|---|
| **Sensor configuration** | **Compared profiles** | **SUNS0104** | **SUNS0103** | **GOLD0101** | **RUSH08** | **WATT01** |
| Multiple returns | ALS DTM vs. None | 11.3 | 6.6 | 13.8 | 4.2 | 66.2 |
| | ALS DTM vs. TLS plane fitting | 6.8 | 1.5 | 12.6 | 2.3 | 20.6 |
| First return | ALS DTM vs. None | 8.0 | 8.3 | 11.9 | 5.4 | 57.9 |
| | ALS DTM vs. TLS plane fitting | 22.0 | 1.3 | 11.0 | 2.1 | 18.7 |

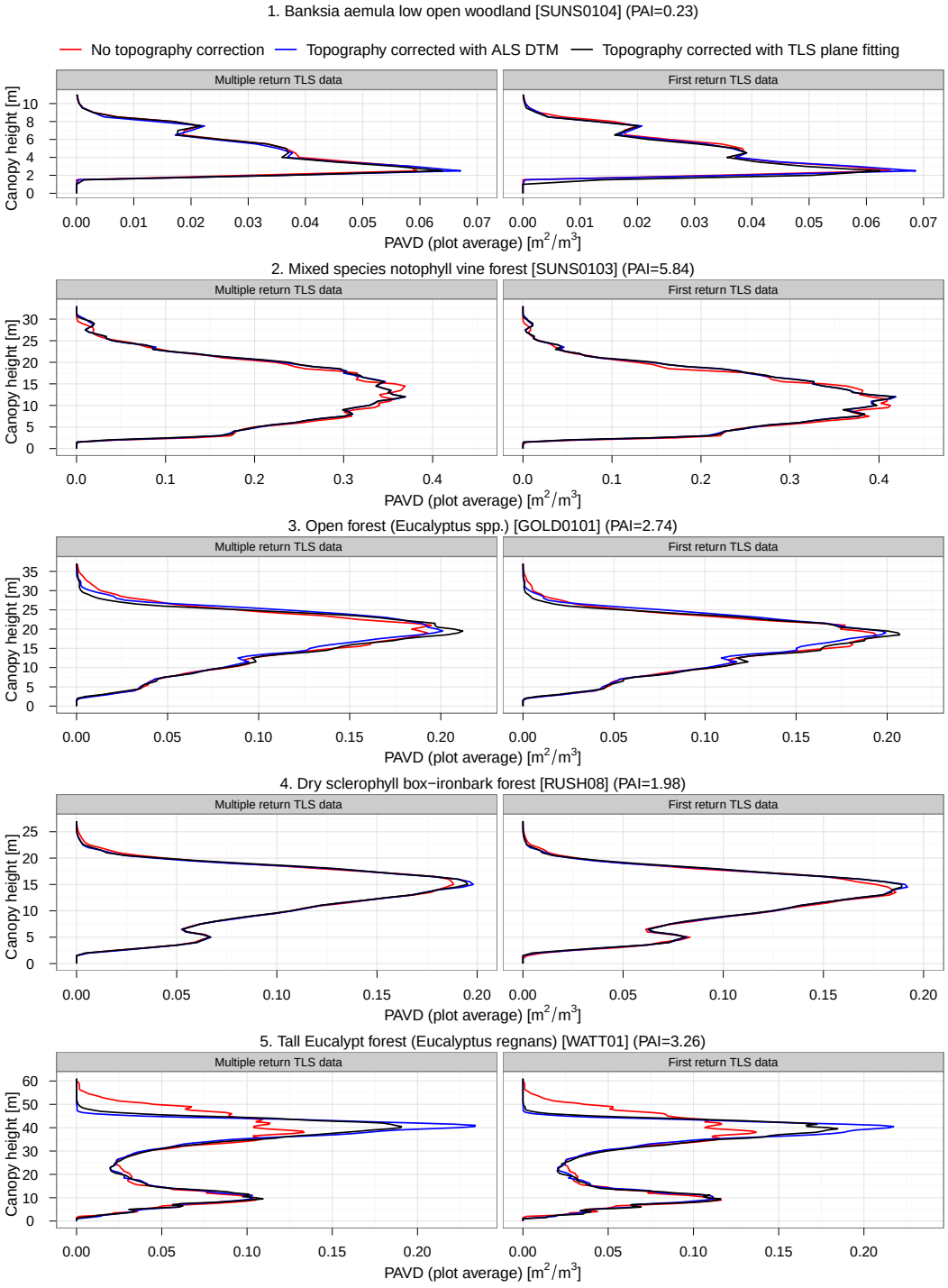


**Figure 2.8:** Plot average vertical plant profiles. For each plot, three plant profiles were derived: (i) no topography correction, (ii) topography corrected with ALS reference DTM, and (iii) topography corrected with TLS plane fitting. (left) vertical plant profiles derived from multiple return TLS data; (right) vertical plant profiles derived from first return TLS data.

Figure 2.9 compares the height percentiles (10th, 20th, 30th, 40th, 50th, 60th, 70th, 80th, 90th, 99.9th) between the different vertical plant profiles and shows a positive effect of the TLS plane fitting compared to applying no correction. This is especially true for the higher height percentiles. The three height metrics derived from the vertical plant profiles are summarised in table 2.6. The peak PAVD height is 2.5 m for SUNS0104 regardless of the topography correction. There is no difference in peak PAVD height (12.0 m) for the SUNS0103 vertical plant profile that is corrected for topography with the ALS DTM or with TLS plane fitting. Not correcting for topography results in an overestimation of this metric with 2.5 m for multiple return TLS data or an underestimation of 2.0 m for first return TLS data. The 50th height percentile agrees within a 0.2 m range for multiple return TLS data and 0.3 m for first return data for both SUNS0103 and SUNS0104. Top canopy height agrees within a 0.1 m range for the multiple return vertical profiles for SUNS0104, but is underestimated by 1.0 m when topography is not corrected for SUNS0103.

The RUSH08 site has little understorey and low slope. Correcting the vertical plant profiles with TLS plane fitting improves the agreement with the ALS DTM corrected reference profiles compared to applying no correction at all: CV(RMSE) decreases from 4.2% to 2.3% for multiple return data and from 5.4% to 2.1% for first return data. Peak PAVD height and the 50th height percentile were the same for the three different profiles derived from multiple return data. Not correcting for topography resulted in a 1.1 m overestimation of canopy top height (multiple return data) for this study site. Peak PAVD was underestimated by 1.0 m (no correction) or overestimated by 0.5 m (TLS plane fitting correction) when derived from first return data vertical plant profiles, but

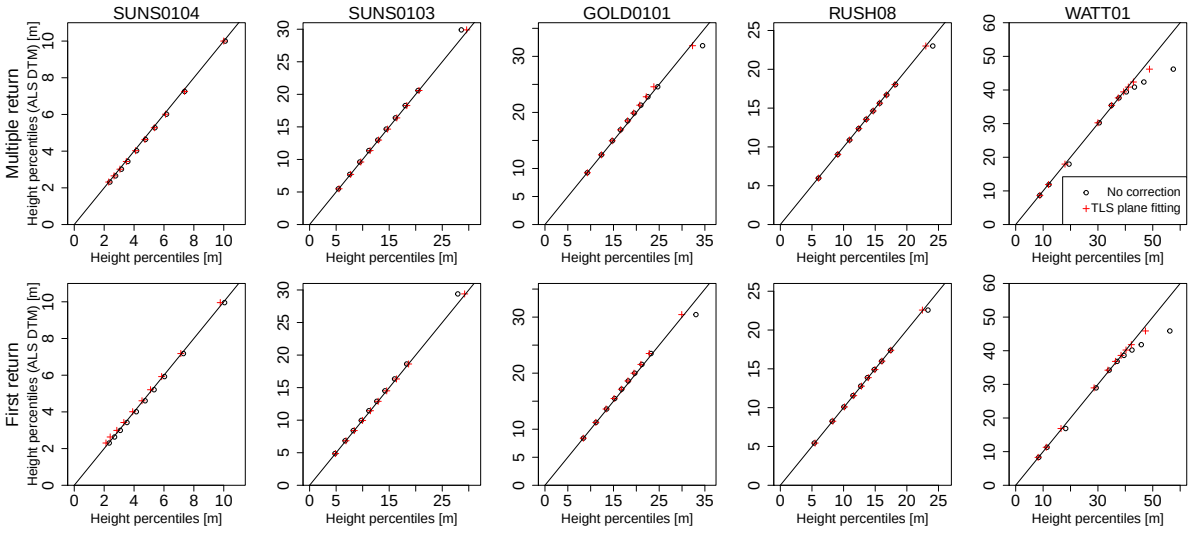


**Figure 2.9:** Comparison of the height percentiles (10th, 20th, 30th, 40th, 50th, 60th, 70th, 80th, 90th, 99.9th) from the ALS DTM corrected vertical plant profiles with (i) the not corrected and (ii) the TLS plane corrected profiles.

**Table 2.6:** Height metrics derived from vertical plant profiles (Peak PAVD height, 50th percentile and top height) and top height derived from ALS.

| Height metric [m] | Sensor configuration | Topography correction | Study area | | | | |
|---|---|---|---|---|---|---|---|
| | | | SUNS0104 | SUNS0103 | GOLD0101 | RUSH08 | WATT01 |
| Peak PAVD height | Multiple returns | None | 2.5 | 14.5 | 21.0 | 15.0 | 38.0 |
| | | TLS plane fitting | 2.5 | 12.0 | 19.5 | 15.0 | 40.5 |
| | | ALS DTM | 2.5 | 12.0 | 19.5 | 15.0 | 41.0 |
| | First return | None | 2.5 | 10.0 | 19.0 | 13.5 | 38.0 |
| | | TLS plane fitting | 2.5 | 12.0 | 19.0 | 15.0 | 39.5 |
| | | ALS DTM | 2.5 | 12.0 | 19.5 | 14.5 | 40.5 |
| 50th percentile | Multiple returns | None | 4.2 | 12.8 | 18.1 | 13.6 | 34.9 |
| | | TLS plane fitting | 4.1 | 13.0 | 18.1 | 13.6 | 35.0 |
| | | ALS DTM | 4.0 | 13.0 | 18.5 | 13.6 | 35.4 |
| | First return | None | 4.2 | 11.2 | 16.8 | 12.7 | 34.1 |
| | | TLS plane fitting | 3.9 | 11.5 | 16.7 | 12.8 | 33.7 |
| | | ALS DTM | 4.0 | 11.5 | 17.1 | 12.8 | 34.2 |
| Top height (99.9th percentile) | Multiple returns | None | 10.1 | 28.6 | 34.5 | 24.1 | 57.5 |
| | | TLS plane fitting | 10.0 | 29.6 | 32.3 | 23.0 | 48.8 |
| | | ALS DTM | 10.0 | 29.9 | 31.9 | 23.0 | 46.2 |
| | First return | None | 10.1 | 27.9 | 33.0 | 23.3 | 56.2 |
| | | TLS plane fitting | 9.8 | 29.2 | 29.9 | 22.5 | 47.3 |
| | | ALS DTM | 10.0 | 29.4 | 30.4 | 22.6 | 45.9 |
| ALS top height | | | 11.6 | 30.4 | 30.8 | 22.5 | 49.6 |

the 50th height percentile was similar for all profiles.

Top canopy height is overestimated if no topography correction is applied on the TLS data of the study sites on significant slope, GOLD0101 and WATT01. This is demonstrated in the profiles in figure 2.8 and the derived height metrics in table 2.6. For GOLD0101, top height is overestimated with 2.6 m when topography is not corrected for and only 0.4 m when TLS plane fitting is applied (multiple return data). The differences are even larger in the WATT01 site: an overestimation of 11.3 m when topography is uncorrected versus only 2.6 m when topography is corrected with TLS plane fitting (multiple return data). Similar trends are observed when the profiles are derived from first return data, however the absolute heights are lower. Peak PAVD height agrees well for both topography corrections (the same for GOLD0101 and 0.5 m difference for WATT01) but is overestimated with 1.5 m in GOLD0101 and underestimated by 3.0 m in WATT01 when topography is not accounted for. The overall shape of the profile improves by applying a TLS plane fitting correction, with CV(RMSE) in GOLD0101 decreasing from 13.8% to 12.6% and from 66.2% to 20.6% in WATT01 compared to the reference profile (multiple return data).

Figure 2.10 shows the difference in height metrics between multiple return and first return vertical plant profiles. The peak PAVD height difference is highest in SUNS0103 and lowest in SUNS0104. The site in SUNS0103 is characterised with the highest PAI (5.84), whereas SUNS0104 has a PAI of only 0.23. The 50th percentile and top canopy heights are consistently lower in the profiles derived from first return data, with an exception for site SUNS0104 where these heights are equal. The differences in 50th percentile height due to

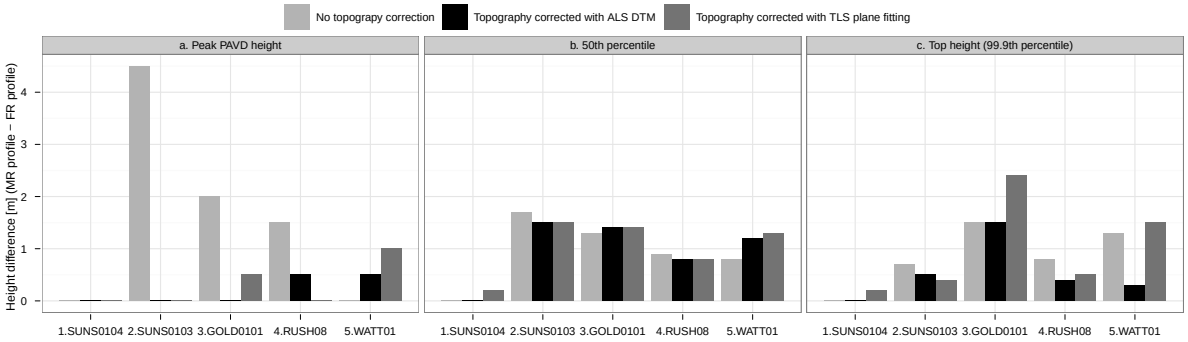


**Figure 2.10:** Difference in height metrics between multiple return (MR) vertical plant profiles and first return (FR) vertical plant profiles.

sensor configuration are similar within each site and thus independent of the topography correction. When the top canopy height metrics are derived from first return data only, differences range from 0 m to 1.5 m for a topography correction with ALS DTM, from 0.2 m to 2.4 m for a topography correction with TLS plane fitting and from 0 m to 1.5 m when topography is not accounted for.

Additional canopy top heights are available directly from the ALS data. The ALS top heights in table 2.6 represent the top height within the boundaries of the plot. The top heights from both corrected vertical plant profiles (ALS DTM and TLS plane fitting) show similar offsets compared to the ALS top heights. Compared to the top heights from both corrected profiles, the ALS top height is larger for SUNS0104 (1.6 m), SUNS0103 (0.5 m and 0.8 m) and WATT01 (0.8 m and 3.4 m), but is smaller for GOLD0101 (1.1 m and 1.5 m) and RUSH08 (0.5 m).

The TLS data was collected with 0.06° x 0.06° angular sampling for all the plots, apart

**Table 2.7:** Evaluation statistics for differences in vertical plant profiles for D'Aguilar National Park (scan position East) generated from scan data with different angular resolution. Full scan resolution is the scan data that was acquired with an angular resolution of 0.04°x0.04°; Reduction 2/5/50 is the scan data subsampled with a factor of 2/5/50.

| Topography correction | Evaluation statistic | Full resolution vs. reduction 2 | Full resolution vs. reduction 5 | Full resolution vs. reduction 50 |
|---|---|---|---|---|
| None | CV(RMSE) [%] | 0.25 | 0.83 | 11.04 |
| | Residual mean [$m^2/m^3$] | -0.0062 | 0.0030 | -0.2080 |
| | Standard deviation [$m^2/m^3$] | 0.0002 | 0.0007 | 0.0086 |
| TLS plane fitting | CV(RMSE) [%] | 0.84 | 2.12 | 15.54 |
| | Residual mean [$m^2/m^3$] | -0.0062 | 0.0026 | -0.2149 |
| | Standard deviation [$m^2/m^3$] | 0.0008 | 0.0021 | 0.0151 |
| ALS DTM | CV(RMSE) [%] | 0.25 | 0.63 | 8.78 |
| | Residual mean [$m^2/m^3$] | -0.0062 | 0.0030 | -0.2160 |
| | Standard deviation [$m^2/m^3$] | 0.0002 | 0.0006 | 0.0079 |

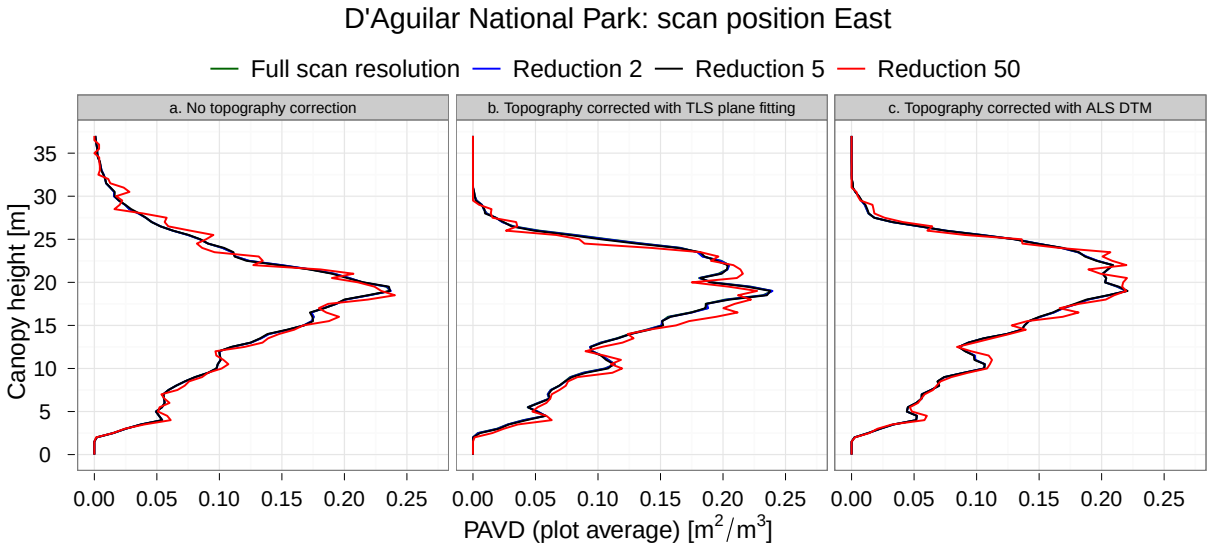


**Figure 2.11:** Vertical plant profiles for D'Aguilar National Park (scan position East) generated from scan data with different angular resolution. Full scan resolution is the scan data that was acquired with an angular resolution of 0.04°x0.04°; Reduction 2/5/50 is the scan data reduced by a factor of 2/5/50.

from the East and West scan in D'Aguilar National Park, which had a 0.04° x 0.04° angular sampling. We tested the impact of this on the calculation of the vertical plant profile. The data reduction between 0.04° and 0.06° is 1.78 and figure 2.11 shows very little difference in the profiles generated from 0.04° x 0.04° angular sampling and a subsampling with a factor of two. For topography corrected with TLS plane fitting, the evaluation statistics for in table 2.7 show a CV(RMSE) of 0.84% and residual mean of -0.0062 $m^2/m^3$ between the full resolution profile and the profile generated after reducing the data with a factor 2. There is little difference when the data is reduced by a factor 5 (CV(RMSE) of 2.12%). A reduction of a factor 50 (i.e. keeping only 2% of the data) will still follow the general shape of the vertical plant profiles, but will differ locally (residual mean of -0.2149 $m^2/m^3$ ). The profiles that are not corrected for topography or are corrected with the ALS DTM show a similar trend (table 2.7).

## 2.5 Discussion and further work

Most studies that used vertical plant profiles did not take into account topography (Lovell et al., 2011b; Jupp et al., 2009) or used data over flat terrain (Ni-Meister et al., 2010). The importance of topography for canopy structural parameters derived from TLS was raised by others (Zhao et al., 2012, 2011; Yao et al., 2011), but topography was not corrected in these studies. Recent work of Zhao et al. (2013) used a plane fitting approach through the ground points of multiple merged EVI scans to account for topography in foliage profiles

inferred from EVI point cloud data. In this work we demonstrate that topography-corrected vertical plant profiles from a single TLS scan agree significantly better with the ALS DTM corrected profiles (CV(RMSE) up to 20.6%, typically ranging from 1.5% to 12.6%) than vertical plant profiles that are not corrected for topography (CV(RMSE) up to 66.2%, typically ranging from 4.2% to 13.8%). The time of acquisition of a single scan depends on the type of instrument used. In this study the RIEGL VZ-400 is used, which takes approximately 1.5 minutes per scan. Not setting up registration targets and doing multiple scans (approximately 2-4 hours in total per plot for one centre scan and four corner scans), will allow for an increased number of sampling plots. Rapid assessment of the vertical structure will also allow for sampling larger areas with TLS and better support sustainable forest management. TLS measures a large range of zenith angles and gives a better representation of the woody component compared to airborne LiDAR. The woody component contributes most to biomass, so an increased spatial sampling might enable new opportunities in biomass assessment.

Our results demonstrate that the assumption of flat terrain for generating vertical plant profiles can lead to significant errors in derived height metrics. We applied two different topography corrections (ALS DTM and TLS plane fitting) and compared metrics derived from those corrected profiles with results from vertical profiles that have not been corrected for topography. We assume that the vertical plant profile corrected with the ALS DTM is the reference for comparing the impact of not correcting terrain versus a TLS plane fit to correct for topography. For multiple return TLS instruments, such as the RIEGL VZ-400, a TLS plane fitting correction will always give a better result than not correcting for terrain. The CV(RMSE) for WATT01, which has a slope of 6.30°, decreases from 66.2% for the uncorrected profile to 20.6% after plane fitting. This suggests that a simple plane fit will correct for 68.9% of the error in the profile. The other sites show similar results and simple plane fitting will correct for a significant part of the overall vertical plan profile bias: 40.0% for SUNS0104, 44.3% for RUSH08 and up to 77.4% for SUNS0103. GOLD0101 only shows an improvement of 8.9%. This is mainly because this site was located in a hilly environment, although the terrain in proximity of the scan locations fitted the assumption of a plane well. The site was characterised by a medium-dense herbaceous understorey, but little woody understorey. This allowed the laser pulses to penetrate well through the forest, with the 90th percentile of horizontal range from the scanner being 46 m. At this distance, it is possible that the fitted plane might not be the best approximation of the terrain and therefore the improvement in vertical plant profile correction will not be as significant. However, it is important to stress that there is still an improvement compared to not applying a terrain correction at all. We expect the assumption of a local plane fit to the terrain not to be valid in the extreme cases where the scan position is located on top of a hill or at the bottom of a valley.

The TLS plane fitting approach is robust and when topography is relatively flat with little understorey (e.g. RUSH08), the topography correction does not have a corrupting

effect on the final vertical plant profile. A dense grass cover was present in SUNS0104 and our results clearly show the advantage of having a multiple return over a first return only instrument. The iterative re-weighted least squares regression that is used for TLS plane fitting is able to correct for some erroneously categorised minimum points as described in section 2.3.2. However, a first return instrument is not able to provide a sufficient number of ground returns and this will result in a fitted plane that does not represent the terrain, but has a positive height offset. This is illustrated in figure 2.8, where the first return vertical plant profile in SUNS0104 is shifted down compared to the multiple return equivalent. It is therefore not surprising that the TLS plane fitting has a corrupting effect on first return vertical plant profiles in environments with a dense herbaceous understorey. Figure 2.10 suggests, in agreement with findings in Newnham et al. (2012a), an overall trend of lower height metrics for first return instruments compared to multiple return instruments. The RIEGL VZ-400 scanner records up to four returns, with the contribution of the first return ranging from 66.7% to 80.1% (see table 2.3). The fourth return only contributes 0.4% to 2% to the total number of returns and we therefore expect potential additional returns (5th or more) not to lead to significant improvements of our method.

Table 2.6 suggests that the 50th percentile heights, derived from multiple return TLS vertical plant profiles, are less influenced by topography than top canopy heights and peak PAVD heights. The largest disagreement in median PAVD height is in WATT01 (0.5 m) and this is reduced by 20% when a TLS plane correction is applied. The effect of this TLS plane correction is more significant for peak PAVD and top canopy heights. Applying the TLS plane fitting correction will correct for at least 77% of the top canopy height error (SUNS0103 and WATT01). This increases to 85% for GOLD0101 and up to 100% (i.e. perfect agreement with the reference profile) for the two other sites. This is significant because tree height is an important parameter for estimating AGB using allometric relationships (Chave et al., 2005; Brown et al., 1989) or large-footprint LiDAR instruments (Lefsky et al., 2005). Propagation of error by using these allometric relationships might lead to significantly wrong estimates of AGB forest carbon stock. Stark et al. (2012) demonstrated that having correct information about the vertical variation of canopy metrics is essential in estimating forest carbon dynamics and not correcting for topography might have implications for the assessment of biomass and biomass growth. Top canopy heights derived from vertical plant profiles show a small underestimation (SUNS0104, SUNS0103 and WATT01) or overestimation (GOLD0101 and RUSH08) compared to top canopy heights directly estimated from ALS (table 2.6). Direct ALS height estimates were validated against field measured predominant heights by Lovell et al. (2003). The lower top canopy heights (ranging from 0.5 m to 3.4 m) from the vertical plant profiles can be explained by the below canopy viewpoint of the TLS instrument, which often leads to occlusion of the top of canopy, and the restricted zenith range of the instrument (table 2.2). The latter can be overcome by recording an additional scan at the same location

with the instrument tilted at 90 degrees from the vertical and then registering the two scans together. This would result in a single full hemispherical scan and is subject of future work. The larger canopy heights from the vertical plant profiles for GOLD0101 and RUSH08 can be explained by tall trees outside the boundaries of the sample plot. Only trees within this boundary were used for the direct retrieval of ALS top height, whereas the vertical plant profiles for corner scan locations also included trees from outside the plot boundary. Peak PAVD height for SUNS0104 and RUSH08 shows no bias when not corrected for topography. This is likely due to a combination of relative low canopy top heights (10.0 m and 23.0 m, respectively), low PAI and low slope. We used a 0.5 m vertical bin height to generate the plant profiles and at this resolution small height disagreements will not be noted. Not correcting for topography resulted in a 3.0 m underestimation of the peak PAVD height in WATT01 and using the TLS plane correction reduced this error with 83.3%. Such topograpy correction even corrected for all peak PAVD height bias in SUNS0103 and GOLD0101.

This work demonstrated the implications of topography and sensor configuration on vertical plant profiles and their derived height metrics. We suggested a simple approach based on TLS plane fitting to correct for most of the bias introduced by topography. Future work will need to assess the impact of slope on path length and inferring gap fraction from TLS data. This impact can be quantified by separating the LiDAR view angle and leaf angle terms. España et al. (2008) suggested that path length only marginally influenced the estimation of effective LAI derived from digital hemispherical photos for low to medium slopes, but this might become an issue on steeper slopes. The issue of slope, together with the accuracy testing of the method from Jupp et al. (2009), can be tested in a simulation environment. Future work will simulate LiDAR data using the *librat* Monte Carlo ray tracing (MCRT) model. This model is based on the *ararat/drat* MCRT model (Lewis, 1999) and has been tested in previous LiDAR studies (Calders et al., 2013a; Disney et al., 2010) and against other LiDAR simulation models (Widlowski et al., 2013). Using simulations enables us to control all aspects of the environment and sensor properties, which would not be possible using measured LiDAR data. The vertical plant profiles in this work do not separate between leaf and non-leaf constituents. The separation of plant profiles into a woody and non-woody component will make it easier to link the vertical distribution of these components to processes such as radiation interception and to distinguish between woody and non-woody AGB. The recent development of dual wavelength research instruments such as SALCA (Salford Advanced Laser Canopy Analyser) and DWEL (Dual-Wavelength Echidna Lidar) are designed to improve this separation of woody and non-woody constituents (Gaulton et al., 2013; Douglas et al., 2012).

## 2.6 Conclusion

Our research demonstrates that not correcting for topography when generating vertical plant profiles can lead to significant errors in the vertical distribution of plant constituents. Ideally, a detailed DTM derived from ALS data could be used to correct for topography. Such data is often not available or expensive to acquire and we therefore suggest an alternative approach based on TLS plane fitting. This approach allows for rapid, robust and automated assessment of the vertical structure of vegetation. We derive vertical plant profiles, using the robust method from Jupp et al. (2009), for five different forest environments (PAI ranging from 0.23 to 5.84) and quantify the impact of TLS plane fitting for topography correction. We show that the overall shape of topography-corrected vertical plant profiles from a single TLS scan agrees better with the ALS DTM corrected profiles (CV(RMSE) up to 20.6%, typically ranging from 1.5% to 12.6%) than vertical plant profiles that are not corrected for topography (CV(RMSE) up to 66.2%, typically ranging from 4.2% to 13.8%). Height metrics are inferred from these vertical plant profiles and results show that not correcting for topography will lead to estimates (especially for canopy top height and peak PAVD height) that significantly depart from those that are inferred from the ALS DTM corrected reference profile. Correcting topography with a TLS plane fitting approach reduces the error in canopy top height by at least 77% and up to 100%, and reduces the error in peak PAVD height by 83.3% and up to 100%. We also highlight the advantages of a multiple return over a first return instrument. Detecting the ground returns and applying the TLS plane fitting approach might be problematic without multiple returns when the herbaceous understorey is dense. Height metrics inferred from vertical plant profiles of first return TLS data are also consistently lower compared to height metrics derived from multiple return data. We present a method that is completely data-driven and is therefore suited to be applied on current data archives such as AusCover (http://www.auscover.org.au/data/product-list). The AusCover archive provides access to remote sensing data, including TLS data over a wide range of forest types. This data is often single scan data with no survey control and our approach could be used to analyse the vertical distribution of plant constituents of these study sites.

## Acknowledgements

We thank the *Schure Beijerinck Popping Fonds, Koninklijke Nederlandse Akademie van Wetenschappen* (Grant No. SBP2012/53), for their financial support. The ALS data for Rushworth Forest and Watts Creek were obtained through AusCover. AusCover is the remote sensing data products facility of TERN (http://www.tern.org.au). We also thank D. Culvenor, J. Muir and M. Disney for their assistance with fieldwork and the anonymous reviewers for their valuable suggestions to improve the manuscript.

## 2.A Appendix: Effect of topography on $P_{gap}(\theta, z)$

Vertical plant profiles are calculated from estimates of the vertically resolved gap probability ($P_{gap}(\theta, z)$, equation 2.1) derived from TLS data (Jupp et al., 2009). The zenith angles $\theta$ are measured by the TLS instrument and $z$ is the vegetation height above the reference height. Figure A.1 shows the 2D cross section of a zenith ring ranging from zenith 1 to 2. We used zenith rings of 5 degrees in this work (see section 2.3.1). Figure A.1 illustrates that not correcting for height will not influence the total gap fraction as a function of zenith angle ($P_{gap}(\theta)$), but estimates of $P_{gap}(\theta, z)$ may be different to $P_{gap}(\theta, h)$. In other words, the total PAI would be the same for the corrected or uncorrected heights since it is the integral of the whole canopy, but vertical plant profiles would be different (Zhao et al., 2013). Total PAI is the integral of the vertical plant profile. If we do not correct for topography, we would essentially have $P_{gap}(\theta, h)$ with height values referenced to a horizontal plane at the instrument height and not $P_{gap}(\theta, z)$ with height values referenced to the true topography. The latter is essential for generating the vertical plant profiles, which represent the 3D distribution of canopy elements with respect to the terrain height (z(x,y)=0 in Fig A.1). It is important to note that zenith angles do not change due to topographic correction so total gap fraction calculations also do not change, i.e. $P_{gap}(\theta, z = max(z))$ equals $P_{gap}(\theta, h = max(h))$.

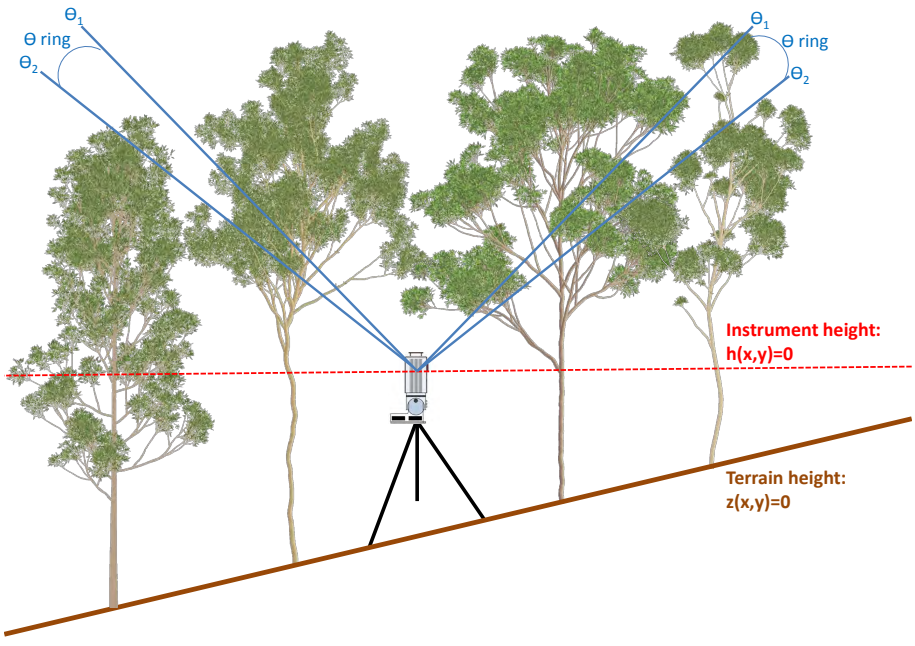


**Figure A.1:** 2D Illustration of terrestrial LiDAR height recordings on sloped terrain. Heights are recorded with respect to the origin of the instrument (red line) and not to the true topography (brown line). The blue lines represents a cross section of a zenith ring. Such zenith rings are used to calculate the vertically resolved gap fraction.

# Chapter 3

# Monitoring spring phenology with terrestrial LiDAR

This chapter is based on:

Calders, K., Schenkels, T., Bartholomeus, H., Armston, J., Verbesselt, J. and Herold, M. Monitoring spring phenology with high temporal resolution terrestrial LiDAR measurements. *Agricultural and Forest Meteorology*, in review.

***Abstract:*** Vegetation phenology studies the timing of recurring seasonal dynamics and can be monitored through estimates of plant area index (PAI). Shifts in spring phenology are a key indicator for the effect of climate change, in particular the start of the growing season of forests. Terrestrial laser scanning(TLS), also referred to as terrestrial LiDAR, is an active remote sensing technique and measures the forest structure with high spatial detail and accuracy. TLS provides information about the 3D distribution of canopy constituents and vertical plant profiles can be derived from these data. Vertical plant profiles describe the plant area per unit volume as a function of height, and can be used to used to monitor seasonal dynamics through PAI. Here, we present a TLS time series based on 48 measurement days of four sampling locations in a deciduous forest in the Netherlands. Vertical plant profiles are derived for each measurement and allow us to quantify not only total canopy integrated PAI, but also monitor PAI at specific horizontal layers. Sigmoidal models show a good fit to the derived total canopy integrated PAI time series (CV(RMSE) $< 2.4\%$ and CCC $> 0.99$). The start of season (SOS) based on these models occurs between March 29 and April 3, 2014, depending on the species composition. The SOS derived from the TLS data occurs earlier compared to the prediction based on meteorological data, which is likely the result of winter and spring warming. TLS allows us to monitor PAI at specific horizontal layers and we defined an understorey, intermediate and upper canopy layer. Even though our study area had only a sparse understorey, small differences are observed in the SOS between the different layers. We expect that these phenological differences will be more pronounced in multi-layered forests and TLS shows the potential to study seasonal dynamics not only as a function of time, but also as a function of canopy height.

## 3.1 Introduction

The structure of forests impacts several biological and physical processes. The structural arrangement of canopy constituents within forests influences respiration, transpiration, photosynthesis, carbon and nutrient cycles and rainfall interception. Furthermore, the vertical structure of vegetation is also related to biological diversity and habitat availability (Tanaka et al., 2010; Goetz et al., 2007; Holmes & Sherry, 2001). Phenology studies the periodic biological cycles and seasonal changes in forest structure generally follow a well-defined temporal pattern (Zhang et al., 2003b). In general, spring activities (e.g. shooting and flowering of vegetation) have occurred progressively earlier since the 1960s (Walther et al., 2002; Hamunyela et al., 2013). Monitoring phenological dynamics provides information about how these recurring biological cycles are connected to the climate and are responding to climate change (Polgar & Primack, 2011; White et al., 2009).

The leaf area index (LAI) is commonly used to quantify forest structure and monitor seasonal dynamics (Bequet et al., 2011; Garrity et al., 2011). However, because most indirect methods do not differentiate between different constituents in the canopy (e.g. stem, branches, leaves), plant area index (PAI) is a more correct term. PAI is defined as the one-sided area of plant material surface per unit ground surface area. The indirect ground-based assessment of PAI in the field has been done with optical instruments (Parker et al., 1989), and, more recently, terrestrial LiDAR (light detection and ranging) instruments. Hemispherical photography is an indirect optical method that is commonly used to estimate PAI to quantify structural information about the canopy architecture (Bequet et al., 2011; Jonckheere et al., 2004). This technique is based on the light attenuation and contrast between elements in the photo to differentiate between sky and canopy elements. Methodological errors can occur at any stage of image capture and analysis and the inferred PAI values are therefore subject to several potential error sources (Jonckheere et al., 2004). The LAI-2000 (Li-Cor, Inc., Lincoln, NE) is another indirect optical method to measure PAI. This method is based on the principle of calculating the transmittance based on the ratio of measurements below and outside the canopy (Jonckheere et al., 2004; Gond et al., 1999). The LAI-2000 tends to underestimate PAI in heterogeneous canopies and its coarse resolution restricts detailed spatial analysis of the canopy constituents distribution (Jonckheere et al., 2004).

LiDAR is an active remote sensing technique that accurately measures distances by transmitting laser pulses and analysing the returned energy as a function of distance or time. Terrestrial laser scanning (TLS), also called terrestrial LiDAR, collects information about the three-dimensional distribution of plant constituents in the canopy and can assess forest structure (Ashcroft et al., 2014; Calders et al., 2014; Vaccari et al., 2013). Previous studies presented fully automated and objective methods to derive forest structure from terrestrial LiDAR data (Calders et al., 2014; Newnham et al., 2012a; Lovell et al., 2011a; Jupp et al., 2009; Danson et al., 2007). The robustness of PAI estimates is critical when

comparing temporal measurements for monitoring seasonal dynamics in phenology. PAI estimates from hemispherical photography were found to be less robust and more susceptible to methodological errors than estimates from TLS (Hancock et al., 2014; Jonckheere et al., 2004).

Vertical profiles of gap fraction and plant area are important structural metrics to quantify the canopy structure and can be derived from TLS (Calders et al., 2014; Ni-Meister et al., 2010; Jupp et al., 2009). The vertical distribution of plant area volume density (PAVD) as a function of canopy height was calculated through estimates of the vertically resolved gap fraction. Vertical plant profiles can be used to derive PAI, but also other various metrics such as tree height, height of maximum density or the canopy base height. LiDAR derived plant profiles provide a means not only to calculate integrated canopy metrics, such as PAI, but also a means to quantify the PAI of a specific horizontal canopy layer. This can be important for monitoring multi-layered forests, where the start of the growing season in the lower canopy layers can occur at an earlier time than the upper canopy layers (Richardson & O'Keefe, 2009; Gond et al., 1999).

Previous studies used a limited number of samples to monitor spring phenology using PAI (Bequet et al., 2011; Calders et al., 2011). To our knowledge, this paper is the first that analyses spring phenology with high temporal resolution 3D measurements. In this paper we collect terrestrial LiDAR time series data in a broadleaf deciduous forest to monitor leaf development during the period February-July. We will create vertical plant profiles from TLS and monitor the forest structure and the phenological changes during this period. The main objectives of this paper are:

1. Monitoring changes in total canopy integrated PAI using TLS from leaf-off conditions in winter to a fully developed canopy in summer;
2. Monitoring PAI dynamics in specific horizontal canopy layers using TLS derived vertical plant profiles; and
3. Comparing the start of season inferred from TLS and meteorological data.

This work provides insight in the stability of TLS measurements in the context of repeatable measurements, which is important to monitor subtle changes in forest structure. We explore the potential of terrestrial LiDAR for monitoring changes in phenology at plot level scale, which may contribute to more objective calibration and validation of large scale remote sensing product.

## 3.2 Study Area and Data Collection

### 3.2.1 Study area

Terrestrial LiDAR data were acquired in *Dassenbos*, a broadleaf deciduous forest in Wageningen, the Netherlands (51.9829°N, 5.6558°E). The terrain had little to no topographic relief. Four sample locations (location A, B, C and D) were established and data were collected on 48 measurements days during the period February - July 2014. The forest was oak-dominated (*Quercus* spp.) with a presence of birch (*Betula* spp.) in the upper canopy, and is approximately 40 years old. The upper canopy of location A and B consisted of approximately 85% oak and 15% birch, whereas location C and D consisted of approximately 95% oak and 5% birch. The sparse understorey mainly consisted of *Sambucus nigra*, *Sorbus aucuparia*, *Prunus* spp., *Amelanchier* spp. and *Ilex aquifolium*. The measurement period started at day of year (DOY) 55 and continued until DOY 191. The sampling intensity varied according to the expected changes in phenology, with more weekly measurements days in periods of larger phenological changes (table 3.1).

### 3.2.2 LiDAR data

TLS data were acquired with a RIEGL VZ-400 terrestrial laser scanner (RIEGL Laser Measurement Systems GmbH), mounted on a tripod at approximately 1.45 m height. The instrument has a beam divergence of nominally 0.35 mrad and operates in the infrared (wavelength 1550 nm) with a range up to 350 m. The instrument also measures the yaw (through an internal compass) and the pitch and roll (through inclination sensors) and records up to four returns per emitted pulse. Lovell et al. (2003) and Calders et al. (2014) discussed the advantage of multiple returns over single returns. Their studies concluded that multiple return instruments will lead to an improved sampling at greater heights in the canopy. The scanner settings were the same across all scans and are summarised in table 3.2. The RIEGL VZ-400 instrument has a zenith angle range of 30 to 130 degrees. Therefore an additional scan was acquired at each sampling location with the scanner

**Table 3.1:** Sampling interval and intensity for TLS data collection.

| Start week[1] | # weeks | # measurements per week |
|---|---|---|
| 9 | 12 | 3 |
| 21 | 4 | 2 |
| 25 | 4 | 1 |

[1] week 9 starts on Feb 24, 2014 (DOY 55); week 21 starts on May 19, 2014 (DOY 139); week 25 starts on June 16, 2014 (DOY 167)

**Table 3.2:** RlEGL VZ-400 scanner settings for data acquisition of a single scan.

| | |
|---|---|
| Pulse repetition rate | 300 kHz |
| Minimum range | 0.5 m |
| Azimuth angle range | 0° - 360° (0.06° angular sampling) |
| Zenith angle range | 30° - 130° (0.06° angular sampling) |
| Acquisition time | 1 minute 23 seconds |

tilted at 90 degrees from the vertical to sample a full hemisphere. These two scans were registered by using reflecting targets that were distributed around the sample location using the RiSCAN PRO software (provided by RIEGL). We converted the raw TLS data to the sorted pulse data (SPD) format with the open source sorted pulse data software library (Bunting et al., 2013b,a) for further analysis.

### 3.2.3 Meteorological data

Hourly measurements of temperature and wind speed were available from a fully automated weather station, located to the West of Wageningen (weather station *Veenkampen*, 51.9808°N, 5.6217°E) at approximately 2.4 km from the study area. Minimum and maximum temperature (°C) were measured at 1.5 m. Hourly mean temperatures were averaged to calculate the average daily temperature (WMO, 2011). Mean and maximum wind speed (m/s) were measured at 10 m. Weather station *Veenkampen* provided meteorological data dating back to January 2012. The nearby weather station *Haarweg* (51.9707°N, 5.6426°E) was operational from 2001 until the end of 2011 and collected similar meteorological data.

## 3.3 Methods

### 3.3.1 Vertical plant profiles

We quantified the vertical forest structure by the plant area volume density (PAVD) as a function of canopy height. These vertical plant profiles were calculated from TLS data through estimates of the vertically resolved gap probability ($P_{gap}$). We used the approach described in Calders et al. (2014), which was tested in different forest types with different topography and understorey. Here, we extended that work by generating profiles that cover the 5-70° zenith angle range. The RIEGL instrument does not take a full hemispherical scan, but this is achieved by taking two separate scans (see section 3.2.2). The scan in upright position was used for the 35-70° zenith angle range and the 90 degrees tilted scan was used for the 5-35° zenith angle range.

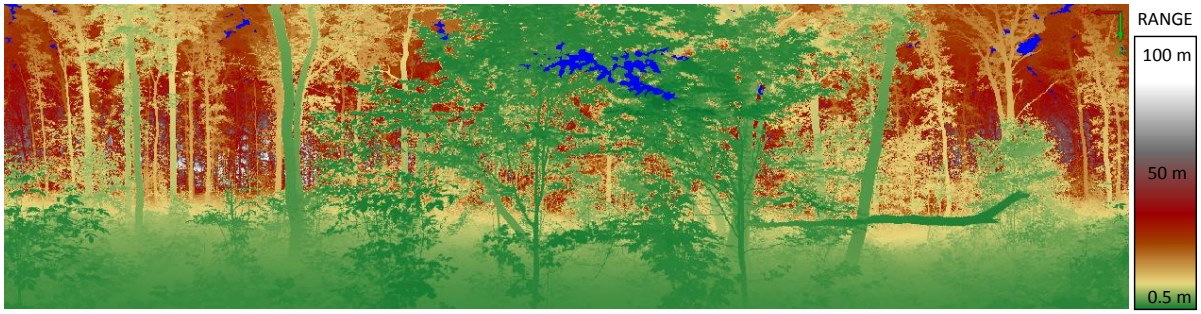


**Figure 3.1:** TLS data for location A on June 10, 2014 (DOY 161) in a cylindrical projection (instrument in upright position). The azimuth angle range is 0 to 360° and the zenith angle range is 30 to 130°, with the top-left corner of the image being azimuth 0° and zenith 30°. The data is coloured according to range. Blue means that no returns have been registered because there is no target or the target is too close (< 0.5 m) to the instrument.

We describe the basic steps of this approach below, but the reader is referred to Calders et al. (2014) for full details of the method:

1. Topographic effects were corrected in the TLS data by local plane fitting. Ground returns were classified in the TLS data and used in an iterative re-weighted least squares (IRLS) regression to define the plane parameters.

2. The vertically resolved gap probability from a multiple return is approximated as:

$$P_{gap}(\theta, z) = 1 - \frac{\sum w_i(z_i<z, \theta)}{N(\theta)} \qquad (3.1)$$
$$w = 1/n_s$$

   $z$ is the height above the instrument optical centre ($z_0$) and $\theta$ is the zenith angle of the laser pulse. The numerator in equation 3.1 gives the number of laser returns that are below $z$ and $N(\theta)$ is the total number of outgoing laser pulses for a finite zenith angle range centered around $\theta$. We make the assumption that for a specific transmitted laser pulse each return equates to a beam area interception of $1/n_s$, where $n_s$ is the number of total returns for that transmitted laser pulse.

3. Vertical plant profiles were derived from the vertically resolved gap probability ($P_{gap}$) using the method of Jupp et al. (2009), which uses a solid-angle-weighted normalised profile:

$$f(z) = PAI \frac{\delta}{\delta z} \left( \frac{log(P_{gap}(\overline{\theta}, z))}{log(P_{gap}(\overline{\theta}, H))} \right) \qquad (3.2)$$

   $H$ is the height at which the laser pulse exits the canopy and $\overline{\theta}$ means that the normalised data are averaged over a zenith ring instead of being a mean angle. The vertical plant profile, $f(z)$, is largely independent of clumping and is derived from

the approximated PAI at 57.5°. This angle is the "hinge angle", at which the foliage orientation function is essentially invariant at 0.5 over different leaf angle distributions (Ross, 1981). The zenith ring between 55° and 60° is used to approximate the hinge region (Jupp et al., 2009; Zhao et al., 2011).

The minimum range of the RIEGL VZ-400 is 0.5 m (table 3.2). Location A had a single branch that was closer than 0.5 m after leaf development. The returns from this branch were not recorded and no returns were registered in the point cloud for these transmitted pulses (figure 3.1). Because the branch was located in the hinge region, this led to an increased $P_{gap}$ and therefore a drop in PAI. We have masked this azimuth region in the data processing of location A and have generated the profiles for the azimuth region excluding azimuth range 115 to 245°.

The integral of PAVD as a function of canopy height is the PAI. PAI values at different horizontal layers can easily be calculated from these profiles. We used three different layers: 0-5 m, 5-15 m and above 15 m. The first layer represents the (sparse) understorey, the second layer is an intermediate layer and the third layer is the upper canopy.

### 3.3.2 Monitoring phenology with TLS data

Sigmoidal models are commonly used to describe the temporal patterns in vegetation phenology in spring (Che et al., 2014; Garrity et al., 2011; Zhang et al., 2003b). The typical "S-curve" in deciduous vegetation is characterised by a period of rapid growth and convergence towards a stable plateau of maximum PAI and is described as a logistic function:

$$y(t) = \frac{U - L}{1 + e^{-k(t-t_m)}} + L \tag{3.3}$$

where $y(t)$ is the fitted PAI value as a function of time and $t$ is the time in days. $U$ is the upper asymptote and $L$ is the lower asymptote of the sigmoidal model, $k$ is the growth rate and $t_m$ is the inflection point at which the growth rate reaches its maximum value (Yin et al., 2003). In theory, the lower asymptote corresponds to the PAI in leaf off conditions. We determined the start of the growing season (SOS) at the time where the PAI value inferred from the logistic function (equation 3.3) exceeds the upper limit of the 95% prediction interval of the lower asymptote (Che et al., 2014). We used the nonlinear least-squares estimation in R (*nls* function) (R Development Core Team, 2011; Bates & Watts, 1988) to estimate the parameters of the sigmoidal model and their prediction intervals. The coefficient of variation of the RMSE, CV(RMSE), and the concordance correlation coefficient, CCC, were calculated to evaluate the goodness of fit. CV(RMSE) is defined as the RMSE normalised to the mean of the measured values and this measure has been successfully used to compare non-linear model estimates (Calders et al., 2013a). CV(RMSE) is, unlike the RMSE, unitless and this allows values to be easily compared

to one another when absolute values are not directly comparable. CCC ranges between -1 (perfect discordance) and 1 (perfect concordance) and computes the agreement on a continuous measure obtained by two methods (Lin, 1989).

### 3.3.3 Inferring start of season from meteorological data

The physiological processes that trigger leaf onset are complex. Several models of leaf onset are available, but there is no consensus on which modelling approach is best (Richardson & O'Keefe, 2009; Botta et al., 2000). Temperature has been related to bud development from early on and later other factors such as light availability and chilling conditions were incorporated. Jeong et al. (2012) and Chiang & Brown (2007) found that the start of season for oak and birch are best described by models including a chill requirement. In this study we used a commonly used model that combines heat and chill requirements and adopted the parameters described in Botta et al. (2000). The accumulated heat is described by growing degree days ($GDD$) and is defined as the sum of daily average temperature ($T$) above an arbitrary threshold ($T_{th}$) starting from January 1:

$$GDD_{Jan}(t) = \sum_{Jan1}^{t} max(T - T_{th}, 0) \tag{3.4}$$

We used a threshold $T_{th}$ of 5°C (Bequet et al., 2011; Jeong et al., 2012; Botta et al., 2000). The number of chill days ($NCD$) is defined as the number of days with a daily average temperature below $T_{th}$ starting from November 1 in the previous calendar year. The start of the season can then be defined as the day that

$$GDD_{Jan}(t) \geq a + be^{cNCD_{Nov}(t)}, \text{ with } c < 0 \tag{3.5}$$

Botta et al. (2000) defined the parameters in equation 3.5 for a cool deciduous broadleaf forest as following: $a$ = -68, $b$ = 638 and $c$ = -0.010 ($r^2$ = 0.59).

## 3.4 Results

Vertical plant profiles were inferred from TLS data and figure 3.2 shows the TLS data and vertical plant profiles for three different dates for location C. PAI was derived for a total of 48 vertical profiles per location, from leaf-off conditions in February to a fully developed canopy in July. Figure 3.3 shows the PAI temporal pattern for the four measurement locations. Sigmoidal models (equation 3.3) were fitted through these TLS derived PAI values in figure 3.4(a) to evaluate spring phenology. These models showed good agreement with the data for all plots (table 3.3), with CV(RMSE) ranging from 1.5 to 2.4% and CCC being close to 1.

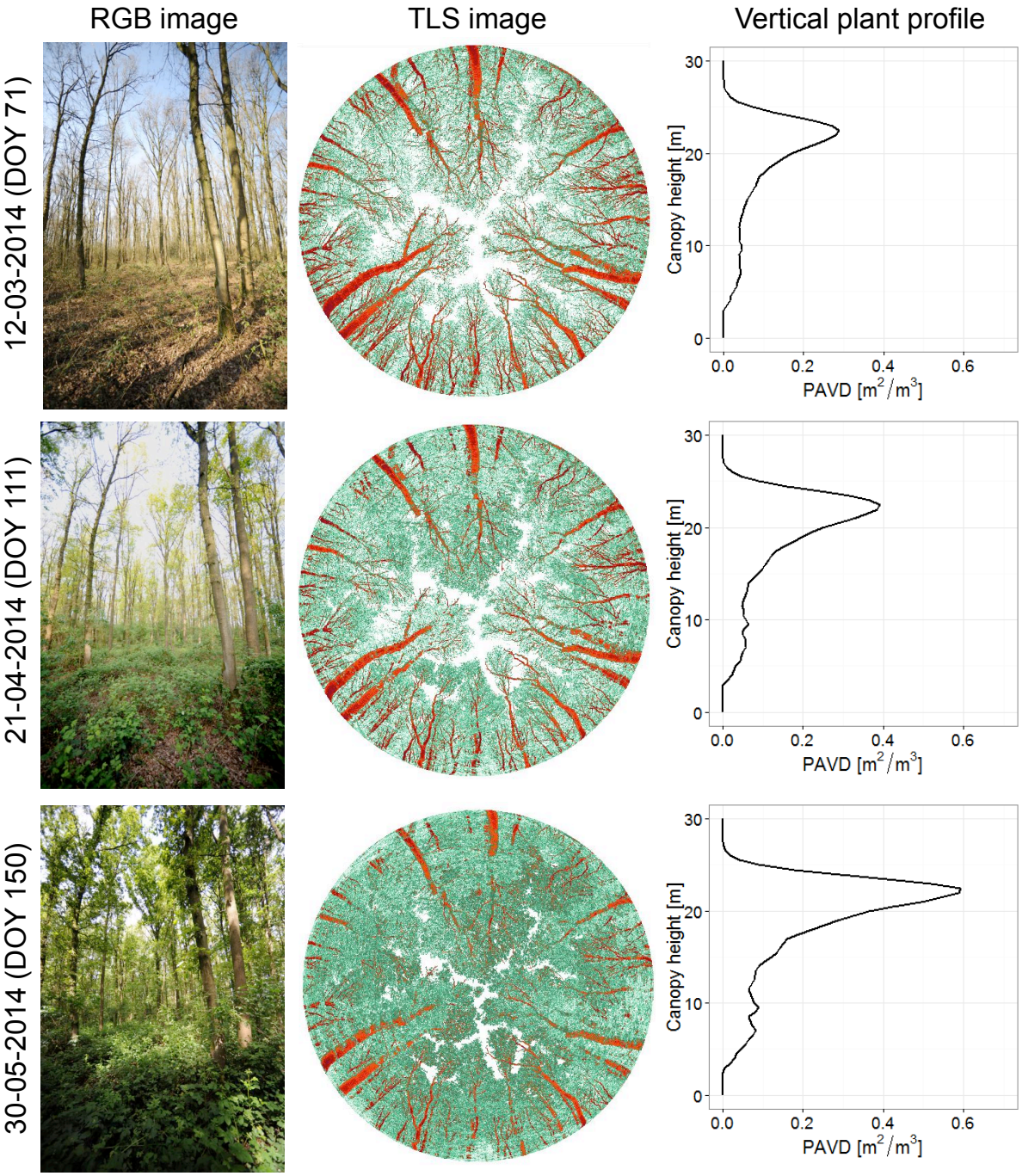


**Figure 3.2:** RGB image, TLS data and vertical plant profiles for three dates at location C. The TLS data is visualised in a polar projection and is coloured according to apparent reflectance $\rho_{app}$ (light green = low $\rho_{app}$, dark red = high $\rho_{app}$). Jupp et al. (2009) defined $\rho_{app}$ as the reflectance of a diffuse target filling the laser beam that would return the same amount of intensity as the actual target.

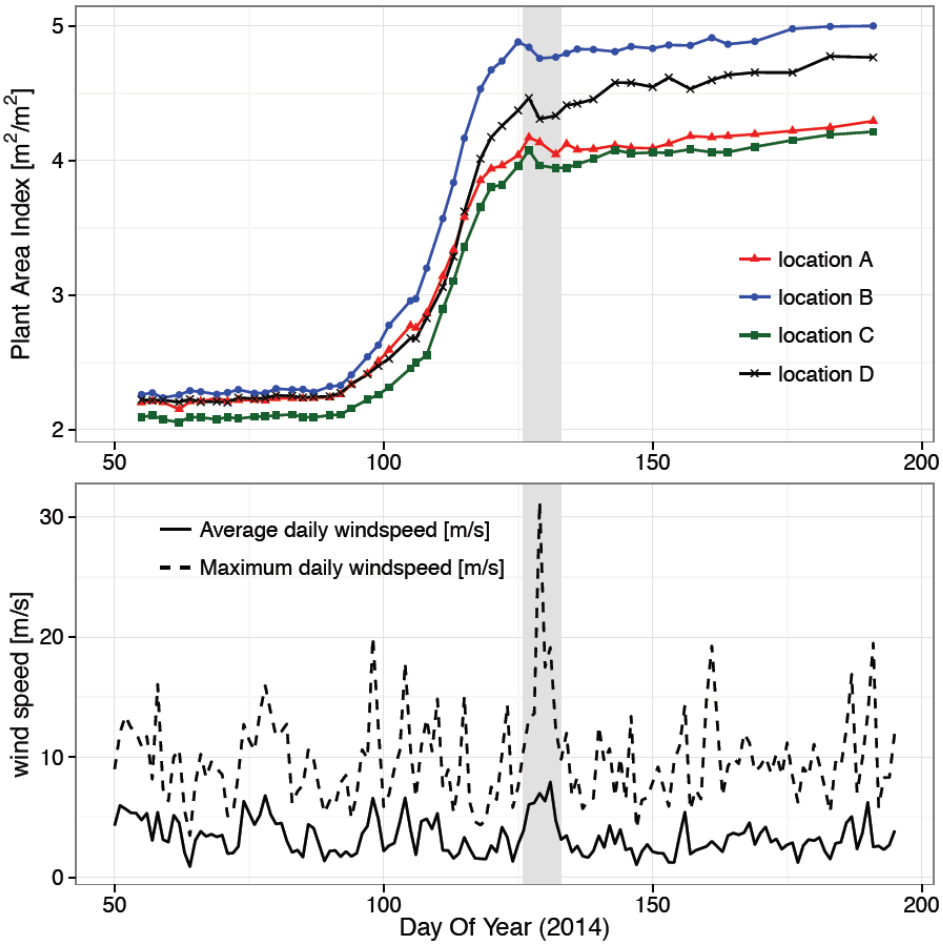


**Figure 3.3:** Total PAI measurements derived from TLS vertical profiles for the four study locations (top panel) and wind speed (bottom panel) as a function of DOY for 2014.

Based on the difference between the upper model asymptote $U$ and the lower asymptote $L$, the increase in total PAI in spring was 1.95 for location A, 2.60 for location B, 1.98 for location C and 2.36 for location D. An unexpected decrease in PAI was observed during the period around DOY 126 to 133 at all four locations. Figure 3.3 suggests that this was caused by a decreasing PAI growth rate in a period with extreme wind speeds. We recorded high average daily wind speeds during this period and a significant peak

**Table 3.3:** Parameter estimates from the sigmoidal fit (equation 3.3) to the TLS data.

| Location | CV(RMSE) [%] | CCC | $L$ | $U$ | $k$ | $t_m$ [DOY] | $SOS_{mod}$[1][DOY] |
|---|---|---|---|---|---|---|---|
| A | 1.5 | 0.998 | 2.22 (2.19; 2.24)[2] | 4.17 (4.14; 4.20) | 0.18 (0.17; 0.20) | 111 (110.1; 111.3) | 88 |
| B | 1.7 | 0.998 | 2.29 (2.25; 2.32) | 4.89 (4.86; 4.93) | 0.20 (0.19; 0.22) | 110 (109.9;110.9) | 90 |
| C | 1.6 | 0.998 | 2.10 (2.07; 2.12) | 4.08 (4.05; 4.10) | 0.21 (0.19;0.24) | 113 (112.1;113.0) | 93 |
| D | 2.4 | 0.997 | 2.23 (2.19; 2.27) | 4.59 (4.55; 4.63) | 0.18 (0.16;0.21) | 113 (112.6;114.0) | 91 |

[1] $SOS_{mod}$ = start of season inferred from logistic model
[2] 95% prediction interval (lower limit; upper limit)

in maximum daily wind speed of more than 30 m/s on DOY 129. The forest gradually recovers from this wind event, until it reaches a more stationary PAI value. Figure 3.4(a) suggests a further, more moderate, increase in PAI for the last three measurement days (DOY 176, 183 and 191) in all plots after reaching this more stable period of the upper asymptote.

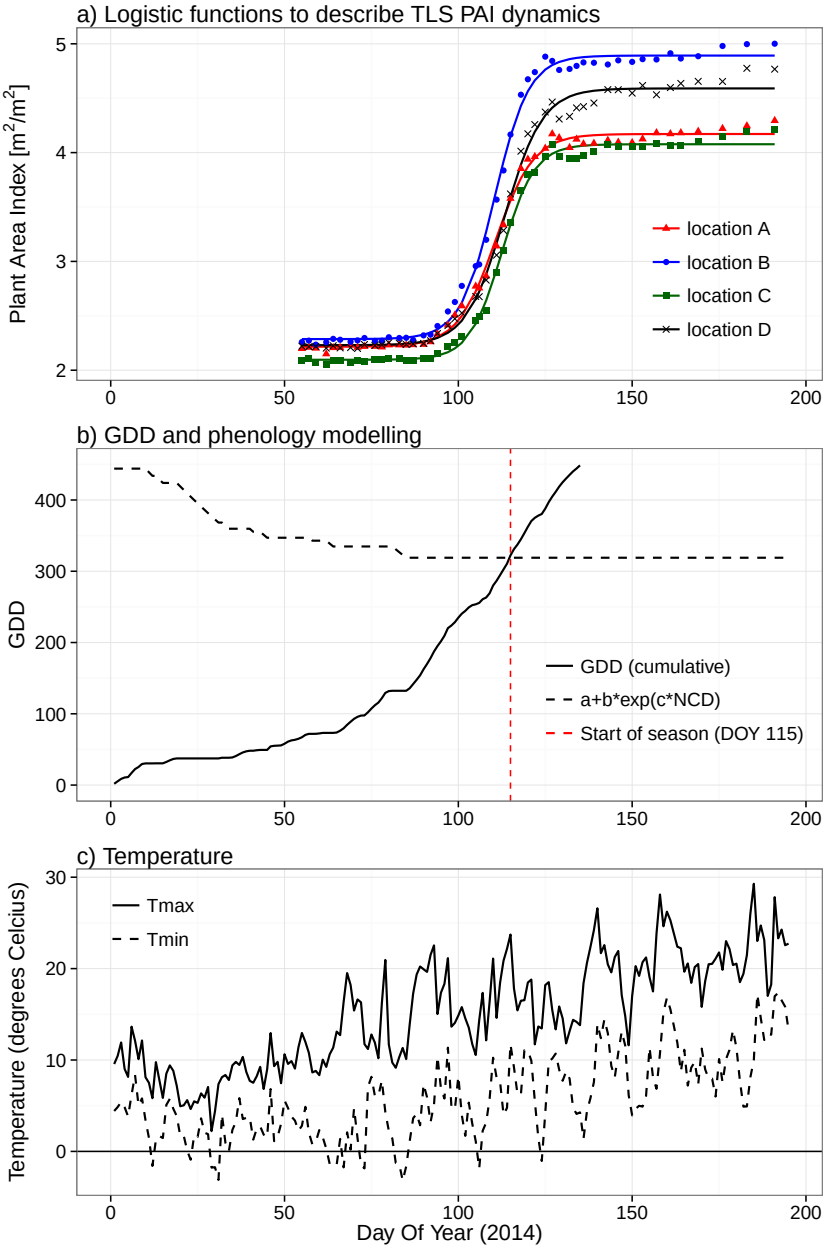


**Figure 3.4:** Phenology dynamics in spring 2014. Panel (a) shows the TLS derived PAI values and the sigmoidal fit (equation 3.3) to the TLS data. Panel (b) shows the GDD and right hand of equation 3.5 [GDD = growing degree days; NCD = number of chill days]. Panel (c) shows the maximum and minimum daily temperature.

The start of the growing season was determined at the time where the PAI value inferred from the logistic function (equation 3.3) exceeded the upper limit of the 95% prediction interval of the lower asymptote ($SOS_{mod}$). Location A showed the first significant increase in PAI on March 29 (DOY 88), followed by location B two days later, location D three days later and finally location C five days later (table 3.3). The inflection point $t_m$ indicates the day of maximum growth rate. This day was observed 20 (location B and C), 22 (location D) and 23 (location A) days after the start of season. The growth rate $k$ ranged from 0.18 to 0.21.

Vertical plant profiles describe the PAVD as a function of canopy height and we can therefore look at the PAI dynamics at different horizontal layers in the canopy (figure 3.5, table 3.4). The intermediate and upper canopy layer show a good agreement with the sigmoidal model. The CV(RMSE) values range between 1.2 and 2.3% and the CCC is close to 1, suggesting a good agreement between the TLS PAI and the fitted sigmoid model. The CV(RMSE) of the understorey layer is higher and ranges from 5.1 to 14.0%. Even though the CCC values (0.94 to 0.99) suggest that a sigmoidal model is a good fit, visual inspection of figure 3.5 shows that whilst this might be a reasonable overall fit, the local agreement was poor. This makes it problematic to infer the start of season from the sigmoidal model. We therefore used another approach to determine SOS for

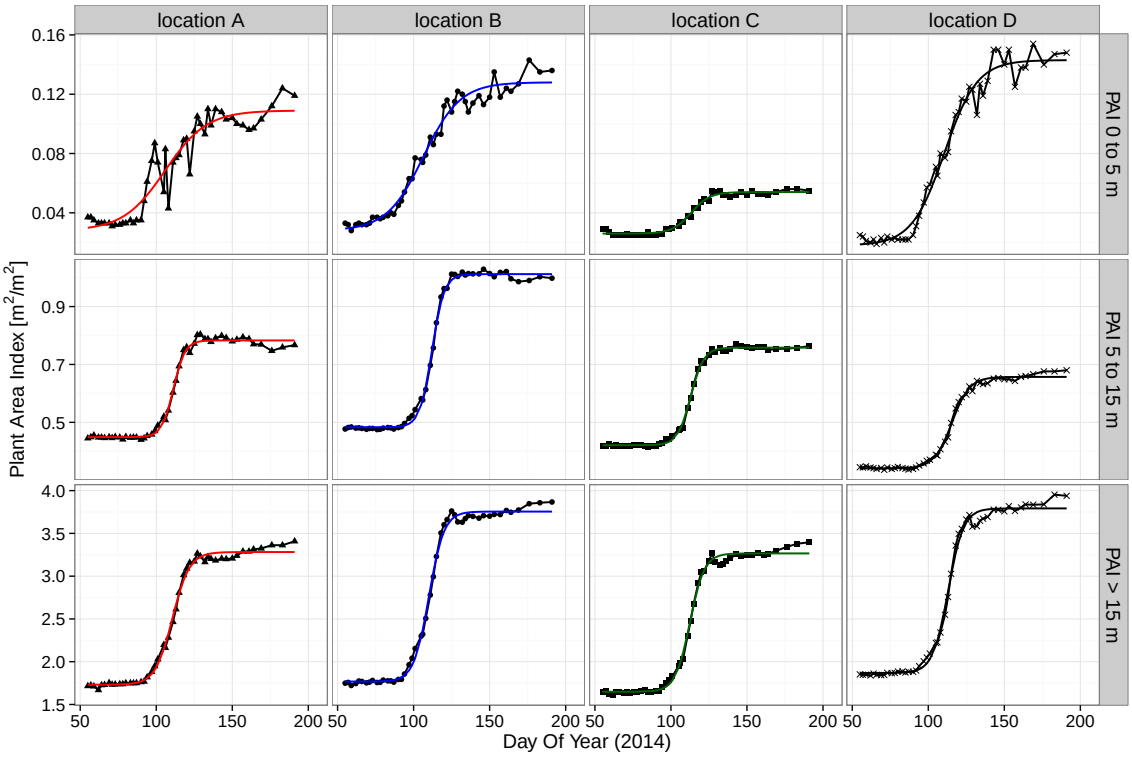


**Figure 3.5:** Phenology dynamics in spring 2014 at different horizontal layers through TLS derived PAI values and a sigmoidal fit (equation 3.3) to the data.

**Table 3.4:** Parameter estimates from the sigmoidal fit (equation 3.3) to the TLS data at different horizontal layers.

| Location | Layer [m] | CV(RMSE) [%] | CCC | $L$ | $U$ | $k$ | $t_m$ [DOY] | $SOS_{mod}$[1]($SOS_{thres}$)[2] [DOY] |
|---|---|---|---|---|---|---|---|---|
| A | 0-5 | 14.0 | 0.945 | 0.03 (0.01; 0.04)[3] | 0.11 (0.10; 0.12) | 0.07 (0.04; 0.11) | 106 (98.8; 112.3) | 77 (92) |
| | 5-15 | 2.0 | 0.997 | 0.45 (0.44; 0.45) | 0.78 (0.78; 0.79) | 0.26 (0.23; 0.30) | 111 (110.7; 111.9) | 96 |
| | > 15 | 1.9 | 0.998 | 1.73 (1.70; 1.76) | 3.28 (3.26; 3.31) | 0.18 (0.16; 0.20) | 111 (110.0; 111.3) | 88 |
| B | 0-5 | 7.4 | 0.989 | 0.03 (0.02; 0.03) | 0.13 (0.12; 0.13) | 0.08 (0.07; 0.10) | 107 (104.0; 109.0) | 72 (90) |
| | 5-15 | 1.6 | 0.999 | 0.48 (0.48; 0.49) | 1.01 (1.01; 1.02) | 0.25 (0.23; 0.27) | 112 (111.7; 112.5) | 95 |
| | > 15 | 2.0 | 0.998 | 1.77 (1.74; 1.80) | 3.76 (3.73; 3.78) | 0.20 (0.18; 0.23) | 110 (109.5; 110.6) | 90 |
| C | 0-5 | 5.1 | 0.992 | 0.03 (0.02; 0.03) | 0.05 (0.05; 0.05) | 0.16 (0.14; 0.20) | 113 (112.0; 114.6) | 90 (97) |
| | 5-15 | 1.2 | 0.999 | 0.42 (0.42; 0.42) | 0.76 (0.75; 0.76) | 0.23 (0.21; 0.25) | 113 (112.6; 113.4) | 93 |
| | > 15 | 1.9 | 0.998 | 1.65 (1.63; 1.65) | 3.27 (3.24; 3.29) | 0.21 (0.19; 0.24) | 112 (111.9; 113.0) | 93 |
| D | 0-5 | 8.8 | 0.991 | 0.02 (0.01; 0.02) | 0.14 (0.14; 0.15) | 0.09 (0.08; 0.11) | 111 (108.5; 112.8) | 76 (92) |
| | 5-15 | 1.9 | 0.998 | 0.34 (0.34; 0.35) | 0.66 (0.65; 0.66) | 0.17 (0.15; 0.19) | 116 (114.9; 116.2) | 92 |
| | > 15 | 2.3 | 0.997 | 1.87 (1.84; 1.90) | 3.80 (3.76; 3.83) | 0.20 (0.17; 0.23) | 113 (112.4; 113.7) | 93 |

[1] $SOS_{mod}$ = start of season inferred from logistic model
[2] $SOS_{thres}$ = start of season from thresholding method (0 - 5 m layer only)
[3] 95% prediction interval (lower limit; upper limit)

the understorey layer. We assumed that the earliest possible start of the understorey layer SOS is the SOS of the vertically integrated canopy (table 3.3). We determined the maximum TLS PAI understorey value before this earliest possible start and determined the SOS ($SOS_{thres}$) for this layer as the first date at which this maximum threshold value was exceeded by the TLS PAI values.

The start of season at location A was first triggered in the upper canopy (DOY 88), followed by the understorey two days later and no significant changes appeared in the intermediate layer until DOY 96. The understorey and upper canopy layer at location B showed a significant increase in PAI on the same day, followed by changes in the intermediate layer five days later. A different pattern was observed for location C, where the intermediate and upper canopy layer started the same date, followed by changes in the understorey only four days later. Changes in location D all happened within a day (DOY 92-93). The SOS for location D based on the integrated canopy was DOY 91, which is a day earlier than any of the three layers. This is likely because the $SOS_{mod}$ uses the continuous logistic model, whereas the $SOS_{thres}$ method uses the discrete TLS PAI time series and SOS can only be associated with measurement days. Measurements were done at DOY 90 and 92, but not at DOY 91.

Figure 3.4 compares the SOS inferred from the LiDAR PAI time series data with the SOS inferred from phenological models that take into account heat and chilling requirements. Figure 3.4(c) shows the daily maximum and minimum temperature and figure 3.4(b) shows the growing degree days (GDD) and the right hand side of equation 3.5. The intersection of these two lines at DOY 115 determine the start of season according to the phenological model, which is 22 to 27 days later than observed in the PAI time series data (figure 3.4(a) and table 3.3).

## 3.5 Discussion

Our results demonstrated that TLS instruments provide stable and repeatable measurement of PAI, and are therefore well suited to monitor temporal changes (figure 3.4(a) and 3.5). The sampling locations were permanently marked in the field, but the tripod (at approximately 1.45 m height) and TLS instrument had to be set up on each measurement day.

Previous studies have commonly used sigmoidal models to monitor vegetation phenology using data captured from optical spaceborne instruments. Zhang et al. (2003b) and Garrity et al. (2011) used vegetation indices derived from MODIS (Moderate Resolution Imaging Spectroradiometer) and Che et al. (2014) used MODIS and AVHRR (Advanced Very High Resolution Radiometer) PAI datesets. Our results demonstrated that PAI time series inferred from terrestrial LiDAR can be described with sigmoidal models with a CV(RMSE) ranging between 1.5 and 2.4% (figure 3.4 and table 3.3). One key parameter that can be derived from these phenological time series and their sigmoidal models is the start of the growing season. Detecting SOS is crucial for monitoring responses of terrestrial ecosystems to climate change (Richardson et al., 2013; Polgar & Primack, 2011; Walther et al., 2002) and we presented a robust and repeatable approach based on TLS data to derive SOS. We determined the SOS inferred from the TLS time series to range between March 29, 2014 (location A, DOY 88) and April 3, 2014 (location C, DOY 93). The difference in the start of season between these two locations is probably due to the different species composition. Although all locations were located in the same forest, location A had an oak to birch ratio of 85:15, whereas location C had a ratio of 95:5. Birch generally has an earlier SOS than oak (Fu et al., 2012; Richardson & O'Keefe, 2009) and it is therefore not surprising that the locations with a higher percentage of birch have an earlier SOS. The increase in PAI after reaching the upper asymptote is similar to the results in Bequet et al. (2011). Figure 3.5 suggests that this moderate increase at the last three measurement days is mainly occurring in the upper canopy layer. The sigmoidal model worked well to capture the spring dynamics, but different models, e.g. a series of piecewise logistic functions of time (Zhang et al., 2003b), are needed to model the whole phenological cycle.

Bequet et al. (2011) studied the seasonal variation in PAI for 10 homogeneous oak stands in neighbouring Northern Belgium (Flanders) using hemispherical photography. They observed the start of leaf unfolding between April 18 and April 24, 2008 (DOY 109-115). This is 16 to 22 days later than the TLS derived SOS we observed in location C and D (i.e. the locations with only 5% of birch). The comparison of our TLS derived SOS with the predictions from the phenological model (figure 3.4) also showed a disagreement, with TLS estimates starting 22 to 27 days earlier. A possible explanation for these disagreements may be the differences in winter and spring temperatures between different years or with the yearly median. Figure 3.6 shows the yearly historical GDD and number

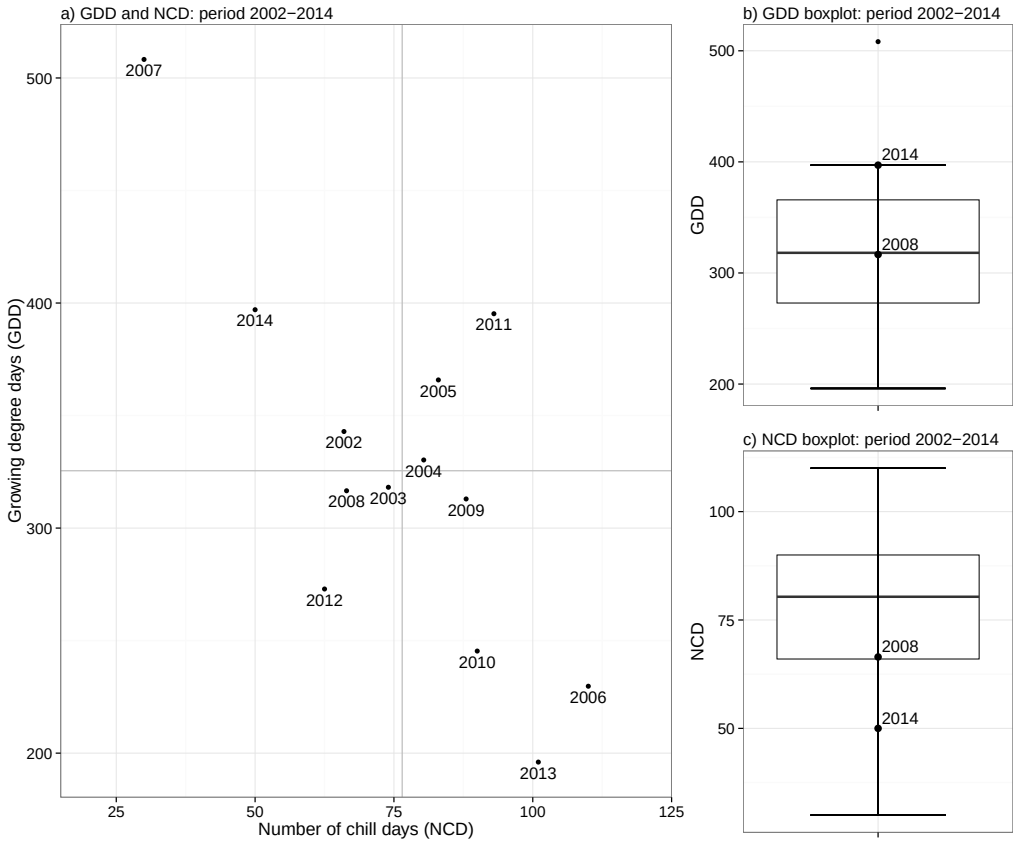


**Figure 3.6:** Growing degree days (GDD) and number of chill days (NCD) for the period 2002-2014. GDD was calculated according to equation 3.4 until DOY 126. NCD was calculated from November 1 in the previous calendar year until DOY 126. DOY 126 was the latest date for the start of season according to equation 3.5 during the period 2002-2014 (year 2012). We corrected the yearly GDD and NCD for leap years. Panel (a) shows the yearly NCD and GDD with the grey lines representing the yearly average. Panel (b) shows the GDD box plot and panel (c) shows the NCD box plot, with the whiskers at 1.5 times the interquartile box plot range.

of chill days (NCD) for the period 2002-2014. Year 2014 had the second highest GDD (397) and NCD (50) and the box plots in figure 3.6 indicate that the 2014 GDD and NCD values fall outside the interquartile range. Year 2014 had 79 more GDD and 30 days less chill days compared to the yearly median. Bequet et al. (2011) studied spring phenology in 2008, which had 16 more chilling days and 80 less GDD compared to 2014. Both GDD and NCD for 2008 fall within the interquartile range of the historical data (period 2002-2014), whereas the values for 2014 suggest a warmer winter and spring compared to these historical data. Fu et al. (2012) used controlled experiments to study the effect of winter and spring warming on phenology. They concluded that birch and oak trees that were exposed to both winter and spring warming would start leaf unfolding earlier when compared to no winter and spring warming. The processes that control spring phenology

are complex, but it is generally accepted that spring warming accelerates bud development (Chmielewski & Rotzer, 2001). Chilling is important and warmer temperatures in winter might delay endodormancy release (Dantec et al., 2014; Murray et al., 1989). However, in trees with lower chilling requirements (e.g. birch and oak), the required chilling may be met even under warming conditions (Dantec et al., 2014; Fu et al., 2012) and warmer winters might therefore advance the start of season too.

Terrestrial LiDAR provides information about the 3D distribution of canopy constituents and enabled us to look at the spring phenology in different horizontal canopy layers. The sigmoidal models were a good fit for the upper canopy and intermediate layer, but local agreement for the understorey layer was poor (figure 3.5). Assuming the PAI uncertainty is constant with height, this can be partly explained by higher relative error compared to the intermediate and upper canopy layer. Absolute PAI values for the understorey are low and range from approximately 0.02 in leaf off conditions to approximately 0.16. The low signal in the understorey layer was a combination of the sparse vegetation in this layer and the lower zenith angle limit of 70° for the vertical plant profiles. The vertical plant profile approach described in section 3.3.1 requires the laser pulse to exit the canopy, which might not always be the case for larger zenith angles, where the path length through the canopy may be greater than the maximum range of the TLS instrument. Future work will investigate modelling of vertical plant profiles to ground level using zenith angles greater than 70 degrees. This will broaden the applications for vertical plant profiles too, for example for better characterisation of ground and understorey fuel loads for fire management.

Our study area was essentially a single-layered forest because the understorey was sparse, but differences in phenology were observed between the different layers (table 3.4). TLS derived vertical profiles have the potential to be an excellent tool to study $P_{gap}$ and PAI dynamics in multi-layered forests. Gond et al. (1999) studied the seasonal variation of PAI in a multi-layered forest using an LAI-2000 instrument, which was used at ground level and mounted on an extendable pole to differentiate between understorey and overstorey canopy. TLS offers a more practical solution since all measurements can be taken from the same location and the 3D data is used to differentiate between horizontal layers. The approach presented in this paper can be directly transferred to the collection of similar TLS time series data in multi-layered forests. Such data will give us more insight into how understorey species take advantage of high-light periods in spring before the development of the upper canopy (Richardson & O'Keefe, 2009).

Recent developments in autonomous ground-based LiDAR instruments will enable us to increase the temporal resolution of 3D data. The VEGNET IML scans the hinge angle region and was used to create vertical plant profiles at a daily frequency to monitor phenological changes in fall (Portillo-Quintero et al., 2014). We have not addressed the issue of spatial variance in this work, but it is important for upscaling variables inferred

from a single sample location to plot level information and is subject of future work. Differences in scanner height between single sample locations and the proximity of individual branches may introduce large variations in $P_{gap}$ at the larger zenith angles, and thereby increase the variation in PAVD and PAI. The vertical plant profiles in this work do not separate between woody and non-woody canopy constituents. Such separation of vertical plant profiles will enable us to quantify temporal changes in leaf and non-leaf components. The recent development of two dual wavelength research TLS instruments (SALCA, Salford Advanced Laser Canopy Analyser; DWEL, Dual-Wavelength Echidna Lidar) are designed to facilitate this separation (Danson et al., 2014; Gaulton et al., 2013; Douglas et al., 2012).

## 3.6 Conclusion

This work provides insight in the stability of terrestrial LiDAR measurements in the context of repeatable measurements, which is important to quantify changes in forest structure. We explore the potential of TLS for monitoring changes in phenology, which may reduce uncertainty in reference data used for calibration and validation of large scale remote sensing products. Sigmoidal models show a good fit for TLS PAI time series of the total integrated canopy (CV(RMSE) $< 2.4\%$ and CCC $> 0.99$) and specific horizontal layers. The sigmoidal fit to the understorey data is a good approximation of the overall shape, but showed local disagreement caused by the relative lower signal to noise ratio. The start of season is derived based on the total canopy integrated PAI time series and compared to phenological models that include heat and chill requirements. The SOS inferred from the TLS data occurs 22 to 27 days earlier compared to the prediction based on meteorological data, which is likely caused by winter and spring warming. Vertical plant profiles are inferred from 3D TLS data, which not only enables us to look at structural changes of the vertically integrated canopy, but also at specific horizontal layers. TLS therefore provides a tool to study seasonal dynamics as a function of time, as well as a function of canopy height. This will be of importance for monitoring multi-layered forests, where the understorey species will generally have an earlier start in the growing season.

## Acknowledgements

We thank Alvaro Lau Sarmiento and Brodie McIntosh for their assistance with fieldwork and Bert Heusinkveld for providing the meteorological data.

# Chapter 4

# Estimating AGB using terrestrial LiDAR

This chapter is based on:

Calders, K., Newnham, G., Burt, A., Murphy, S., Raumonen, P., Herold, M., Culvenor, D., Avitabile, V., Disney, M., Armston, J. and Kaasalainen, M., 2014. Nondestructive estimates of above-ground biomass using terrestrial laser scanning. *Methods in Ecology and Evolution*, DOI: 10.1111/2041-210X.12301.

***Abstract:***

**1.** Allometric equations are currently used to estimate above-ground biomass (AGB) based on the indirect relationship with tree parameters. Terrestrial laser scanning (TLS) can measure the canopy structure in 3D with high detail. In this study we develop an approach to estimate AGB from TLS data, which does not need any prior information about allometry. We compare these estimates against destructively harvested AGB estimates and AGB derived from allometric equations. We also evaluate tree parameters, diameter at breast height (DBH) and tree height, estimated from traditional field inventory and TLS data.

**2.** Tree height, DBH and AGB data are collected through traditional forest inventory, TLS and destructive sampling of 65 trees in a native Eucalypt Open Forest in Victoria, Australia. Single trees are extracted from the TLS data and quantitative structure models are used to estimate the tree volume directly from the point cloud data. AGB is inferred from these volumes and basic density information, and is then compared with estimates derived from allometric equations and destructive sampling.

**3.** AGB estimates derived from TLS show a high agreement with the reference values from destructive sampling, with a concordance correlation coefficient (CCC) of 0.98. The agreement between AGB estimates from allometric equations and the reference is lower (CCC = 0.68 to 0.78). Our TLS approach shows a total AGB overestimation of 9.68% compared to an underestimation of 36.57% to 29.85% for the allometric equations.

**4.** The error for AGB estimates using allometric equations increases exponentially with increasing DBH, whereas the error for AGB estimates from TLS is not dependent on DBH (figure 4.10). The TLS method does not rely on indirect relationships with tree parameters or calibration data and shows better agreement with the reference data compared to estimates from allometric equations. Using 3D data also enables us to look at the height distributions of AGB and we demonstrate that 80% of the AGB at plot level is located in the lower 60% of the trees for a Eucalypt Open Forest. This method can be applied in many forest types and can assist in the calibration and validation of broad scale biomass maps.

## 4.1 Introduction

Above-ground biomass (AGB) is an important indicator for forest productivity, carbon storage and sequestration of forests (Bi et al., 2004). However, the global distribution of carbon sources and sinks is uncertain (Houghton et al., 2009) and carbon emissions are poorly known on local, national and global scales (Hill et al., 2013). Data retrieved through remote sensing methods can be a useful tool to monitor AGB over large areas (Avitabile et al., 2012), with a currently increasing interest in forest carbon stock changes (De Sy et al., 2012). Accurate ground reference measurements are needed for the calibration and validation of these global satellite derived AGB datasets. Two recently published maps of carbon stocks in tropical regions across different continents (Saatchi et al., 2011; Baccini et al., 2012) used similar input data layers but showed substantial differences in mapped AGB , especially in areas with little field data (Mitchard et al., 2013). These two pantropical AGB maps also show very different spatial patterns compared to field plots distributed across the region (Mitchard et al., 2014). Improving the field techniques is key to reducing uncertainty in global biomass mapping and previous work suggests more emphasis is needed on real plot-level forest AGB measurement instead of estimating AGB from traditional allometric equations (Asner et al., 2013).

Current field methods to estimate AGB of forests are generally based on indirect relationships with tree structural parameters, such as diameter at breast height (DBH) and tree height (Chave et al., 2014; Bi et al., 2004). This allometric approach can be effective when applied within the productivity and species range of the calibration data, but may lead to large uncertainties in broad scale biomass mapping. This is particularly true for large trees which contain most of the biomass (and thus carbon) but have rarely been harvested and measured (Stephenson et al., 2014). Calibration data to support allometric biomass models requires direct estimates of AGB that involve destructive sampling of trees. This is often expensive and impractical and can therefore only be conducted on a limited basis. Terrestrial laser scanning (TLS), also called terrestrial LiDAR (light detection and ranging), is an active remote sensing technique that can accurately measure distances by transmitting laser pulses and analysing the returned energy as a function of time. TLS therefore can serve as an excellent tool to assess forest structure and the three-dimensional distribution of plant constituents (Calders et al., 2014). TLS allows for measuring forest structure with high detail and accuracy and has the potential to reduce uncertainties in inferring AGB since it enables direct estimates of complete tree volume. Dassot et al. (2012) demonstrated the potential of TLS for assessing wood volume in leaf-off conditions and used simple geometric fitting to model the woody structure up to branches of 7 cm. Hosoi et al. (2013) used a voxel-based model to estimate the woody volume. These previous studies focused on woody components only, required a substantial amount of manual input or were restricted in sensitivity analysis.

In this paper we suggest an approach to estimate total AGB based on detailed non-

destructive sampling with terrestrial LiDAR. We validate the derived AGB estimates against destructively harvested AGB in native Eucalypt Open Forest plots in Australia. This nondestructive approach has important implications for large area sampling of AGB as it facilitates calibration and validation of satellite derived biophysical datasets. The main objectives of this paper are:

1. The derivation of AGB through TLS derived volume estimates and basic density information;
2. The validation of TLS derived AGB estimates with destructively sampled AGB; and
3. The comparison of TLS derived AGB estimates with AGB derived from allometric biomass models.

We also compare traditional forest inventory measures such as DBH and tree height from TLS data and field data. Our TLS-driven approach supports the need for an accurate nondestructive method to assess AGB. A comparison of AGB derived through TLS and allometric models with the harvested AGB gives some insight into the potential and accuracy of TLS for rapid biomass assessments at the plot level, and how this may be used in support of broad scale biomass mapping.

## 4.2 Study area and data collection

### 4.2.1 Study area

This study was undertaken in native Eucalypt Open Forest (dry sclerophyll Box-Ironbark forest) in Victoria, Australia. Two plots (RUSH06 and RUSH07) with a 40 m radius were established in Rushworth forest and partially harvested in May 2012 to acquire accurate estimates of AGB. The main tree species in these plots were *Eucalyptus leucoxylon*, *E. microcarpa* and *E. tricarpa*. Plots RUSH06 and RUSH07 had a stem density of 347 and 317 stems/ha and a basal area of 13.0 and 13.2 $m^2$/ha respectively.

### 4.2.2 Forest inventory and destructive sampling

Traditional field inventory was carried out pre-harvest to collect DBH, tree height and stem maps for both plots. Each stem of a multi stem tree was treated as an individual tree in the forest inventory and analysis if the stems split below 1.3 m. DBH was measured over bark at 1.3 m using a diameter tape (precision to the nearest mm). Tree height was measured using a Laser Tech Impulse (Laser Technology Inc.), which has a precision to the nearest 0.1 m. Detailed measurements of tree height (with a tape measure) and fresh weight (FW) were collected in the field for each harvested tree. Fresh weight was measured using a Wedderburn WS600 digital crane scale (W.W. Wedderburn Pty Limited).

**Table 4.1:** Summary of parameters a and b to describe the dry weight (DW) to fresh weight (FW) ratio as a function of DBH: DW:FW = a + b*DBH.

| Species | # sample trees | a | b | $R^2$ of fit |
|---|---|---|---|---|
| *E. leucoxylon* | 8 | 0.4869 | 0.004088 | 0.91 |
| *E. microcarpa* | 13 | 0.6366 | 0.001785 | 0.74 |
| *E. tricarpa* | 7 | 0.6102 | 0.001913 | 0.94 |

Most fresh weight crane lifts were <500 kg at an accuracy of 0.2 kg, with very few lifts approaching 1000 kg at an accuracy of 0.5 kg. Basic density (dry weight overbark per unit green volume) and moisture content for each species were derived from a limited number of samples across a range of DBH (11 - 62 cm). Discs were taken every 3 m (from DBH) up the tree for a single sample tree to a minimum diameter of 5 cm and the total fresh and dry weight (DW) of these discs (including bark) was used to generate a weighted average DW:FW ratio. The discs were all dried at 70°C to constant weight and whole discs were weighed, including bark. The moisture content ratios are lower for larger DBH and higher for smaller diameters, reflecting the proportion of sapwood. The DW:FW ratios are described as function of DBH for each tree species (DW:FW = a + b*DBH; table 4.1). The reference dry weight of single trees, i.e. AGB, was derived from the measured fresh weights in combination with the inverse DW:FW ratios. Basic densities for the harvested species are 625.5 kg/m$^3$ for *E. tricarpa*, 665.1 kg/m$^3$ for *E. leucoxylon* and 759.4 kg/m$^3$ for *E. microcarpa*. These basic densities were derived from full discs including bark at a height of 1.3 m.

### 4.2.3 Terrestrial LiDAR data acquisition

TLS data were acquired with a RIEGL VZ-400 terrestrial laser scanner (RIEGL Laser Measurement Systems GmbH). The beam divergence is nominally 0.35 mrad and the instrument operates in the infrared (wavelength 1550 nm) with a range up to 350 m. The instrument also collects information about the yaw (through an internal compass) and the pitch and roll (through inclination sensors). This scanner allows fast data acquisition and records multiple return LiDAR data (up to four returns per emitted pulse). The advantage of multiple returns over single returns has been discussed by Calders et al. (2014). They concluded that multiple return instruments will lead to an improved sampling at greater canopy heights. The scanner settings were the same across all scans and are summarised in table 4.2. We used five scan locations per plot in a systematic sampling design with one centre scan location and a scan location at 40 m from the centre in each cardinal direction. The RIEGL VZ-400 has a zenith range of 30 to 130 degrees. Therefore an additional scan was acquired at each scan location with the instrument tilted at 90 degrees from the vertical to sample a full hemisphere. Reflecting targets were distributed throughout the

**Table 4.2:** Riegl VZ-400 scanner settings for data acquisition.

| | |
|---|---|
| Beam divergence | 0.35 mrad |
| Pulse repetition rate | 300 kHz |
| Minimum range | 1.5 m |
| Azimuth range | 0° - 360° (0.06° angular sampling) |
| Zenith range | 30° - 130° (0.06° angular sampling) |
| Acquisition time | 1 minute 23 seconds |

plot and were used to register the five scan locations using the RiSCAN PRO software (provided by RIEGL). The average standard deviation of the registered point clouds was 0.0129 m with values for individual scans ranging from 0.0062 m to 0.0226 m. Figure 4.1 shows the terrestrial LiDAR data pre- and post-harvest for RUSH07, visualised from a virtual point above the forest.

## 4.3 Methods

### 4.3.1 Terrestrial LiDAR analysis

Tree height, DBH and AGB were derived from the TLS data following a two step approach: i) extracting single trees from the registered pre-harvest TLS point cloud; and ii) deriving parameters for an extracted single tree.

#### Extracting single trees

A C++ library based on the open-source Point Cloud Library (Rusu & Cousins, 2011) was used to develop a semi-automated extraction of individual trees from the global point clouds. This was achieved in four steps: i) identification of individual stems through segmentation of the ground plane and return reflectance filtering; ii) cylinder fitting to these stems and application of a series of pass through filters with respect to the unfiltered point cloud to extract the individual trees; iii) sequential identification of point clusters defined by point density in height slices along the length of the tree to remove unrelated vegetation and noise from these clouds; and iv) visual inspection against the whole point cloud and, if needed, manual removal of unrelated vegetation from neighbouring trees.

In the first step, only LiDAR data within the 40 m plot radius and reflectance values above -4 dB were used. Reflectance is defined as range-corrected intensity and the majority of the LiDAR returns generally ranges between -20 dB (low return energy) to 0 dB (high return energy). The unfiltered point cloud in step two and three had a 50 m radius. This allowed us to capture the full crown extent of trees whose stem is within the boundaries

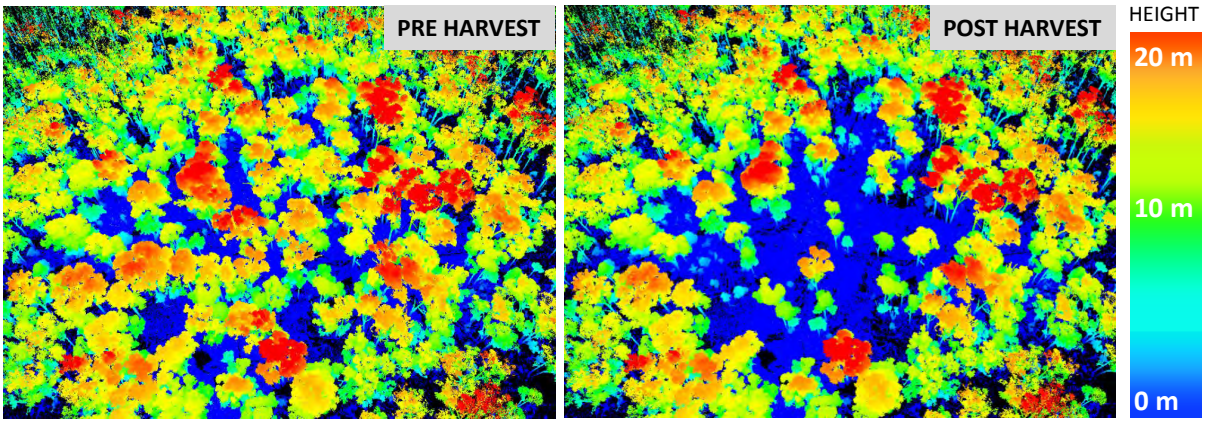


**Figure 4.1:** Pre and post harvest terrestrial LiDAR data for RUSH07 plot.

of the plot, but have their crown partially outside the plot boundaries. The slices in step three are 1 m high and each slice increases 300% in x and y coordinate compared to the slice below. The visual inspection in step four is similar to the final step in single tree extraction from a LiDAR point cloud in Hopkinson et al. (2004).

### Tree height and DBH

Tree height was calculated as the difference between the height of the highest and lowest LiDAR point of a single tree point cloud. The DBH was calculated on a 0.06 m thick cross section between 1.27 and 1.33 m above the lowest point (Tansey et al., 2009). We use a least squares circle fitting algorithm to account for potential occlusion in the LiDAR data. Tansey et al. (2009) compared least squares circle fitting, least squares cylinder fitting and circular Hough transformation for estimating DBH and found that least squares circle fitting was most accurate.

### AGB from quantitative structure models

Tree volume was directly inferred from the TLS data through quantitative structure models (QSMs). AGB is derived from these volume estimates and basic density. The QSMs in this paper are reconstructed with a modified version of the method presented in Raumonen et al. (2013). The original method was validated previously using detailed 3D tree models, where tree structure was known. Results showed that, with some constraints, original length and volume could be reconstructed with a relative error of less than 2% (Disney et al., 2012). Burt et al. (2013) applied the same approach to TLS data from three different forest types in Queensland, Australia. Based on TLS simulation of the reconstructed tree model, they found that total volume could be recreated to within a 10.8% underestimate. The accuracy to which single scans could be globally registered was

identified as the greatest constraint in the method.

The reconstruction method assumes a single tree point cloud and has two main steps. First, the point cloud is segmented into stem and branches, and secondly, the surface and volume of the segments are reconstructed with geometric primitives, in this case with cylinders. The method uses a cover set approach, where the point cloud is partitioned into small subsets, which correspond to small connected patches in the tree surface. The cover sets or patches can be thought of as small building bricks, which can be used to grow the tree from its base upwards and into the branches. The size of the patches is important: after an optimum size is reached, the larger the patches are, the less detail that can be modelled.

The first main step of segmenting the point cloud into branches can be divided into multiple sub-steps and the segmentation is done twice. The first segmentation uses large patches and its purpose is to use the segmentation for information about the local size of the branches based on the branching order, height, and position in the branch. This information is then used for a second iteration where the patch size is smaller and varies: the size decreases linearly along the branch from the base to the tip and the size at the branch base decreases with increasing height and branching order (figure 4.2).

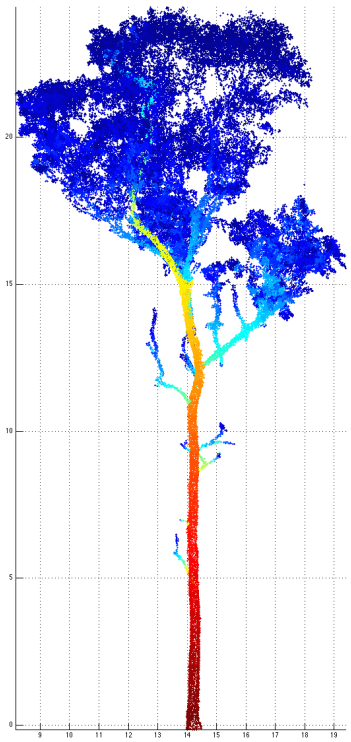


**Figure 4.2:** Example of patch size variation according to the first segmentation for a *E. leucoxylon*. Dark blue denotes areas with half the patch size of dark red areas at the base of the tree.

After the cover generation, we next model the base of the stem at the bottom part of the point cloud. We approximate the stem by expanding the base upwards using the neighbour relation of the patches. The approximated stem now contains most of the stem patches and some patches from first order branches. We determine the connected components of the other patches near the approximate stem and connect them to the stem by modifying the neighbour relation. This ensures that small occlusions do not disconnect first order branches from the stem. Finally we expand the stem into tree crown as much as possible and determine all the connected components of the other patches. The components are connected to the closest parts of the tree or other components. This process of determining separate components and connecting them is continued until the tree is one connected component.

Next the patches are segmented into stem and branches using the algorithm presented in Raumonen et al. (2013), with some additional correctional steps:

1. The small child segments, whose distance from the parent segment is about the same as the approximate radii of the parent segment, are removed as ambiguous and insignificant;

2. The initial segments are corrected so that they are reaching the furthest tip of their child segments. The stem segment is corrected to reach the highest tip of all the segments. The resulting segmentation is more robust, has lower maximum branching order, and in general the segments correspond better with the real branches; and

3. The segments are expanded into their parent segment and the whole expansion is removed from the parent and the child. This diminishes the size and occurrence of small parts of the child segments in the parent, which can make the fitted cylinders too large.

After the second segmentation based on small patches, the second main step is to reconstruct the surface and volume of the segments. This is accomplished by fitting cylinders, in a least squares sense, into short sub-regions of the segments. The length of the sub-regions is approximately controlled by the input parameter $l$ that defines the relative length of the cylinders, i.e. the ratio of the length and radius. After the cylinders are fitted to a segment, the fitted radii is checked in two ways to eliminate unrealistic cylinders that otherwise would be fitted in some instances. First the radii that exceed the radius of the parent segment at the branching point are set to the value of the parent, and the radii below 2.5 mm are set to 2.5 mm. The radius along the segment is controlled by a parabola shaped taper, which makes the radii decrease towards the tip (figure 4.3). The parabola is fitted to the taper data of a few cross sections of the branch and it gives the maximum local radii along the branch. The minimum radius is 75% of the maximum. For the stem we use a partially linear taper, with the radius at the end of the stem set to 2.5 mm (figure 4.3).

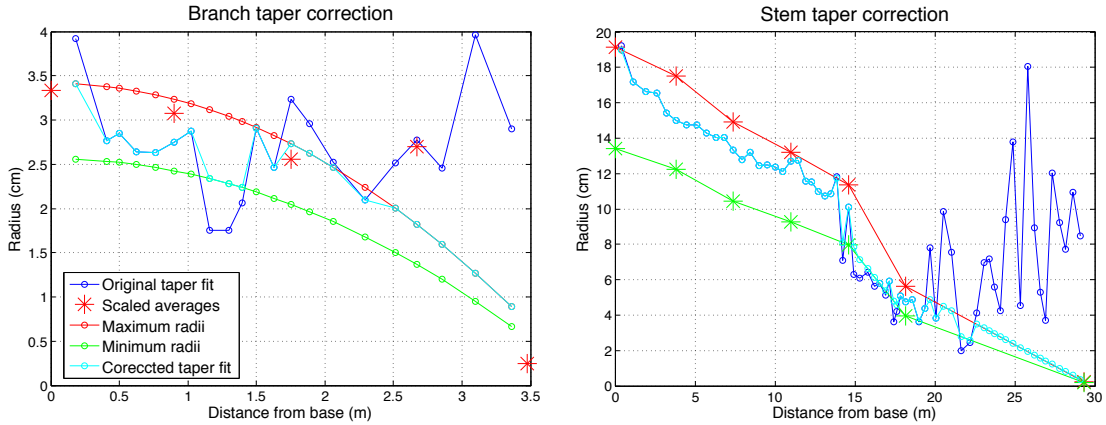


**Figure 4.3:** Radius control along branches and stem. Red stars are the scaled average radii at specific cross sections of the branch and scaled up by 5%. These are used for fitting the parabola (left) or for defining the partially linear red taper curve (right), which defines the maximum local radii.

The method has two important input parameters, $d$ and $l$, which define the patch size in the second cover and the relative cylinder length. Given that the cover generation is random, the final QSMs are always a little different, even if using exactly the same input parameters. To assess the robustness of the reconstruction method and variability between the results, we produced 10 models for each case and calculated the mean and standard deviation from these 10 models. We tested higher number of iterations (20, 50 and 100 runs) for a selected number of trees, but mean (Student's t-test) and standard deviations (Levene's test) did not significantly differ. The method is implemented in MATLAB and the average model completion time over our total 650 runs was 102 seconds per run when using a Windows 7 64-bit operating system (3.07 GHz, 24 GB memory).

### 4.3.2 Allometric biomass models

Allometric equations for estimating above-ground biomass for the harvested Eucalyptus species are described in Paul et al. (2013). The equations use a power function, which has a linear equivalent form:

$$ln(AGB) = a + b \times ln(DBH) + e \tag{4.1}$$

Values for parameters $a$ and $b$ are specified in table 4.3, as well as the correction factor. This factor is a bias correction for the AGB estimates following back-transforming the logarithm as described by Snowdon (1991). The derived AGB is multiplied by the factor to correct for the bias.

**Table 4.3:** Summary of parameters $a$, $b$ and $CF$ in allometric equations according to Paul et al. (2013). $N$ gives the number of individual trees and maximum DBH indicates the upper limit of the calibration data used to develop the allometric equations. $EF$ is the model efficiency index to assess the accuracy of overall fit with the calibration data and ranges from 0 to 1 (perfect fit).

| Species | $N$ | Max. DBH [cm] | $a$ | $b$ | $CF$ | $EF$ |
|---|---|---|---|---|---|---|
| *E. leucoxylon* | 28 | 25 | -1.37 | 2.07 | 1.04 | 0.98 |
| *E. microcarpa* | 30 | 110 | -1.92 | 2.36 | 1.17 | 0.98 |
| *E. tricarpa* | 54 | 60 | -2.39 | 2.40 | 1.10 | 0.95 |
| Generic *Eucalyptus* tree | 2640 | 100 | -1.71 | 2.21 | 1.29 | 0.93 |

### 4.3.3 Measurement comparison

We used linear regression to compare different methods for deriving DBH and tree height. Both tree height and AGB have reference measurements through destructive harvesting. We therefore calculated their root mean squared error (RMSE) with respect to the 1:1 line to evaluate the deviation from the reference data. AGB was estimated through allometric equations and TLS. We compared these two different methods against the reference data by calculating the coefficient of variation of the RMSE, CV(RMSE), and the concordance correlation coefficient, CCC. CV(RMSE) is defined as the RMSE normalised to the mean of the reference values. Unlike the RMSE, CV(RMSE) is unitless and this allows values to be easily compared to one another. CCC computes the agreement on a continuous measure obtained by two methods (Lin, 1989) and ranges between 1 (perfect concordance) and -1 (perfect discordance).

## 4.4 Results

A total of 75 trees were harvested (table 4.4), 65 of which were included in the analysis (25 *E. leucoxylon*, 21 *E. microcarpa* and 19 *E. tricarpa*). The inventory measures of the remaining ten harvested trees could not be linked with the extracted trees from the TLS data. This mostly concerned multi stem trees with similar DBH for the different individual stems. Four more trees were missing reference tree height data and were excluded from the height analysis (see table 4.4). AGB was destructively measured in the field and used as a reference to compare against AGB derived from TLS data and allometric equations. Furthermore, we compared tree height and DBH measurements from traditional field measurements, terrestrial LiDAR and destructive sampling (reference).

**Table 4.4:** Rushworth felled and sampled trees, and trees used in analysis.

| Tree count | RUSH06 | RUSH07 | Total |
|---|---|---|---|
| Felled and Sampled Trees (FST) | 36 | 39 | 75 |
| FST in AGB analysis | 34 | 31 | 65 |
| FST in DBH analysis | 34 | 31 | 65 |
| FST in height analysis | 33 | 28 | 61 |

### 4.4.1 DBH and tree height

The comparison of field measured DBH against TLS derived DBH is shown in figure 4.4. The linear regression shows an RMSE of 0.02 m and a slope of 0.98. Figure 4.5 illustrates the different scenarios for inferring DBH from TLS data through circle fitting. The left panel shows a circle fit through data with no occlusion, whereas the middle panel illustrates how circle fitting overcomes occlusion in the TLS data. For one tree in our study sites (double leader), a circle shows not to be the most optimal fit (Figure 4.5, right panel).

The destructively measured tree height is compared against the field measured tree height and the TLS derived tree height in figure 4.6. Both methods show a good linear fit with

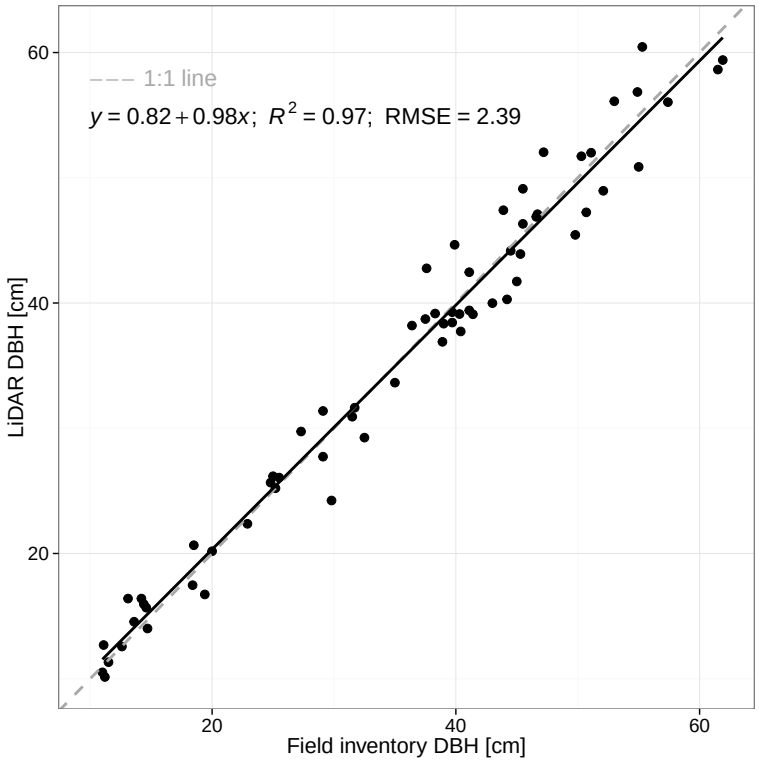


**Figure 4.4:** Comparison of TLS derived DBH with field measured DBH values.

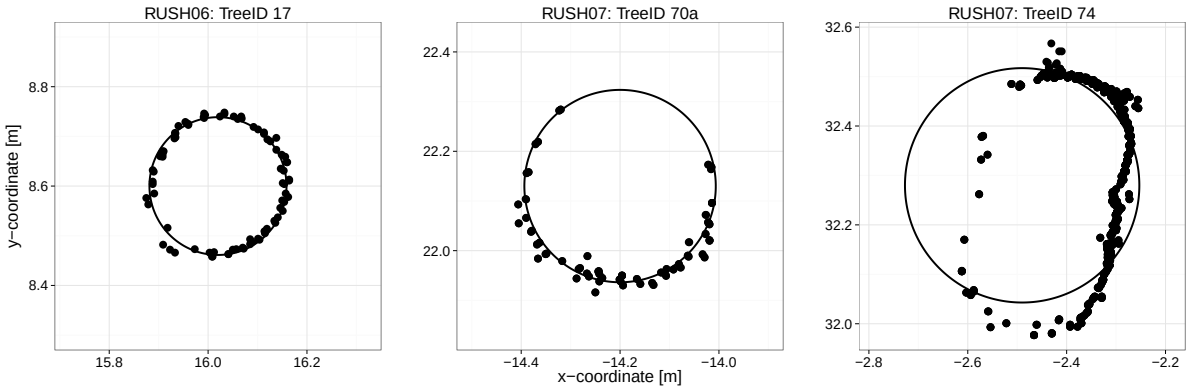


**Figure 4.5:** Examples of TLS derived DBH through circle fitting on the 1.27 - 1.33 m cross section above the lowest LiDAR point. (Left) No occlusion in the data; (middle) Partial occlusion in the data; (right) Circle not the optimal fit.

the reference tree height data, but tree heights measured using traditional methods were underestimated in trees up to approximately 16 m tall, and overestimated in trees taller than 16 m. The linear fit of the TLS derived heights is close to the 1:1 line with a slope

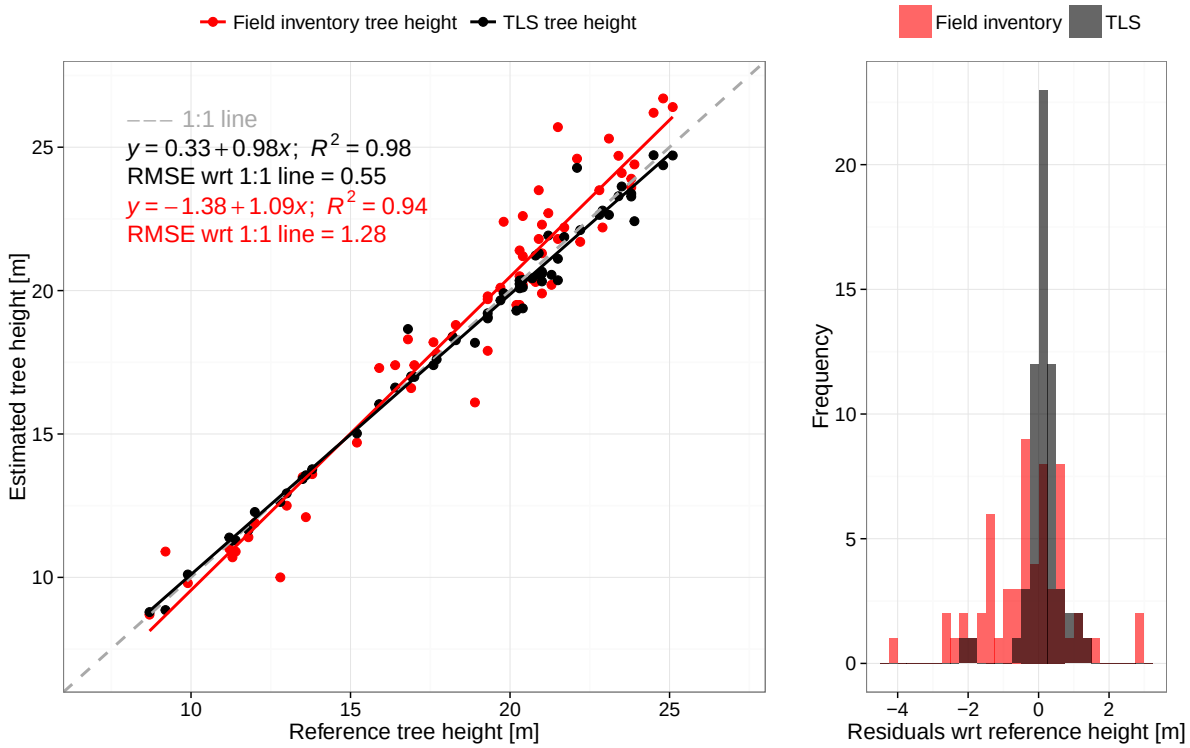


**Figure 4.6:** Comparison of destructively measured reference tree height with a) TLS derived tree height and b) field measured tree height. (Left) linear regression; (right) residuals = reference tree height - estimated tree height.

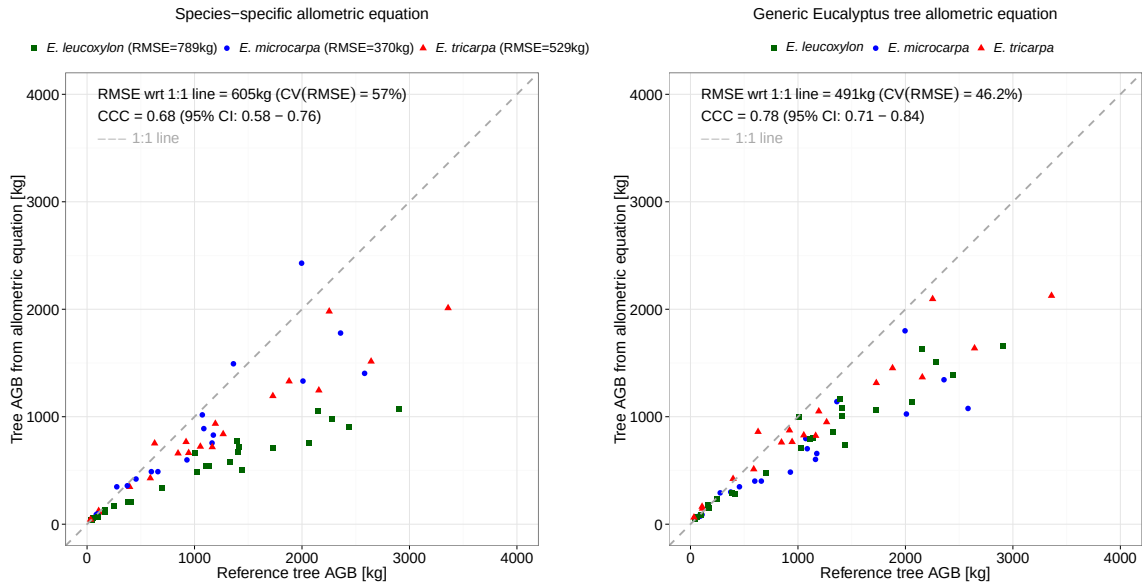


**Figure 4.7:** Comparison of destructively measured reference tree AGB with AGB derived from allometric equations. (Left) AGB from species-specific allometric equations; (right) AGB from the Generic Eucalyptus tree allometric equation.

of 0.98. Residuals for both height methods are calculated with respect to the reference heights and are shown in the right panel of figure 4.6. The RMSE with respect to the 1:1 line is 0.55 m for the TLS derived heights and 1.28 m for the field inventory heights.

### 4.4.2 Above-ground biomass

Above-ground biomass estimates from allometric equations are compared against the harvested reference values in figure 4.7. AGB derived from allometric equations generally underestimates the reference AGB. The overall CV(RMSE) for the species-specific equations is 57% and the CV(RMSE) for the generic *Eucalyptus* equation is 46.2%. The agreement between the allometric equation AGB and the reference, expressed by the concordance correlation coefficient (CCC), is lowest for the species-specific equations (0.68) and is as high as 0.78 for the generic *Eucalyptus* equation.

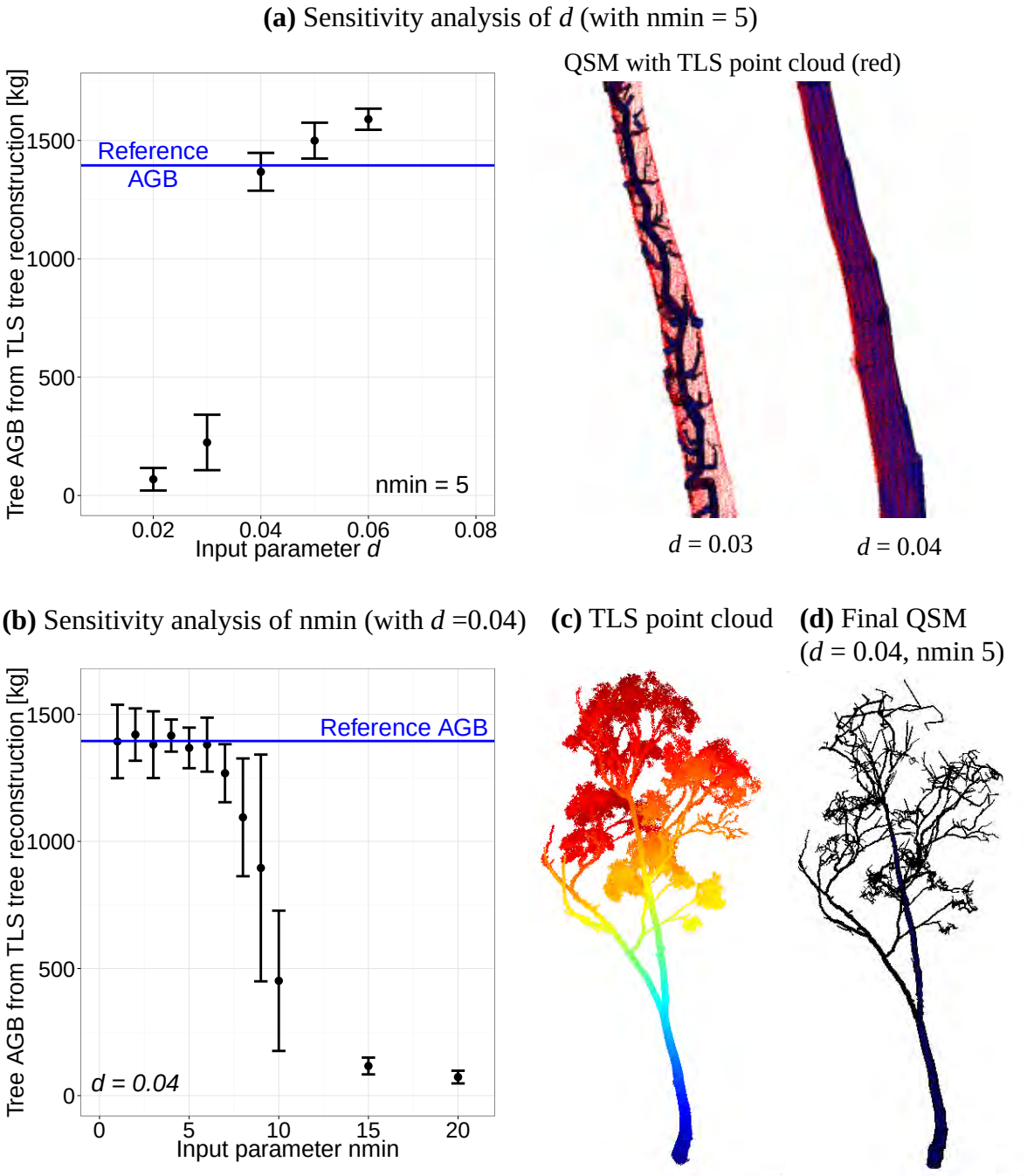


**Figure 4.8:** Sensitivity analysis, TLS point cloud and final QSM for a *E. leucoxylon* (RUSH07: TreeID 4). a) sensitivity analysis of *d*, which defines the patch size, with examples of the stem for values 0.03 and 0.04; b) sensitivity analysis of nmin, the minimum number of points within a single patch; c) TLS point cloud; d) final QSM model.

Tree volume is directly inferred from the TLS data through quantitative structure models (QSMs), and AGB is inferred from these volume estimates and basic density. The input parameters for the QSM method were visually evaluated and, the relative cylinder length, $l$, of five was selected to best represent the general tree structure. Parameter $d$ defines the patch size of second cover generation and we used the smallest $d$ that models the stem well (figure 4.8a) . The input parameter that determines the neighbour relations was fixed to $d + 0.005$ m. The last input parameter that influences the volume reconstruction controls the minimum threshold of LiDAR points within a single patch for inclusion in the reconstruction. This parameter, *nmin*, is generally robust (figure 4.8b) up to a certain threshold. Values larger than that threshold will filter out parts of the tree (Calders et al., 2013b). Figure 4.8c-d shows an example of the TLS point cloud and the corresponding final QSMs for a *E. leucoxylon*.

Figure 4.9 compares the destructively measured AGB with the AGB inferred from TLS. The CV(RMSE) is lower than for the allometric equations (16.1%) and the agreement with the reference values is higher (CCC = 0.98). The absolute AGB deviation as a function of DBH for the different methods is shown in figure 4.10. This figure suggests an exponential

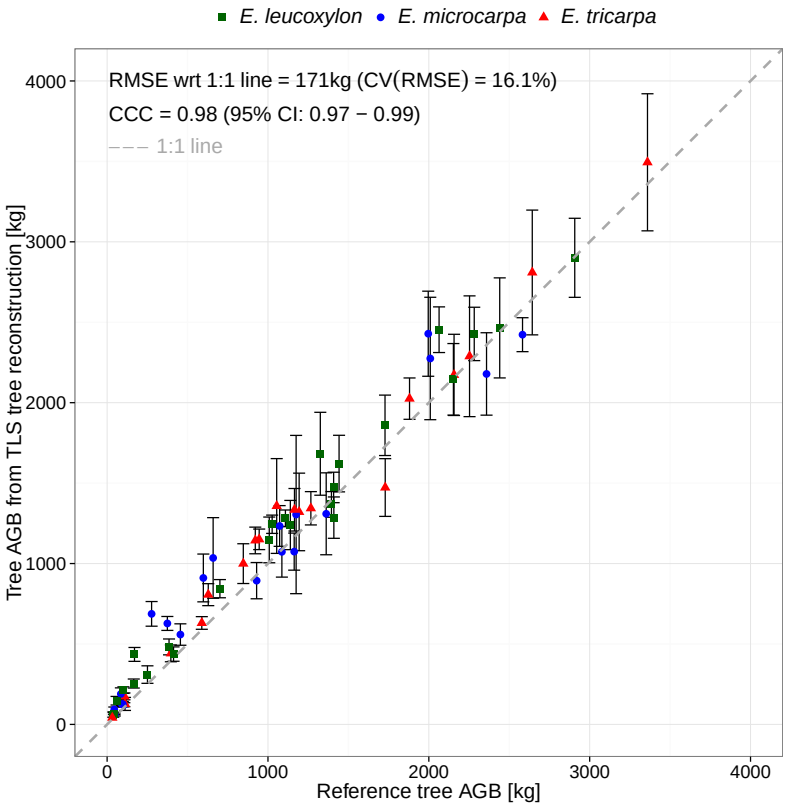


**Figure 4.9:** Tree AGB inferred from TLS volume estimates through tree reconstruction and basic density information. Error bars indicate the 95% confidence interval around the mean of 10 reconstructions.

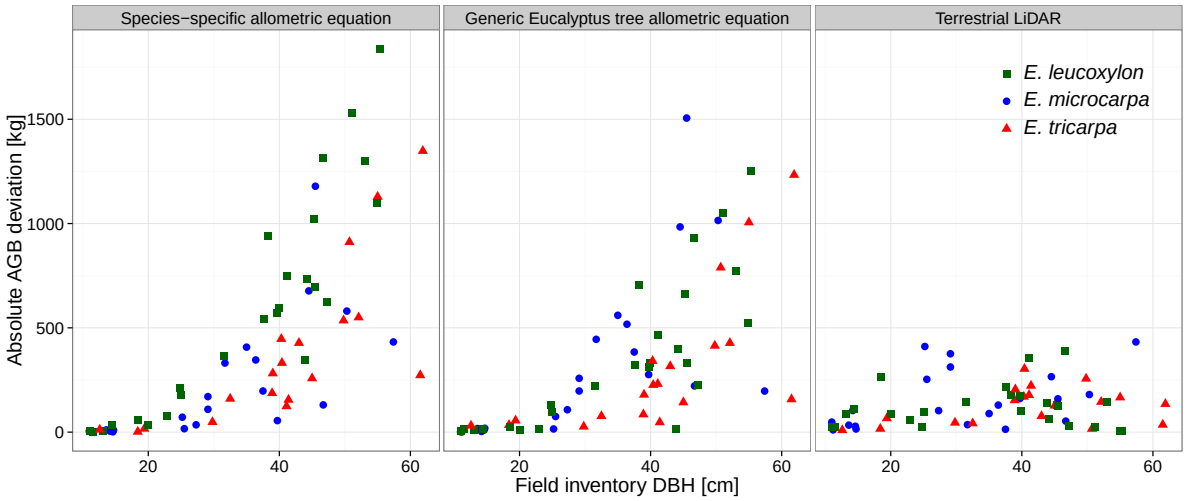


**Figure 4.10:** Comparison of absolute tree AGB deviation for TLS and allometry based methods.

increase in absolute deviation with increasing DBH for the allometric equations and a more stable deviation for the TLS derived values. The total AGB of the 65 trees ranges from 43.78 t (generic) to 48.42 t (species-specific) for the allometric equations and is 75.70 t for the TLS derived values. The destructive harvesting yielded 69.02 t, so there is an overall underestimation of 36.57% to 29.85% for the allometric biomass models and an overestimation of 9.68% for the total AGB derived from TLS.

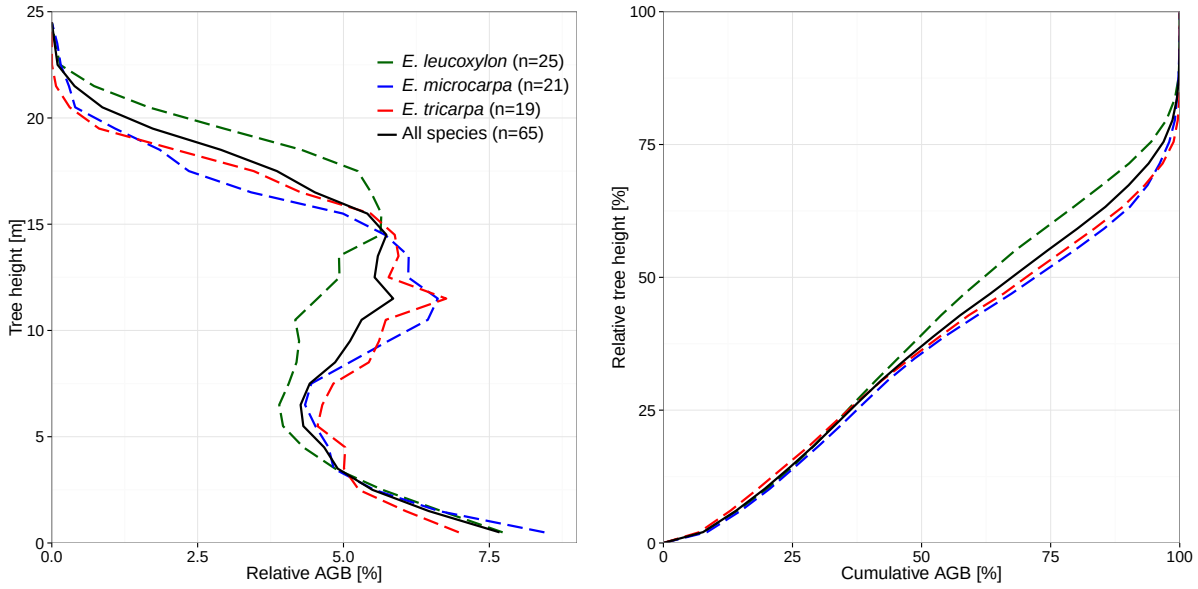


**Figure 4.11:** Tree height distribution of AGB derived from terrestrial LiDAR with height bins of 1 m.

TLS data provides information about AGB as a function of tree height and this is shown in figure 4.11. The tree height distributions of AGB are based on the AGB estimates in figure 4.9 with a vertical bin height of 1 m. These results show that more AGB is stored lower in the tree. Averaged over all *Eucalyptus* species, 50% of the AGB is approximately located in the lower 40% of the tree and 80% of the AGB is located in the lower 60% of the tree.

## 4.5 Discussion

Single trees were extracted from registered TLS point clouds with a semi-automated approach and no trees were missed in the extraction process. The comparison of TLS derived DBH measures with estimates from the field showed high accuracy and are consistent with previous work (Tansey et al., 2009; Hopkinson et al., 2004). Circle fitting works well when stems are partially occluded in the TLS data and the linear regression does not show bias.

It is not surprising that TLS derived height agrees better with the reference tree height than field measured height (figure 4.6). The RIEGL TLS system essentially fires millions of laser pulses to measure the canopy, whereas traditional field measurements are generally based on a single measurement of the tallest part of the tree. Picking the tallest part of the tree in Eucalypt Open Forest is often difficult from the ground given the large spreading of crowns and lack of apical dominance.

The model efficiency of the allometric equations in Paul et al. (2013) ranged from 0.93 to 0.98 (table 4.3), indicating a good fit with the calibration data of environmental plantings. Growing environments can be different for trees in native forests and the allometric equations underestimate the total AGB by 29.85% to 36.57%. Figure 4.10 suggests that the absolute error increases with increasing DBH of the tree. This is not unexpected because large trees have rarely been harvested and measured for the calibration data of the allometric equations (Stephenson et al., 2014). The allometric equations in this study only include DBH. Eucalyptus trees are not generally shade-tolerant, so diameter to height ratios can be quite variable. Stand height also reflects the degree of stand competition, particularly in the wetter eucalypt forests, and therefore has shown not to be significantly correlated to AGB. Consequently, DBH has been found to be the best predictor of AGB without much improvement from height as an additional parameter for these sites (Paul et al., 2013).

A circle may not always be the most optimal fit at 1.3 m, as is illustrated in figure 4.5 (right panel). The particular tree in this figure is a double leader, which does not split below 1.3 m. Similar problems may occur in tropical forests, where many trees have buttresses and do not follow the assumption of being circular at breast height and

instead should be measured above the height of the buttress (Cushman et al., 2014). Many allometric equations that are being used in tropical forests (Chave et al., 2014) also include tree height, as well as DBH. Figure 4.6 suggests that including tree height information from traditional field inventory in biomass regression models may prove to be problematic, depending on crown shape and apical dominance. Propagation of error in height estimates by using these allometric equations is likely to lead to reduced accuracy of AGB estimates (Kearsley et al., 2013). Terrestrial LiDAR has the potential to more accurately estimate tree height than traditional field methods, but further testing in densely forested environments is needed (Disney et al., 2014).

Our approach of tree volume modelling from terrestrial LiDAR data does not need prior assumptions about tree structure. This is important as our approach will not only be able to monitor natural gradual changes in biomass, but also abrupt changes caused by, for example, storm damage, harvesting, fire or disease. Kaasalainen et al. (2014) found that changes in tree and branching structure could be monitored within 10% with QSMs. The total AGB of the 65 trees is overestimated by 9.68% and the individual estimates in figure 4.9 also reflect a similar overestimation. Possible error sources that can cause overestimation can be related to the TLS data (registration error, occlusion, wind and noise) or quantitative structure model (QSM) reconstruction (segmentation error and geometric structure error due to cylinder versus real branch or leaf shape). The TLS AGB was derived from volume estimates and species-specific basic densities. We used basic densities that were derived from samples across a range of DBH. This may introduce some uncertainty in the conversion of volume to AGB for an individual tree, since basic density tends to be lower for smaller DBH and higher for larger DBH. Further reduction of these error sources is, along with objective parameter setting, an area of future work. The final step of the single trees extraction process, the removal of unrelated vegetation, required user interaction for about half of the trees and was caused by dominant and subdominant crown structures touching. This step was similar to Hopkinson et al. (2004), but further work should be carried out to fully automate the single tree extraction method. Boudon et al. (2014) provided an evaluation framework for the assessment of tree reconstruction that could assist with an automated objective parameter setting for the QSMs based on, for example, the sensitivity information in figure 4.8. A new QSM approach is currently being developed that combines both single tree extraction and QSM generation. These improvements will significantly speed up the processing of large plots and supports the need for robust and repeatable AGB estimates from TLS with limited user interaction.

This work provides a tool to assess AGB in a nondestructive and robust way. Furthermore, the three-dimensional nature of TLS data enables us to quantify AGB not only at tree or plot level, but also as a function of tree height, branch size or branch order. The vertical distribution of AGB is important for many applications, such as monitoring habitat heterogeneity and spatially explicit fuel load mapping. The latter is important to

predict fire behaviour and is essential for the development of 3D wildfire spread models (Skowronski et al., 2011).

## 4.6 Conclusion

We demonstrate not only that DBH can be extracted accurately from LiDAR data, but also that derived tree heights show better agreement with the reference height than traditional field height inventories. In this study we introduce an approach to estimate AGB that does not rely on the indirect relationship to basic field measurements. Instead, our approach uses direct estimates of volume based on 3D data and basic density to derive AGB. We validate these terrestrial LiDAR derived AGB estimates by comparing them with destructively sampled AGB, and the results reflect a high level of agreement (CCC = 0.98). The total AGB of the 65 sampled trees is overestimated by 9.68%. AGB derived from local allometric equations shows an underestimation of 36.57% to 29.85% and the agreement with the reference data is lower (CCC = 0.68 to 0.78). Our research also demonstrates that AGB is not evenly distributed within the tree. For Eucalypt Open Forest, 80% of the AGB at plot level is located in the lower 60% of the trees.

TLS allows not only for testing of allometric equations, but the 3D data can also be used to develop and test new allometric relationships. This is of importance because large trees are not often harvested and measured for the calibration of allometrics, resulting in larger absolute error with increasing DBH. Our analysis demonstrates that TLS measurements can be efficiently modelled with quantitative structure models. This opens up the possibility of storing and analysing a broad spectrum of volumetric and other properties. For example, rather than merely calibrate allometric equations, we can define proper distributions of tree attributes and, in general, use all the available information.

## Acknowledgments

We thank Jacqui England for her help with the allometric equations and Bi Huiquan for his help with the fieldwork and suggestions for the manuscript.

# Chapter 5

# Investigating assumptions of crown archetypes for modelling LiDAR returns

This chapter is based on:

Calders, K., Lewis, P., Disney, M., Verbesselt, J. and Herold, M., 2013. Investigating assumptions of crown archetypes for modelling LiDAR returns. *Remote Sensing of Environment*, 134, 39-49.

***Abstract:*** LiDAR has the potential to derive canopy structural information such as tree height and leaf area index (LAI), via models of the LiDAR signal. Such models often make assumptions regarding crown shape to simplify parameter retrieval and crown archetypes are typically assumed to contain a turbid medium to account for within-crown scattering. However, these assumptions may make it difficult to relate derived structural parameters to measurable canopy properties. Here, we test the impact of crown archetype assumptions by developing a new set of analytical expressions for modelling LiDAR signals. The expressions for three crown archetypes (cuboids, cones and spheroids) are derived from the radiative transfer solution for single order scattering in the optical case and are a function of crown macro-structure (height and crown extent) and LAI. We test these expressions against waveforms simulated using a highly-detailed 3D radiative transfer model, for LAI ranging from one to six. This allows us to control all aspects of the crown structure and LiDAR characteristics. The analytical expressions are fitted to both the original and the cumulative simulated LiDAR waveforms and the CV(RMSE) of model fit over archetype trees ranges from 0.3% to 21.2%. The absolute prediction error (APE) for LAI is 7.1% for cuboid archetypes, 18.6% for conical archetypes and 4.5% for spheroid archetypes. We then test the analytical expressions against more realistic 3D representations of broadleaved deciduous (birch) and evergreen needle-leaved (Sitka spruce) tree crowns. The analytical expressions perform more poorly (APE values up to 260.9%, typically ranging from 39.4% to 78.6%) than for the archetype shapes and ignoring clumping and lower branches has a significant influence on the performance of waveform inversion of realistic trees. The poor performance is important as it suggests that the assumption of crown archetypes can result in significant errors in retrieved crown parameters due to these assumptions not being met in real trees. Seemingly reasonable inferred values may arise due to coupling between parameters. Our results suggest care is needed in inferring biophysical properties based on crown archetypes. Relationships between the derived parameters and their physical counterparts need further elucidation.

## 5.1 Introduction

Forest structure plays an important role in forest ecosystems. Leaf area index (LAI) is a meaningful structural parameter, since several biological and physical processes are related to the total leaf surface. For example, photosynthesis, respiration, transpiration, carbon and nutrient cycles, and rainfall interception are a function of forest structure and LAI.

Active sensors such as LiDAR (light detection and ranging) can measure something approximating the retroreflectance as a time or distance resolved signal over forest canopies. LiDAR therefore can serve as an excellent tool to assess forest structure and the three-dimensional distribution of plant canopies (Vauhkonen et al., 2009; Koch et al., 2006; Lefsky et al., 1999; Nelson, 1997). Although many studies have examined the possibilities that LiDAR offers in structure assessment, little work has been conducted on quantitative LiDAR data interpretation, i.e. relating the LiDAR signal to the fundamental principles governing the scattered signal. Barbier et al. (2011) studied how canopy structure interacts with physical signals (light) at forest stand level. However, a better understanding of the physical underpinnings of light interaction with canopy structure at tree level is needed, for example, to optimise fusion with optical and LiDAR data. In this study, we will therefore look at single tree LiDAR signals in an effort to understand the information content of such LiDAR signals. Here, the relationship between LiDAR and vegetation structure is studied and quantified in the nadir direction.

Many LiDAR studies are based on the assumptions of crown archetypes and some examples are listed in table 5.1. Ferraz et al. (2012), Riaño et al. (2004), Lim et al. (2003) and Ni-Meister et al. (2001) assumed ellipsoidal crowns. North et al. (2010) and Wang & Glenn (2008) used both conical and ellipsoidal crown shapes to characterise the crown. Goodwin et al. (2007) described crowns as hemi-ellipsoids and Koetz et al. (2007) also assumed crowns were shaped as hemi-ellipsoids when simulating large footprint LiDAR over simulated forest stands. Hyde et al. (2005) used four archetypes to characterise the trees in their study area: elliptical, umbrella-shaped, conical and cylindrical. They used vegetation type as a proxy for crown shape, e.g. stands of pure red fir were assumed to be conical or pointed, while deciduous crowns were assumed to be more rounded. Sun & Ranson (2000) modelled crown shapes as cones, ellipsoids and hemi-ellipsoids. Kato et al. (2009) did not make assumptions about some sort of archetype but used a wrapped surface reconstruction approach based on the LiDAR point cloud to generate the crown shape. A common approach to describe the distribution of foliage within archetype crowns is to use a turbid medium model, which assumes a constant leaf area density throughout the crown (North et al., 2010; Koetz et al., 2007; Sun & Ranson, 2000).

Earlier work on complex modelling approaches for LiDAR waveforms mainly focused on understanding some of the influences on the waveform. Sun & Ranson (2000) presented

**Table 5.1:** Examples of LiDAR studies using crown archetypes.

| Reference | Crown archetype |
|---|---|
| Ferraz et al. (2012) | Ellipsoidal |
| North et al. (2010) | Ellipsoidal & Conical |
| Wang & Glenn (2008) | Ellipsoidal & Conical |
| Koetz et al. (2007) | Hemi-ellipsoidal |
| Goodwin et al. (2007) | Hemi-ellipsoidal |
| Hyde et al. (2005) | Elliptical, Umbrella-shaped, Conical & Cylindrical |
| Riaño et al. (2004) | Ellipsoidal |
| Lim et al. (2003) | Ellipsoidal |
| Ni-Meister et al. (2001) | Ellipsoidal |
| Sun & Ranson (2000) | Ellipsoidal, Conical & Hemi-ellipsoidal |

a 3D model for simulating LiDAR waveforms from forest stands. Their results showed that LiDAR waveforms are an indication of both horizontal and vertical structure of forest canopies. Kotchenova et al. (2003) introduced a time-dependent stochastic radiative transfer theory, which allowed for a more realistic description of clumping and gaps. Ni-Meister et al. (2001) used a hybrid geometric optical and radiative transfer model (GORT) to interpret the LiDAR waveforms with respect to canopy structure and validated their findings using SLICER data. Gap probability was identified as the most important link between canopy structure and modelling LiDAR waveforms. LiDAR simulations in Blair & Hofton (1999) suggested that multiple scattering in vegetation canopies did not contribute significantly to the LiDAR waveform shape and several other LiDAR modelling studies also assumed single scattering only (Sun & Ranson, 2000; Ni-Meister et al., 2001; Goodwin et al., 2007).

Empirical relationships often make assumptions, which lead us away from the fundamental scattering properties, making it hard to relate the derived structural parameters to real canopies. In this study we return to a limited number of assumptions based on radiative transfer (RT). These assumptions are: crown archetypes, constant leaf area density throughout the crown and first order scattering. We adopt these widely-used assumptions in order to quantify their impact in deriving canopy parameters from LiDAR observations. We address the question of whether simple crown archetype assumptions can be used to model LiDAR scattering. If these assumptions hold up, analytical expressions for LiDAR scattering would be preferred over empirical relationships, because those analytical solutions will allow retrieval of crown parameters that are physically interpretable. If such crown archetype assumptions are shown not to be valid, the analytical expressions will give insight into why this is and what implications this will have for inverting LiDAR

signals using these assumptions. The main objectives of this paper are:

1. The derivation of analytical formulae that express the LiDAR reflectivity as a function of crown macro-structure parameters and crown leaf area density for a nadir configuration;
2. The testing of these formulae against realistic LiDAR simulations; and
3. The quantification of impact of crown archetype assumptions on retrieval of LAI.

Such formulae, for single trees, are potentially of great value themselves for understanding and deriving information. Solving for canopy properties using analytical expressions allows crown structure to be extracted from LiDAR waveforms. We present analytical expressions for a nadir configuration obtained by solving the 3D integral for photon transport in a specific envelope crown shape. We test these expressions by comparison with realistic LiDAR simulations of which all variables are known. Various 3D tree models are created, which conform to the assumptions underlying our analytical expressions. LiDAR signals from these crowns are simulated using a Monte Carlo ray tracing radiative transfer model. In this way, we can control all aspects of the crown structure and the (simulated) signal properties, which would not be possible using measured LiDAR data. Trees with simple archetype crown shapes are analysed first to fully understand these waveforms. More realistic representations of broadleaved deciduous (birch) and evergreen needle-leaved (Sitka spruce) trees are then considered, which we use to elucidate some of the more interesting aspects of when and why simple models might fail. Finally, we discuss the likely impact of assumptions of crown archetypes on interpreting LiDAR signals and we outline ways in which these impacts can be quantified. This work is of importance due to the increasing requirement for accurate, physically-realistic retrieval of canopy parameters from LiDAR data.

## 5.2 Methods

### 5.2.1 Describing LiDAR reflectivity as a function of tree structure

In this section, we derive analytical formulae to describe LiDAR reflectivity as a function of different structural tree parameters for a nadir configuration. We use an approach based on the solution to the scalar radiative transfer equation for a plane parallel medium, which assumes vertical homogeneity within canopy layers and Lambertian scattering from objects. We then adjust the solution for the standard case for vertical heterogeneity inside the canopy. As a result, we can describe light passing through archetype crown shapes as cuboids, cones and prolate spheroids (hereafter referred to as spheroids). Several LiDAR studies (Sun & Ranson, 2000; Ni-Meister et al., 2001; Goodwin et al., 2007) assumed

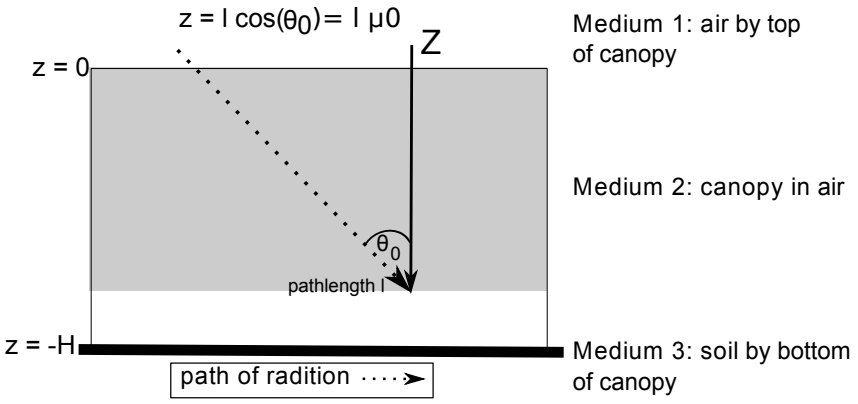


**Figure 5.1:** Overview of a plane parallel canopy medium: the top of the canopy is at z=0 and the path of radiation has length l.

single scattering only and LiDAR simulations over vegetation canopies in Blair & Hofton (1999) suggested that there was no significant contribution of multiple scattering to the LiDAR waveform shape. We tested that for a spheroid archetype more than 98.5% of the returned LiDAR reflectance was coming from the first order scattering when there was a single tree in the LiDAR footprint. Testing over a canopy with multiple trees in the LiDAR footprint showed a first order scattering domination of 91.1%. All tests were done at wavelength 1064 nm for plate leaf crowns using the *librat* radiative transfer model with settings specified in section 5.2.2. It is therefore a reasonable assumption to only consider first order scattering (i.e. only one interaction with soil or canopy elements) in this study.

### A solution to the scalar radiative transfer equation for a LiDAR signal

The solution for first order scattering in the optical case is used to reconstruct the LiDAR waveform over a plane parallel canopy medium theoretically (see figure 5.1). If $\Omega_s$ is the direction of scattering and $\Omega_0$ the direction of the incident LiDAR pulse then $I(\Omega_s, z)$ is the received single scattering energy by the sensor at depth $z$ in direction $\Omega_s$ over a plane parallel canopy.

$$I(\Omega_s, z) = e^{\frac{-\kappa_e(\Omega_s)(z-(-H))}{\mu_s}} \rho_{soil}(\Omega_s, \Omega_0) e^{\frac{-\kappa_e(\Omega_0)(-H)}{\mu_0}} I_0 d(\Omega_s - \Omega_0) + \frac{I_0}{\mu_s} \int_{Z=-H}^{Z=z} e^{\frac{-\kappa_e(\Omega_s)(z-Z)}{\mu_s}} e^{\frac{\kappa_e(\Omega_0)Z}{\mu_0}} P(\Omega_0 \to \Omega_s)\, dZ \tag{5.1}$$

$I_0$ refers to the incident radiation intensity on top of the canopy. The volume scattering phase function is defined as $\mathrm{P}(\Omega_0 \to \Omega_s) = \frac{u_l}{\mu_s}\Gamma(\Omega_0 \to \Omega_s)$ where $\Gamma(\Omega_0 \to \Omega_s)$ is the area

scattering phase function. The volume scattering phase function defines that part of the radiation coming in the direction $\Omega_0$ which is scattered by a unit volume in a particular direction $\Omega_s$. The area scattering phase function is the part of the radiation coming in the direction $\Omega_0$ which is scattered by a unit area in a particular direction $\Omega_s$ (Ross, 1981). $u_l$ is the leaf area density function, which describes the area of leaves per unit volume. $\mu$ is the cosine of the direction vector $\Omega$ with the local normal, $Z$, and accounts for path length through the canopy. In this study, the sensor emits and receives LiDAR pulses at nadir and therefore $\mu_s$ and $\mu_0$ were equal to $\cos(0°) = 1$. Both $\mu_s$ and $\mu_0$ need to be re-introduced to work out the equations for off-nadir conditions. In the specific case of a LiDAR sensor, $\Omega_s = -\Omega_0$ and therefore this direction is called $\Omega$. The optical extinction coefficient $\kappa_e$ describes the probability per unit length that a photon encounters a canopy element in the direction of travel. According to Ross (1981), $\kappa_e$ can be written as $u_l G(\Omega)$. $G(\Omega)$ is the foliage orientation function and equals the projection of a unit area of foliage on a plane perpendicular to the direction $\Omega$, averaged over elements of all orientations. LiDAR sensors operate in the so-called hotspot, i.e. where view and illumination angles coincide. In this retroreflection direction the probability of a photon being able to follow the same path back up through the canopy as it took on its way down through the canopy is 1 and therefore we need to account for the joint gap probability. We are not only interested in the final returned energy, but also in the intermediate interactions at each level of $z$. Therefore equation 5.1 can be integrated with different limits of [0,-$z$], where $z$ is any value between 0 (i.e. top of the canopy: see figure 5.1) and $H$ (i.e. tree height). The received single scattering energy by the LiDAR sensor, looking in a specific direction $\Omega$, as function of canopy depth $z$ can be expressed as $I(\Omega, 0, z)$. The 0 in $I(\Omega, 0, z)$ indicates that the LiDAR sensor is located above the canopy ($z$=0 at the top of the canopy).

$$I(\Omega, 0, z) = e^{-G(\Omega)u_l H}\rho_{soil}(\Omega)I_0 d(\Omega) + \frac{I_0\Gamma(\Omega \rightarrow -\Omega)}{G(\Omega)}\left[1 - e^{-G(\Omega)u_l z}\right] \tag{5.2}$$

The focus in this study is on describing the LiDAR waveform of the crown, which is a plane parallel canopy in this section. For ease of reference, only the crown contribution of equation 5.2 will therefore be considered in the derivation of the analytical expressions, i.e.

$$I(\Omega, 0, z)_{crown} = \frac{I_0\Gamma(\Omega \rightarrow -\Omega)}{G(\Omega)}\left[1 - e^{-G(\Omega)u_l z}\right] \tag{5.3}$$

To reconstruct the LiDAR waveform, the contribution of each individual infinitesimal horizontal crown layer is needed. This is achieved by taking the derivative with respect to $z$:

$$\frac{dI(\Omega, 0, z)_{crown}}{dz} = I_0\Gamma(\Omega \rightarrow -\Omega)u_l e^{-G(\Omega)u_l z} \tag{5.4}$$

### Interpretation of LiDAR waveforms over single crown archetypes

In this section we derive analytical expressions to describe LiDAR waveforms over single crown archetypes for a nadir configuration. An analytical description of the waveform is preferred over a numerical approach, because it establishes a direct and stronger link with effective crown structure parameters. In section 5.2.1 we described the analytical expression for a LiDAR waveform of a plane parallel canopy medium, which implied that the whole of the LiDAR footprint is covered by the canopy. This is not necessarily true when we use single trees and therefore we will introduce a factor $C$ that accounts for the portion of the LiDAR footprint that is covered by the horizontal crown extent. $C$ is therefore the canopy cover, which can range from zero to one.

Our approach treats the crown shapes as a summation of homogeneous annuli with equal effective penetration depth $z'$ centred around the vertical axis (i.e. elevation axis). Unlike a numerical approach, the vertical interval (i.e. the bin step) and annulus width are infinitesimal and therefore the analytical expression can be seen as an integral.

By definition, the effective penetration depth ($z'$) within the plane parallel canopy medium is constant throughout the extent of any horizontal layer. The top of the canopy is earlier defined as the origin of the z-axis ($z = 0$) and therefore the value $z$ (the depth with respect to the top of the canopy) is equal to the value $z'$ (the effective penetration depth within the crown) for a plane parallel canopy. This is also true for cuboid crown archetypes since the horizontal extent of each horizontal crown layer is constant. This is not the case for irregular crown shapes (conical and spheroid). For these crown archetypes the horizontal extent changes with depth into the crown, which is illustrated in figure 5.2 and 5.3 and discussed below.

### Cuboid archetypes

The top of the crown in this case is a horizontal plane and $z'$ is constant throughout the extent of any horizontal layer (i.e. $z$ equals $z'$ at any position in a horizontal layer). Therefore we can describe the behaviour of photons passing through a cuboid crown by introducing the canopy cover $C$ to equation 5.4:

$$\frac{dI(\Omega, 0, z)_{crown}}{dz} = CI_0\Gamma(\Omega \rightarrow -\Omega)u_l e^{-G(\Omega)u_l z} \tag{5.5}$$

This expression can be solved for LAI by substituting $\frac{A_{cover}LAI}{V_{tot}}$ for $u_l$ where $A_{cover}$ is the area of the tree cover projection and $V_{tot}$ the total tree volume. For cuboid archetypes this substitution therefore becomes $u_l = \frac{LAI}{h}$ where $h$ is the crown height.

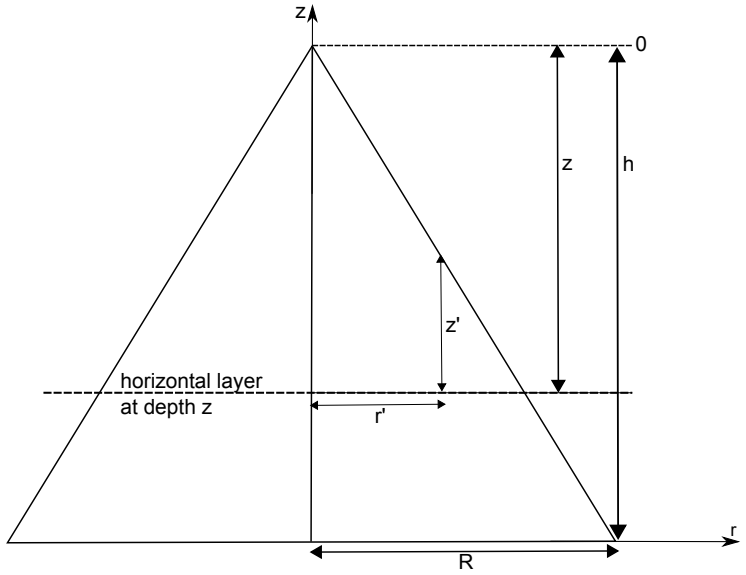


**Figure 5.2:** The vertical cross section of conical crown. $z$ is the depth with respect to the top of the canopy and $z'$ is the effective penetration depth within the crown. $R$ is the maximum crown radius at $z = h$. For a horizontal layer at depth $z$, the radius at this depth, $r$, equals $\frac{Rz}{h}$. At this layer, $r'$ can be any intermediate position in the interval $\left[0, \frac{Rz}{h}\right]$.

### Conical archetypes

In this case, within one horizontal layer at a specific depth $z$, different parts of the crown will be subject to different within-crown path lengths $z'$. Therefore the expression for the general (cuboid) case needs to be adjusted for shapes which have different $z'$ values within a single horizontal layer. Based on equation 5.5, it follows that

$$\frac{dI(\Omega, 0, z)_{crown}}{dz} = CI_0\Gamma(\Omega \rightarrow -\Omega)u_l e^{-G(\Omega)u_l z'} \tag{5.6}$$

Each horizontal layer can be seen as the sum of infinitesimal annuli with constant $z'$. The reflectance of each annulus is the product of equation 5.6 with its area. The total reflectance of a horizontal layer therefore is the integral over all the annuli. Figure 5.2 illustrates that for a horizontal layer at depth $z$, the radius at this depth, $r$, equals $\frac{Rz}{h}$. $R$ is the maximum crown radius at $z = h$. Therefore the integral needs to be calculated for the $r'$ interval $\left[0, \frac{Rz}{h}\right]$, where $r'$ can be any intermediate position in the interval. Normalising is achieved by dividing by $\pi R^2$:

$$\frac{dI(\Omega, 0, z)_{crown}}{dz} = C \int_{r'=0}^{r'=\frac{Rz}{h}} \frac{I_0\Gamma(\Omega \rightarrow -\Omega)u_l\left(e^{-G(\Omega)u_l z'}\right)2\pi r' dr'}{\pi R^2} \tag{5.7}$$

From figure 5.2 it can be seen that $z'$ is a function of $z$ and $r'$: $z' = z - \frac{hr'}{R}$ and the

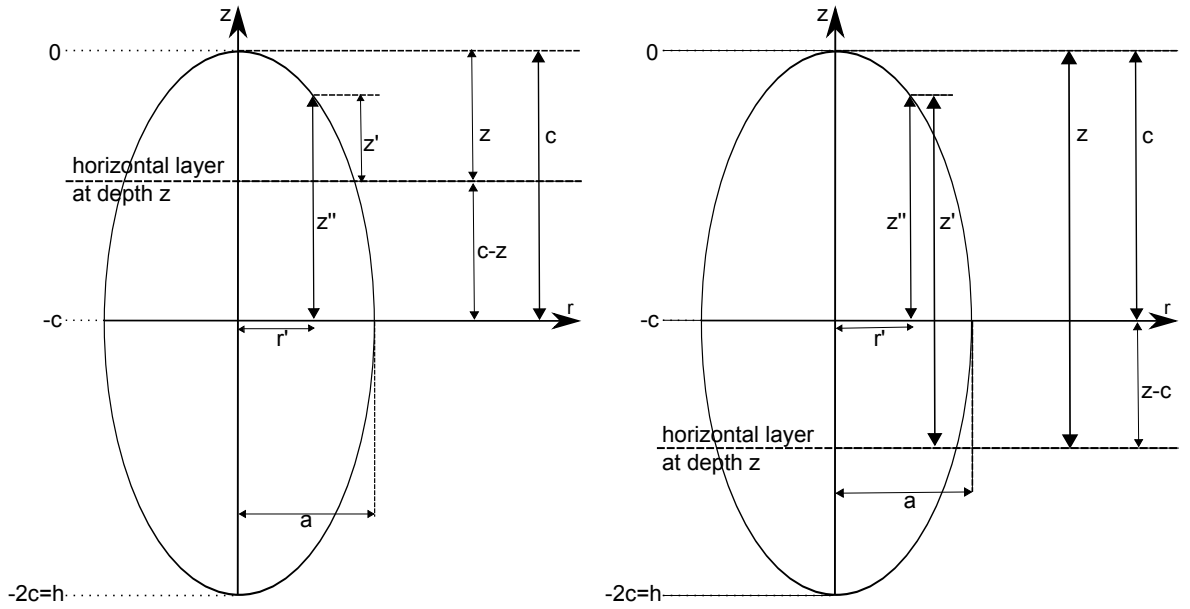


**Figure 5.3:** The vertical cross section of a spheroid crown is an ellipse described by $1 = \frac{r'^2}{a^2} + \frac{z''^2}{c^2}$ where $a$ is the semi-minor radius and $c$ is the semi-major radius. $z$ is the depth with respect to the top of the canopy and $z'$ is the effective penetration depth within the crown. For a horizontal layer at depth $z$, the radius at this depth is $r$ and $r'$ can be any intermediate position in the interval $[0,r]$. (left) Upper hemisphere; (right) Lower hemisphere.

integral (equation 5.7) can be solved, giving

$$\frac{dI(\Omega,0,z)_{crown}}{dz} = C\frac{2I_0\Gamma(\Omega \rightarrow -\Omega)}{h^2 G(\Omega)}\left(z - \frac{1}{G(\Omega)u_l} + \frac{e^{-G(\Omega)u_l z}}{G(\Omega)u_l}\right) \tag{5.8}$$

This expression can also be expressed as a function of LAI by substituting $\frac{3LAI}{h}$ for $u_l$.

### Spheroid archetypes

Based on figure 5.3, the equation of the ellipse (i.e. the vertical cross section of the prolate spheroid) can be written as $1 = \frac{r'^2}{a^2} + \frac{z''^2}{c^2}$ and therefore $z'' = c\sqrt{1 - \frac{r'^2}{a^2}}$ and $r' = a\sqrt{1 - \frac{z''^2}{c^2}}$ where $(r',\ z'')$ are the locations of the points on the surface of the envelope that shapes the ellipse. $r'$ is rewritten in terms of $z$ as $a\sqrt{1 - \frac{(c-z)^2}{c^2}}$ and will serve as the upper boundary of the integral over $r'$. For the upper hemisphere of the crown, $z'$ can be expressed as $z'' - (c - z) = c\sqrt{1 - \frac{r'^2}{a^2}} - (c - z)$. The expression for the

spheroid case is obtained similar to equation 5.7 since spheroids and cones both have a circular horizontal cross section (for the spheroid case $R = a$).

$$\begin{aligned}&\frac{dI(\Omega,0,z)_{crown,upper}}{dz}\\&= C\frac{2I_0\Gamma(\Omega\rightarrow-\Omega)}{G(\Omega)c}\left(\frac{c-z}{c}+\frac{1}{G(\Omega)u_l c}-e^{-G(\Omega)u_l z}\left(1+\frac{1}{G(\Omega)u_l c}\right)\right)\end{aligned} \tag{5.9}$$

From figure 5.3 it can be seen that the expression for $z'$ for the lower hemisphere is identical to the $z'$ expression for the upper hemisphere. However, the limit for the upper border of the integration interval for $r'$ is different: $a\sqrt{1-\frac{(z-c)^2}{c^2}}$. The expression for the lower hemisphere is obtained analogous to the upper hemisphere of the spheroid crown, i.e.

$$\begin{aligned}\frac{dI(\Omega,0,z)_{crown,lower}}{dz} = C\frac{2I_0\Gamma(\Omega\rightarrow-\Omega)}{G(\Omega)c}&\left(e^{-2G(\Omega)u_l(z-c)}\left(\frac{z-c}{c}+\frac{1}{G(\Omega)u_l c}\right)\right.\\&\left.-e^{-G(\Omega)u_l z}\left(1+\frac{1}{G(\Omega)u_l c}\right)\right)\end{aligned} \tag{5.10}$$

Equation 5.9 is used when $0 \leq z \leq c$ and equation 5.10 is applied when $c \leq z \leq 2c$. Both expressions can be written as a function of LAI by substituting $\frac{3LAI}{4c}$ for $u_l$.

### 5.2.2 Testing the analytical expressions

In the previous section, the analytical expressions of light passing through a crown and back to the LiDAR sensor were described for cuboid, conical and spheroid crowns. To test those expressions, a set of simplified trees with varying structural attributes is generated. These generated trees are used to create LiDAR simulations to test the analytical formulae. The modelled, detailed full 3D models allow us to control all parameters and exclude uncertainty introduced by e.g. scan angle, terrain or atmosphere.

#### Generating tree models

Three crown shapes are considered when generating simplified tree models: cuboids, cones and spheroids. Cuboid archetypes are specified by height, width and length. In this case, width and length are equal so the cross section for cuboid trees is square. Conical archetypes are determined by the height and base radius of the crown. The spheroid archetypes are parametrised by the semi-major radius and semi-minor radius and shape

is obtained by rotating an ellipse around its semi-major axis. The trunk underneath the crown is constructed by a single cylinder, parameterised by its height and radius: the trunk radius is fixed at 0.2 m for every tree and the trunk height is set to a quarter of the crown height. Leaves are the only material present in the canopy (no branches etc.) and are shaped as small disks with a radius of 0.01 m. This is similar to the leaf radius of 0.025 m assumed in (North et al., 2010). Previous LiDAR studies (North et al., 2010; Koetz et al., 2007; Kotchenova et al., 2003; Sun & Ranson, 2000) used a foliage orientation function, $G(\Omega)$, of 0.5. Therefore we will use a uniform leaf angle distribution and leaves are not permitted to overlap. The final parameter used to parametrise the crown is the LAI. In this study, LAI ranges from one to six and this parameter is interpreted as the one-sided area of leaf surface per unit ground surface area (Jensen, 2007). The leaf area density function $u_l$ is dependent on the position in the canopy. When $\mathrm{N}_v$ is the leaf number density (i.e. the number of leaves per unit volume) and $\mathrm{A}_l$ is the leaf area, the leaf area density at depth z is $u_l(z) = \mathrm{N}_v(z)\mathrm{A}_l$.

For the trees with an archetype crown shape, $\mathrm{A}_l$ is constant because all the leaves had the same dimensions and the leaf angle distribution is uniform. The leaves are spread equally over the crown and therefore $\mathrm{N}_v$ is constant as well. $u_l$ is therefore constant throughout the crown and units are [$\mathrm{m}^2$ / $\mathrm{m}^3$]. Three components are considered in the final tree models: leaves, trunk and soil. Each of these elements has its own spectral reflectance function. The functions used for these trees are similar to the reflectance properties used in previous studies (Disney et al., 2010, 2006). The birch and Sitka spruce tree models that were utilised in Disney et al. (2009) are used as realistic broadleaved deciduous and conifer tree models. The three-dimensional birch models were derived from the OnyxTREE© software (www.onyxtree.com) and were parameterised with field data obtained in a birch forest in Sweden. Radiometric properties are the same as for the archetype tree models. The 3D structure of Sitka spruce was derived from the PINOGRAM model (Leersnijder, 1992), modified as described in Disney et al. (2006).

### LiDAR simulations

LiDAR waveforms are numerically simulated by a Monte Carlo ray tracing (MCRT) approach. In this study the *librat* MCRT model, a library of C functions, is used. This model is based on the *ararat/drat* MCRT model (Lewis, 1999) and has been tested in previous studies against other models (Pinty et al., 2004; Widlowski et al., 2007) as well as against observations (Disney et al., 2010, 2009, 2006). The wavelength used for the LiDAR simulations is 1064 nm and the scene reflectance is simulated as observed from nadir. The first order scattering contribution over single trees is simulated. The field-of-view (FOV), i.e. the angle which can be viewed by the sensor, is set to 0.208 degrees for all simulations. We use a large footprint of 20 m x 20 m. We prefer a square footprint, as opposed to the more realistic circular footprint, since it makes simulations easier. The shape of the

footprint has no influence on the testing because we examine whole tree waveforms and the full horizontal extent of the crown is covered by the footprint, regardless of its shape. The vertical bin step is set to 0.1 m. Sampling characteristics are defined by 100 primary sample rays per sampling unit.

### Testing of the analytical expressions using simulated LiDAR waveforms

The analytical expressions for describing LiDAR waveform (equations 5.5, 5.8, 5.9 and 5.10) are tested by comparing them against the numerically MCRT simulated LiDAR waveforms. The comparison is done for both the original waveforms and their respective cumulative values. LAI parameter estimation from the waveforms is done by inversion of the analytical expressions using the Levenberg-Marquardt algorithm (Marquardt, 1963; Levenberg, 1944). The inversion is evaluated by the coefficient of variation of the root mean squared error, CV(RMSE), to determine the best fit. The CV(RMSE) is defined as the RMSE normalised to the mean of the observed reflectance values. Unlike the RMSE, CV(RMSE) is unitless. This allows CV(RMSE)s to be compared to each other easily. Furthermore the absolute prediction error (APE) is calculated. This is a measure of accuracy and is defined as $\frac{|LAI_{true} - LAI_{estimated}|}{LAI_{true}}$ x 100%.

The analytical expressions are tested in three experiments and an overview of these experiments can be found in table 5.2. The inversion strategy is tested in the first experiment. In this experiment, we use prior knowledge of the tree and crown height to subset the crown signal from the whole tree waveform correctly. The inversion approach does not require prior knowledge or assumptions about the crown shape and has no land cover constraint. Once the crown signal is extracted, we rescale the original crown extent from 0 to 100, where 0 is the top of the crown (TOC) and 100 the bottom of the crown (BOC). In reality, however, often no prior information about tree and crown height is available. Therefore we introduce a simple subset algorithm to delimit the crown signal from the whole tree waveform. We test this subset algorithm in the second experiment in which we evaluate its accuracy and precision with respect to the LAI parameter estimation. This will lead to better insight on how sensitive the analytical descriptions are when tree and crown height are not known. The aim of the subset algorithm is to find the TOC and BOC based on the comparison of the LiDAR reflectance value from a certain bin with a certain threshold. The subset algorithm searches the recorded waveform, starting at the smallest bin. The TOC is then defined as the waveform bin before the first 3 consecutive reflectance values above a certain threshold. The BOC is the first bin of the first 3 consecutive reflectance values below this threshold after the detection of the TOC. This threshold is subject to the noise in the simulated signal. Monte Carlo methods provide a stochastic simulation and will always contain (random) statistical variation, i.e. simulation noise. Disney et al. (2000) discussed that this does not have to be a disadvantage

**Table 5.2:** Overview of the 3 experiments that are used to test the analytical expressions.

| | Testing | Tree models | Prior information about crown height |
|---|---|---|---|
| Experiment 1 | Inversion strategy | Archetype crowns | Available |
| Experiment 2 | Crown signal subset algorithm | Archetype crowns | Unavailable |
| Experiment 3 | Crown archetype assumptions | Realistic crowns | Unavailable |

and the potential for deriving an understanding of the random error in the simulation can be considered a major advantage over numerical methods. The explicit representation of the canopy by a finite number of objects, rather than the infinitesimal (and therefore infinite number of) objects assumed in the general turbid medium approach, and hence the analytical formulae derived here, will influence the level of noise as well. The threshold we use in the subset algorithm is defined as 0.1% of the median returned reflectance and this value works for the level of noise in our simulations but remains a heuristic value. To determine this median, zero reflectance returns are filtered out first. Alternatively, more sophisticated approaches such as Hancock et al. (2011) could be used. In the third experiment we look at how these formulae apply to more realistic 3D vegetation structures, which do not fulfil all underlying assumptions of the derived formulae and have no prior information about tree or crown height.

## 5.3 Results

The analytical expressions (equations 5.5, 5.8, 5.9 and 5.10) are a combination of a scaling factor and a variable part, which is dependent on z. The scaling factor is assumed to be constant for a specific archetype crown and therefore it has no influence on the shape of its LiDAR waveform. Results of the same archetypes with different macro-structure parameters show similar results. Therefore we will only discuss the results of one example per archetype for the first two experiments. Crown height for the discussed examples is 6 m; cuboid crowns have a width and length of 2 m, conical crowns have a base radius of 2 m and spheroid crowns have a semi-minor radius of 2 m.

The first experiment tests the inversion strategy that is used in this study, i.e. the accuracy of the analytical expressions for describing LiDAR scattering, tested against full 3D simulations of the same. The results of these two experiment will indicate how well the analytical expressions work when crown archetype assumptions are met.

The second experiment compares our new analytical expressions for LiDAR waveforms against the simulated waveforms for archetype trees with fixed LAI (4) with no prior information about about the crown shape. Figure 5.4 shows the comparison of the analytical expressions against the simulated waveforms for archetype trees with LAI 4 in

the second experiment. The figure shows the optimal fit based on parameter estimation by the Levenberg-Marquardt algorithm. This figure clearly demonstrates that when the archetype crown assumptions are met, the LiDAR signal over a specific crown archetype will have a good fit with the corresponding analytical expression.

The inferred LAI values obtained by inverting the analytical expressions against the simulated waveforms of archetypes can be found in table 5.3 and the evaluation statistics of the analysis are summarised in table 5.4. The evaluation statistics from the first and and second experiment show that the inversion of the waveform of a cuboid or spheroid crown works best when the cumulative signal is used. The average CV(RMSE) for the cumulative waveform inversion of cuboid archetypes is 0.3% when crown height is known and 0.8% with no prior knowledge of crown height. The CV(RMSE) for spheroid archetypes is 0.3%, regardless of whether or not we know the crown height. The APE of the inversion

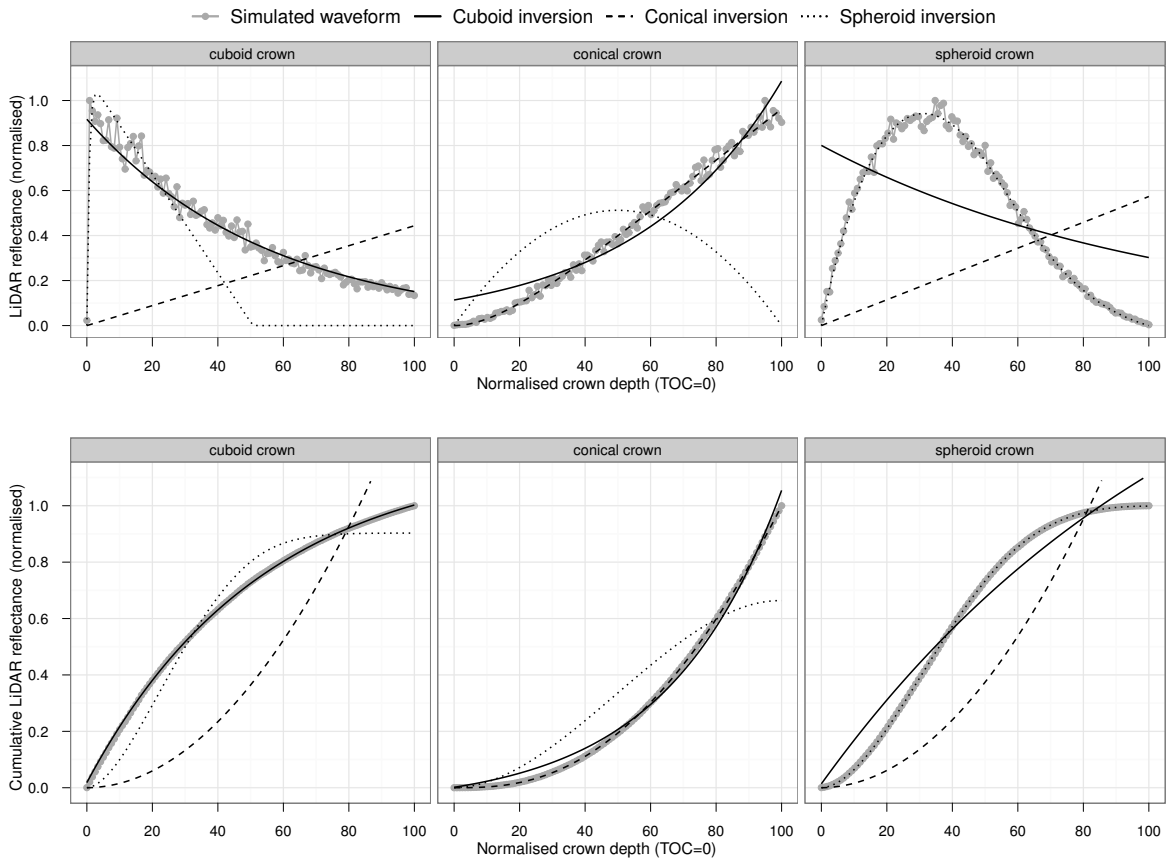


**Figure 5.4:** Testing of the analytical expressions against simulated waveforms for archetype crowns (cuboid, conical, spheroid) with LAI 4 with no prior information of tree and crown height (experiment 2). Crown depth ranges from 0 (top of crown) to 100 (bottom of crown). (upper row) Analysis of the original waveform; (lower row) Analysis of the cumulative waveform.

**Table 5.3:** LAI estimation from the waveforms of crown archetypes based on the Levenberg-Marquardt algorithm.

| | LAI estimation | | | | | | | | | | | |
|---|---|---|---|---|---|---|---|---|---|---|---|---|
| | Cuboid crown | | | | Conical crown | | | | Spheroid crown | | | |
| | Orig[1] | | Cumul[2] | | Orig | | Cumul | | Orig | | Cumul | |
| True LAI | hA[3] | hNA[4] | hA | hNA | hA | hNA | hA | hNA | hA | hNA | hA | hNA |
| **1** | 1.02 | 0.89 | 0.98 | 0.85 | 1.06 | 1.50 | 1.02 | 1.75 | 1.10 | 0.92 | 1.12 | 0.96 |
| **2** | 2.01 | 1.83 | 2.02 | 1.87 | 1.71 | 2.14 | 2.01 | 2.77 | 2.06 | 1.87 | 2.09 | 1.91 |
| **3** | 3.04 | 2.80 | 3.04 | 2.85 | 3.08 | 3.54 | 3.05 | 3.73 | 3.07 | 2.87 | 3.12 | 2.92 |
| **4** | 3.93 | 3.61 | 3.95 | 3.73 | 3.98 | 4.26 | 3.95 | 4.36 | 3.98 | 3.74 | 4.01 | 3.78 |
| **5** | 5.12 | 4.66 | 5.08 | 4.82 | 4.80 | 6.30 | 4.97 | 7.08 | 5.06 | 4.66 | 5.09 | 4.69 |
| **6** | 5.98 | 5.42 | 5.99 | 5.69 | 5.68 | 6.19 | 5.68 | 6.35 | 6.19 | 5.73 | 6.21 | 5.75 |

[1] Orig = Original
[2] Cumul = Cumulative
[3] hA = prior information about $h$ (crown height) is available: experiment 1
[4] hNA = prior information about $h$ (crown height) is not available: experiment 2

of the cumulative signal with no prior knowledge of the crown height is 7.1% for cuboid archetypes and 4.5% for spheroid archetypes. For conical crowns best fitting is achieved on the cumulative waveform (CV(RMSE) less than 0.7%), but the prediction based on the original LiDAR signal is more accurate, with an APE of 18.6% when the crown height is not known. This can also be seen in figure 5.5, which shows the MCRT simulated LiDAR wavforms of crown archetypes for LAI values ranging from one to six. This is because the cumulative LiDAR signals for different LAI values in conical crowns cover a smaller range of normalised LiDAR reflectance than the original waveforms and are therefore less distinguishable. Cumulative waveforms of cuboid and spheroid crowns are more distinguishable (figure 5.5). These results from the first and second experiment show that an archetype crown can be distinguished from among the three archetypes through model fitting using the Levenberg-Marquardt algorithm.

**Table 5.4:** Evaluation statistics of experiment 1 and 2: coefficient of variation of the RMSE and absolute prediction error averaged over LAI values one to six for crowns archetypes.

| | Cuboid crown | | | | Conical crown | | | | Spheroid crown | | | |
|---|---|---|---|---|---|---|---|---|---|---|---|---|
| | Original | | Cumulative | | Original | | Cumulative | | Original | | Cumulative | |
| | hA[1] | hNA[2] | hA | hNA | hA | hNA | hA | hNA | hA | hNA | hA | hNA |
| **CV(RMSE)** [%] | 8.8 | 21.2 | 0.3 | 0.8 | 6.0 | 6.0 | 0.4 | 0.7 | 5.3 | 5.4 | 0.3 | 0.3 |
| **APE** [%] | 1.5 | 8.7 | 1.3 | 7.1 | 5.5 | 18.6 | 1.9 | 32.4 | 3.3 | 6.0 | 4.4 | 4.5 |

[1] hA = prior information about $h$ (crown height) is available: experiment 1
[2] hNA = prior information about $h$ (crown height) is not available: experiment 2

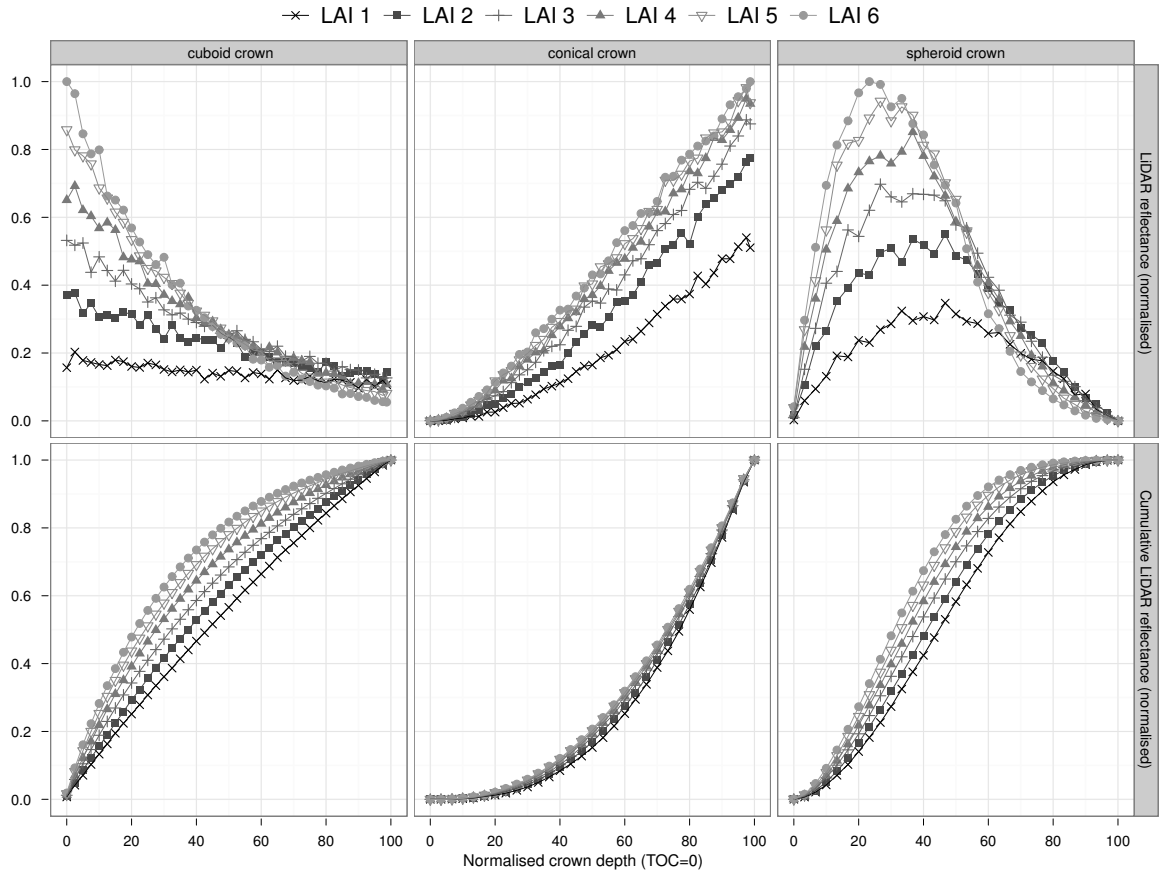


**Figure 5.5:** MCRT simulated LiDAR waveforms of crown archetypes (cuboid, conical, spheroid) for different LAI values. (upper row) Original waveform; (lower row) Cumulative waveform.

Figure 5.6 gives an overview of the testing of the analytical expressions against simulated waveforms of realistic 3D representations without prior knowledge of the crown height (experiment 3). Two birch trees and 2 Sitka spruce trees are used in this experiment, which looks at how the analytical expressions perform when the crown archetype assumptions are not met. The statistics for the inversion of the cuboid and spheroid expressions are summarised in table 5.5. Fitting a cumulative spheroid waveform works best for the first birch case (figure 5.6a): CV(RMSE) is 3.1% against 8.9% for the cumulative cuboid fitting. However, the prediction of the cuboid fit (APE 25.9%) is significantly better than the prediction of the spheroid fit (APE 260.9%). The inferred LAI using the cuboid inversion is 5.4 and the inferred LAI resulting from the spheroid fit is 15.3, with the true LAI for this birch tree being 4.3. Similar findings are observed in a less extreme way in the second birch case (true LAI 4.4, figure 5.6b), where a cumulative cuboid fit with a CV(RMSE) of 3.6% has an absolute prediction error of 39.4% (inferred LAI 2.7). Cumulative spheroid fitting has a higher CV(RMSE) of 8.5%, but a better APE of 25.8%

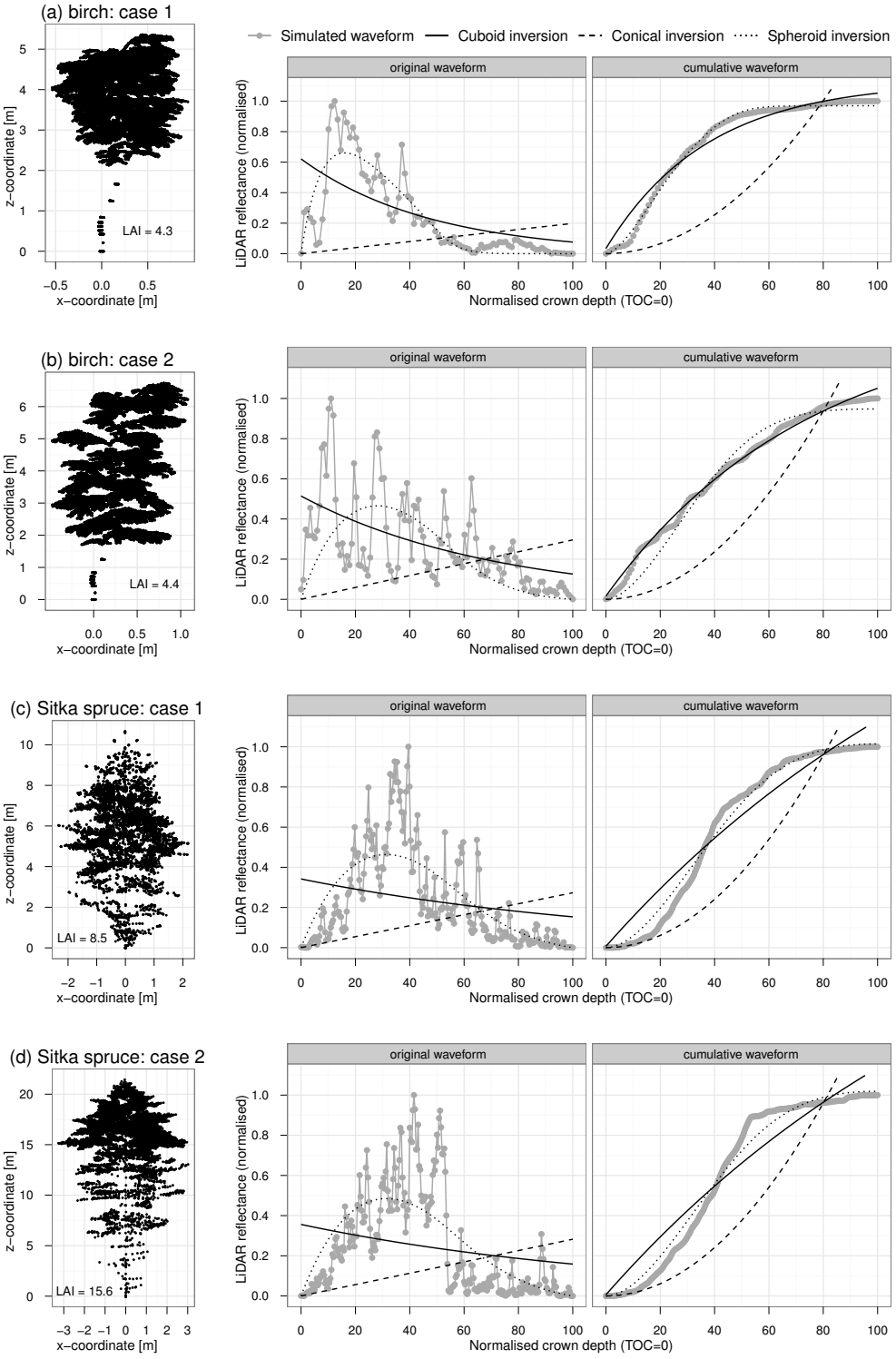


**Figure 5.6:** Testing of the analytical expressions against simulated waveforms for realistic 3D tree representations (experiment 3). (left) xz-cross-section of the tree structure; (middle) Analysis of the original waveform; (right) Analysis of the cumulative waveform.

**Table 5.5:** Estimated LAI values and evaluation statistics for realistic 3D trees (experiment 3).

| | | | birch case 1 | birch case 2 | Sitka spruce case 1 | Sitka spruce case 2 |
|---|---|---|---|---|---|---|
| | | **True LAI** | 4.3 | 4.4 | 8.5 | 15.6 |
| **Cuboid** | **Original** | **Estimated LAI** | 4.2 | 2.8 | 1.6 | 1.6 |
| | | **CV(RMSE)** [%] | 86.1 | 68.1 | 99.0 | 102.6 |
| | | **APE** [%] | 1.2 | 36.1 | 81.2 | 89.6 |
| | **Cumulative** | **Estimated LAI** | 5.4 | 2.7 | 1.3 | 1.3 |
| | | **CV(RMSE)** [%] | 8.9 | 3.6 | 16.6 | 17.9 |
| | | **APE** [%] | 25.9 | 39.4 | 84.9 | 91.7 |
| **Spheroid** | **Original** | **Estimated LAI** | 16.3 | 5.1 | 3.7 | 3.7 |
| | | **CV(RMSE)** [%] | 52.8 | 75.2 | 66.4 | 69.6 |
| | | **APE** [%] | 284.2 | 14.9 | 56.6 | 76.5 |
| | **Cumulative** | **Estimated LAI** | 15.3 | 5.5 | 3.3 | 3.3 |
| | | **CV(RMSE)** [%] | 3.1 | 8.5 | 6.8 | 8.1 |
| | | **APE** [%] | 260.9 | 25.8 | 60.7 | 78.6 |

(inferred LAI 5.5). The inversion of the cumulative spheroid expression leads to the best results for both Sitka spruce case studies (figure 5.6c&d). CV(RMSE) is less than 8.1% but the absolute prediction error is high, with a minimum of 60.7%. For the first sitka Spruce tree, the inferred LAI of 3.3 is smaller than the true LAI of 8.5. The second sitka Spruce case with true LAI 15.6 has a higher APE of 78.6% with the cumulative spheroid inversion of the LiDAR signal leading to an inferred LAI of only 3.3.

## 5.4 Discussion

Our results demonstrate that the analytical expressions for first order scattering are able to reconstruct the simulated LiDAR waveforms over crown archetypes satisfactorily in most cases. The first experiment gives similar results over the whole LAI range (1 to 6). We show that the models based on crown archetypes fit the 3D simulations less well when we do not have information on tree and crown height (as will often be the case in practice). However, our results indicate that when archetype assumptions are not met, models based on these assumptions can still fit observed LiDAR signals quite well, but, crucially, only by assuming unrealistic parameter values. In particular inversion of LiDAR signals over realistic tree crowns can lead to estimates of effective LAI, which will depart from the true LAI. Given the rapidly increasing use of LiDAR in studies of canopy

properties, we discuss the implications for using LiDAR models to retrieve and interpret canopy parameters.

Similar to findings in Ni-Meister et al. (2001), the key concept in these analytical expressions is the gap probability and its dependency on crown path length. The first experiment shows that the solved LAI values for crown archetypes have apparently small absolute prediction errors ranging from 1.3% to 5.5%. This shows that we established an analytical method to retrieve LAI based on the crown signal of the LiDAR waveform over crown archetypes. Not knowing tree and crown height in advance (and hence the crown signal can be delimited less accurately from the whole tree waveform) increased the absolute prediction error only marginally compared to the prediction errors from the first experiment. Results from the second experiment show that the prediction error increases by 5.8% for cuboid crowns, 13.1% for conical crowns and 0.1% for spheroid crowns. These marginal increases in prediction errors suggests that when the inversion method is applied with no prior knowledge of the crown extent or shape, it will still give an accurate estimate of the true LAI.

The results from the third experiment illustrate the importance of accurate crown signal detection within the whole tree waveform and the effect of within-crown clumping. The second Sitka spruce case (figure 5.6d) illustrates the importance of accurate crown signal detection. The simple subset algorithm we introduced fails to distinguish between crown and the lower branches because it requires the returned LiDAR reflectance to fall below a set threshold to detect the BOC. The signal from the lower branches will fuse with the crown signal and will indicate a wrong BOC. This will lead to a biased input signal for the inversion algorithm and therefore optimal inversion is not achieved. In the archetype trees, crowns were well defined and no lower branching was present. Therefore the simple subset algorithm to detect the crown signal in the whole tree waveform worked well in those cases. The results with the real trees suggest the need for a more robust method to delimit the correct crown signal in more realistic circumstances. Also the effect of topography plays an important role in the correct delineation of the crown signal from a large footprint LiDAR waveform. If the tree is located on a sloping terrain, the vegetation and ground return might overlap in the LiDAR waveform (Hancock et al., 2012). Approaches to reduce the effect of slope on the LiDAR signal could use a sensor design that is susceptible to the differences in the traits of vegetation and ground, such as multi-wavelength instruments. Alternatively, a digital terrain model could be used to predict the influence of the ground signal on the LiDAR signal.

The analytical expressions describe the LiDAR signal of a single tree having the full horizontal extent of the crown covered by the footprint. The shape of the LiDAR signal over multiple trees might become less distinct. For non-overlapping crowns, the resulting waveform would be the summation of linear transformations of the individual crown waveforms, which are quantified by the analytical expressions for single crowns. We cannot

deal with partial crowns (other than the cuboid archetype) so the results are only directly applicable to waveforms that contain some integer number of trees. A common approach to overcome this issue is by re-sampling smaller footprint LiDAR to mimic large footprint waveforms over single trees. Blair & Hofton (1999) aggregated high resolution small footprint elevation to mimic the footprint waveform of the LVIS instrument. Popescu et al. (2011) and Muss et al. (2011) both used discrete return LiDAR to create pseudo-waveforms. Popescu et al. (2011) used simulated pseudo-waveforms from airborne LiDAR to compare retrieval of aboveground biomass and forest structure between GLAS and airborne LiDAR. Muss et al. (2011) aggregated discrete LiDAR height and intensity into larger footprints so they could use the characteristics of traditional waveform LiDAR to asses forest structure. Reitberger et al. (2008) used small footprint waveform LiDAR in combination with tree segmentation to derive forest characteristics at tree level. Such an approach would depend on the forest type and how reliable trees could be isolated. Trees could be isolated more easily in open forest types (e.g. savanna), but it will be more challenging to isolate trees in denser environments (e.g. rainforest). Tang et al. (2012) derived LAI in tropical rainforests from LVIS waveforms (25 m footprint) with moderate success ($R^2$ ranging from 0.42 to 0.63) using the light transmittance within the canopy. The LVIS footprint covered multiple trees and the formulae used in their work implicitly assumed a crown shape equating to the cuboid crown archetype. If we take their analysis as typical, then the assumptions we tested in our abstraction are no different from those used in practice.

The plots in figure 5.6 illustrate that when the inversion method is applied to realistic tree crowns, which do not follow one of the assumed archetypes quite closely, the analytical expressions do not work so well. This may perhaps appear unsurprising: where the model assumptions are not met, our simplified models fail to pick up key aspects of the LiDAR signal. However many of the current approaches to modelling LiDAR signals in airborne laser scanning applications use some sort of assumption of crown archetype (table 5.1), and these models of course allow retrieval of parameters such as LAI and crown height. Our results show that caution should be given to the impact of such assumption on inferring biophysical parameters. Figure 5.6 suggests that, although assuming a crown archetype will provide a result, it can potentially be misleading when measured crowns depart from the archetypes. Similar conclusions were drawn in Calders et al. (2012), where LAI was inferred from realistic trees with lower LAI values (LAI ranging from 0.3 to 3.1 for eucalyptus and from 0.3 to 2.2 for birch).

The second birch case (figure 5.6b) is a good example of the effect of clumping on the waveform. This effect is clearly visible in the original LiDAR waveform. The cumulative waveform is more robust and hence less affected by clumping. Severe clumping means that the assumption of constant leaf area density is severely violated, so it is not surprising that results are poor (table 5.5). This is especially true in both birch cases, where the best fitting archetype does not necessarily lead to the most realistic inverted LAI value. The

results from the birch cases also illustrate the advantage of an inversion method which does not make any prior assumptions about crown archetype according to tree species as opposed to many current LiDAR studies. A spheroid crown fits best for the first birch case, but a cuboid crown provides a better fit for the second birch case. It is important to stress that, as mentioned above, best fit does not equate to best LAI inversion for the birch cases. In Kotchenova et al. (2003) a time-dependent stochastic radiative transfer theory was introduced to model the propagation of laser pulses in the crown and this was solved numerically. The approach allowed for a more realistic description of the canopy structure including clumping and gaps. A factor was used to describe the correlation between foliage elements in different layers (vertical heterogeneity). Although additional improvements need to be made to provide more accurate characterisation of the probability density function, this probability-based approach has the potential to improve our approach.

This work demonstrates the implications of crown archetype assumptions on inferring biophysical parameters from LiDAR signals. Canopy parameters inferred from realistic canopies using the archetype assumptions can be misleading as they are essentially effective parameters. That is, these derived parameters may be consistent with the assumptions of archetypes and hence allow inversion against observations, but they will not correspond to physically-measurable versions of these parameters. The key for applications of such models is understanding how the effective parameters are related to the real ones. We suggest that an analysis of the departure of the true waveform from the inverted waveform will provide more knowledge about the vertical clumping of all crown constituents. Clumping, along with the slope issue, is an area for future work. The analytical expressions, together with a MCRT radiative transfer to model LiDAR signals, are an ideal approach to further explore these issues.

## 5.5 Conclusions

Our research demonstrates a method for exploring the assumptions of crown archetypes, typically made when modelling LiDAR signals for parameter estimation. A unique feature of this work is the development of a new set of analytical expressions to describe LiDAR waveforms. Analytical expressions for three archetype crowns are derived based on the radiative transfer solution for single order scattering in the optical case. These expressions are tested against MCRT waveform simulations using a curve-fitting optimisation approach. Using simulations enabled us to control all aspects of the crown architecture and sensor properties to test the implications of such crown archetype assumptions for inferring LAI from LiDAR waveforms. Overall agreement is shown between the expressions and simulated signals over simplified trees. LAI estimates demonstrate only a small prediction error, even when there is no prior knowledge of the crown height for such trees. We then demonstrated that the analytical expressions did not function well when applied

to more realistic 3D representations of broadleaved deciduous (LAI ranging from 4.3 to 4.4) and evergreen needle-leaved (LAI ranging from 8.5 to 15.6) crowns, which depart significantly from the crown archetypes. Even if an archetype waveform fits the realistic data, it can potentially have very large (up to 260.9%, typically ranging from 39.4% to 78.6%) errors in inferred LAI. We suggest this discrepancy is largely due to within-crown clumping of the crown constituents. Our results indicate that assuming crown archetypes for parameter retrieval from LiDAR may be problematic if within-crown clumping is not accounted for. Such a negative outcome is of importance as LAI is closely relates to forest structure and plays an important role in forest ecosystems. The increasing use of LiDAR for forestry suggest prudence is needed in inferring LAI based on crown archetypes. These inferred values are essentially effective parameters that will not be measurable in practice.

## Acknowledgements

The authors thank the anonymous reviewers for their valuable suggestions to improve the manuscript. We also thank R. Dubayah for his helpful comments on the manuscript.

# Chapter 6

# Synthesis

## 6.1 Main findings

The main objective of this thesis is to explore the potential of terrestrial LiDAR to be used for the monitoring and assessment of forest structure at plot level scale, and to develop methods to derive accurate in-situ reference data. In this regard, four research questions are defined in the first chapter. Chapters 2 and 3 use single scan TLS data to quantify and monitor forest structure. Chapter 4 uses multiple registered scan locations to explicitly model the true tree architecture and estimate above-ground biomass (AGB). Chapter 5 investigates the assumptions of crown archetypes on inferring structural information from airborne/spaceborne LiDAR. The previous four chapters provide a detailed discourse on the research conducted in this thesis. In this chapter I will revisit and answer the research questions that are defined in chapter 1 based on the findings of this research.

**1. How can we derive topography-corrected vertical plant profiles from terrestrial LiDAR?**

Vertical plant profiles characterise the 3D distribution of canopy constituents and can be used for the rapid assessment of the vertical forest structure. TLS instruments record heights relative to the position and orientation of the instrument. The recorded heights should therefore be corrected for topography so that they represent the true height above the terrain (figure 1.2). Chapter 2 demonstrates that not correcting for topography when generating vertical plant profiles can lead to significant errors in the vertical distribution of plant constituents.

A method of deriving topography-corrected vertical plant profiles is introduced and local plane fitting through single scan TLS data is used to account for topography. Results are compared with vertical plant profiles that were corrected for topography using DTMs derived from airborne LiDAR. Such detailed DTMs are often not available or are expensive to acquire, but provide the best possible reference data for topography to validate the local plane fitting approach. The local plane fitting approach is tested in five different forest types with different topography and understorey. I show that using the plane fitting approach significantly reduced the error in height metrics derived from vertical plant profiles for these five plots. The major limitation of the local plane fitting approach is that it is not a good approximation in extreme cases where the instrument is put on top of a hill or at the bottom of a valley. For such cases, the use of a detailed DTM for topography correction is advised. A DTM can be derived from registered TLS scans if no ALS data is available, but this will result in significantly increased data acquisition time. Zhao et al. (2013) used five registered scan locations to derive vertical plant profiles for a red fir stand in the Sierra National Forest (CA, United States) using the Echidna® Validation Instrument (EVI) point cloud data. Similar to the approach in chapter 2 of this PhD thesis, ground returns are identified first. Due to the registration of different scan locations, occlusion in the point cloud data was reduced and a three-dimensional

surface was fitted to the EVI ground returns. The heights of the LiDAR points were then adjusted accordingly using this surface.

**2. How can we use TLS derived vertical plant profiles to monitor spring phenology?**

Chapter 3 builds on the methodology that is described and tested in chapter 2. Spring phenology, and more specifically the start of the growing season, is one of the key indicators for the effect of climate change (White et al., 2009). Unlike conventional ground-based optical techniques such as hemispherical photographs or the LAI-2000, terrestrial laser scanning is an active remote sensing technique and is not influenced by the illumination conditions in the forest. A robust and repeatable approach is established that requires no user interaction during data capture or derivation of the vertical plant profiles (chapter 2). Data noise is therefore kept to a minimum, which allows us not only to monitor seasonal increase in plant area index (PAI), but also to detect structural damage in the canopy, for example, after periods with increased wind speeds. I demonstrate that TLS measurements with high temporal resolution can effectively monitor phenology and capture structural changes in PAI throughout the growing season. This sensitivity to subtle structural changes demonstrates the potential for other applications, such as monitoring forest recovery after (selective) logging or fire damage.

Compared to conventional ground-based optical techniques, TLS is a practical and robust tool to monitor seasonal dynamics as a function of time, as well as a function of canopy height. A single TLS measurement can monitor different horizontal layers independently, whereas the conventional methods require multiple measurements at different heights to make a vertical differentiation. In chapter 2, I demonstrate the advantage of a multiple return over a first return TLS instrument. Multiple return TLS data not only improves the definition of true ground returns when the herbaceous understorey is dense, it also leads to improved sampling at greater canopy heights. Figure 3.5 suggests that the latter may be important for monitoring phenology throughout the whole year. After a period of rapid growth followed by a period of stable PAI, an additional moderate increase is occurring, primarily in the upper part of the canopy.

The main limitation of the current method of generating vertical plant profiles is the exclusion of the larger zenith angles. Profiles that cover the 30-70° zenith angle range are generated in chapter 2 and this range is extended so that profiles cover the 5-70° zenith angle range in chapter 3. The 0-5° zenith angle range is excluded because there is high variance at low zenith angles, with large gaps near the zero zenith angle (Jupp et al., 2009), and because the upper zenith rings are unable to sample the spatial variance (Lovell et al., 2012). Inclusion of larger zenith angles would extend the vertical plant profiles to the ground and allow us to better monitor the woody and herbaceous understorey. This is a key subject of future work and would broaden the potential applications for vertical plant profiles, for example for better fuel load characterisation for fire management or

better understanding of animal habitat dynamics.

**3. How can we use TLS point clouds to estimate above-ground biomass?**

Chapters 2 and 3 use single scan data to calculate the vertically resolved gap fraction and to describe the plant area volume density (PAVD) as a function of height. Chapter 4 uses multiple scan locations that are registered to a single point cloud. Setting up registration targets significantly increases the data acquisition time, but allows us to reduce occlusion effects in the TLS data.

Traditional field inventories generally measure DBH and height and infer AGB based on the allometric relationships with these tree parameters (Chave et al., 2014; Bi et al., 2004). Chapter 4 demonstrates not only that DBH can be extracted accurately from TLS data, but that these derived tree heights show better agreement with the reference heights from destructive harvesting than traditional field height inventories do. The key advantage of TLS point clouds over traditional field inventory is being able to directly reconstruct 3D tree models from which volume can be inferred. AGB can then be derived from these volume estimates using basic density information. TLS derived AGB is therefore independent of indirect relationships of AGB with DBH and tree height. The TLS AGB estimates are validated by comparing them with destructively sampled AGB from 65 trees and a high level of agreement is found (CCC = 0.98), with the total AGB being overestimated by 9.68%. AGB inferred from local allometric equations shows an underestimation of 36.57% to 29.85% and the agreement with the reference data is significantly lower (CCC ranging from 0.68 to 0.78).

Chave et al. (2004) identified four types of uncertainty in AGB assessment using traditional forest inventory data: (i) errors in tree measurements, (ii) errors in the allometric model, (iii) errors related to the sampling plot size, and (iv) errors related to the landscape-scale representation of the sampling plots. In this PhD thesis, I contribute to reducing errors (i) and (ii) and section 6.2.3 will discuss the potential of TLS data regarding the reduction of errors (iii) and (iv), which are related to spatial variance.

The key result of chapter 4 is that the error for AGB estimates from TLS is not dependent on DBH, whereas the error for AGB estimates using allometric equations increases exponentially with increasing DBH (figure 4.10). This is not surprising since the performance of allometric equations depends on the calibration data. It is often impractical and expensive to harvest large trees and they are therefore often under-represented in the calibration data, resulting in larger errors with increasing DBH. The approach in chapter 4 not only demonstrates that we can effectively model tree volume using quantitative structure models, but that the availability of TLS data also offers opportunities to develop and test new allometrics without having to harvest the calibration data.

Access to destructively sampled reference data is essential for the validation of the QSM approach. The results presented in chapter 4 are limited to data from native Eucalypt

Open Forest in Australia, but the QSM method should, in theory, work for most tree species. Deploying the QSM method to other, more densely forested, environments will impose new challenges regarding data acquisition (e.g. enhanced occlusion, taller trees) and should be researched further. The work of Disney et al. (2014) presents preliminary results of using QSMs for biomass estimation in tropical forests in Gabon.

**4. How well do crown archetypes represent true crown architecture when inferring broad-scale forest structure?**

The answers to the previous three research questions provide methods of analysing terrestrial LiDAR data to infer forest structural measures, such as the vertical distribution of plant area index at a plot level scales, as well as the above-ground biomass, height and diameter of individual trees. These inferred measures reduce uncertainties in reference data and support the calibration and validation of large scale remote sensing products. The fourth research question looks at the potential of 3D data as input for realistic scene models to simulate real airborne or satellite data through radiative transfer modelling. The focus in chapter 5 is on simulating large footprint air/spaceborne LiDAR over virtual scene models, but this work can easily be transferred to simulating optical sensors in the future.

Many LiDAR studies assumed crown archetypes (table 5.1) for estimating vegetation parameters from LiDAR signals. Such crown archetypes are typically assumed to contain a turbid medium to account for within-crown scattering. A new set of analytical expressions for modelling LiDAR returns is developed in chapter 5. These expressions are used to test the impact of assumptions made concerning crown archetypes when inferring structural information from large footprint LiDAR. Highly detailed 3D models are used and LiDAR waveforms are simulated using the *librat* radiative transfer model. The use of 3D computer generated tree models allows us to control all aspects of the environment and sensors, and provide a straightforward means to calculate reference values. The retrieval of leaf area index (LAI, as a proxy for forest structure) is evaluated through inversion of the analytical expressions. Seemingly rational values of LAI are inferred due to coupling of parameters. The absolute predication error typically ranges from 39 to 79%, but is in some cases as high as 261%.

Terrestrial LiDAR provides us with very detailed 3D data. These data have large potential as input for realistic scene models, using explicit models that are not dependent on crown archetype assumption. They provide information not only about the individual trees, but also concerning the woody and herbaceous understorey and the interaction between all these vegetation components. Furthermore, it provides a very detailed terrain model, which is of importance for simulating satellite data (Hancock et al., 2012; Schaaf et al., 1994).

## 6.2 Reflection and outlook

This research is motivated by the need for more objective, robust and rapid assessment of forest structure that can assist in the calibration and validation of large scale remote sensing products. Within that context, this thesis shows that highly detailed 3D measurements derived from terrestrial LDAR have great potential for forest monitoring. This work contributes scientifically to the development and testing of new methods and explores their practical use. The latter is of importance, in particular for Measurement, Reporting and Verification (MRV) systems for REDD+. REDD+ is a climate change mitigation solution that is developed and supported by initiatives such as The United Nations Collaborative Programme on Reducing Emissions from Deforestation and Forest Degradation (UN-REDD) (United Nations, 2014). Terrestrial LiDAR can play an important role in reducing uncertainties in forest inventory data. Although it is not a wall-to-wall technique that can provide a national forest inventory, it offers great opportunities for consistent data collection.

This thesis provides a true validation of TLS inferred DBH, tree height and AGB against destructive harvesting and compares these estimates with measures from traditional forest inventory data. Furthermore, I improve the methods for generating vertical plant profiles by applying a topography correction and test this in multiple forest types. The robustness of such vertical plant profiles and how they can assist with monitoring seasonal vegetation dynamics is demonstrated. The remainder of this chapter reflects on some of the issues and limitations of terrestrial LiDAR and discusses future developments.

### 6.2.1 LiDAR intensity information

The methods developed in this thesis use only the explicit spatial component (i.e. x, y and z values) of the TLS data. The intensity information, which indicates the strength of each LiDAR return, or the shape of the returned waveform (see section 6.2.2) is not used. Inclusion of such additional spectral information may further improve the current methods presented in this thesis.

The vertical plant profiles that are generated within the framework of this thesis (chapter 2 and 3) use multiple return TLS data to estimate $P_{gap}$. The method assumes that each return for a specific outgoing pulse equates to a beam area interception of $1/n_s$, where $n_s$ is the number of returns for that outgoing laser pulse (equation 2.1). The use of additional intensity information may further improve the estimation of intercepted beam area for each return. Ramirez et al. (2013) used intensity information to improve $P_{gap}$ from a first return TLS instrument. The use of a similar approach for a multiple return instrument will be more complex because the intercepted laser energy from previous returns has to be accounted for.

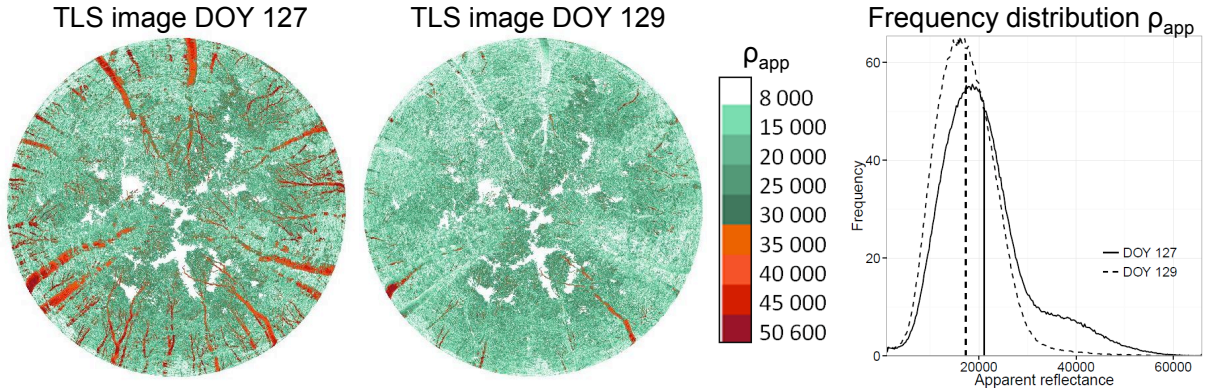


**Figure 6.1:** Effect of moisture on terrestrial LiDAR data captured with the RIEGL VZ-400 (wavelength 1550 nm). The data on DOY 127 was captured in dry weather, the data on DOY 129 was captured after rain when canopy constituents were still wet. The data was captured in Dassenbos, location C (see chapter 3 for details). The TLS data is visualised in a polar projection and is coloured according to apparent reflectance $\rho_{app}$. Jupp et al. (2009) defined $\rho_{app}$ as the reflectance of a diffuse target filling the laser beam that would return the same amount of intensity as the actual target. The right panel shows the frequency distribution of the two images, with the vertical lines indicating the statistical mean $\rho_{app}$.

The RIEGL VZ-400 terrestrial laser scanner is used for the data acquisition in this thesis and operates in the infrared at a wavelength of 1550 nm. Other commercial and scientific TLS instruments operate in a similar wavelength. For example, the Leica HDS7000 and Trimble TX8 operate at 1500 nm (Leica Geosystems, 2014; Trimble, 2014), the Optech ILRIS uses a wavelength of 1535 nm (Optech, 2014) and the FARO Focus$^{3D}$ X 330 operates at 1550 nm (FARO, 2014). The Salford Advanced Laser Canopy Analyser (SALCA, Danson et al. (2014); Gaulton et al. (2013)) and Dual-Wavelength Echidna Lidar (DWEL, Douglas et al. (2012)) are two recently developed scientific dual-wavelength instruments and both have one wavelength operating at approximately 1550 nm. This is near the end of the water absorption band around 1450 nm (Jensen, 2007) and this may have implications when scanning wet vegetation. Figure 6.1 shows TLS data that is captured at the same scan location in Dassenbos (chapter 3) under dry conditions (DOY 127) and wet conditions (DOY 129, after a rain event when the canopy was still wet). The frequency distribution diagrams shows that $\rho_{app}$ is systematically lower for the scan in wet conditions compared to the scan in dry conditions. This is of importance and weather conditions will have to be taken into account when using the returned intensity values in future applications.

### 6.2.2 LiDAR waveforms and the separation of woody and non-woody canopy components

It is not only intensity information that can enrich point cloud data; attributes derived from the returned waveform can also provide additional information about the intercepted canopy constituent. In this thesis a RIEGL VZ-400 laser scanner is used, which collects multiple returns and additional waveforms for returns that deviate (above a certain threshold) from the system waveform shape. The RIEGL VZ-400 is not a full-waveform scanner such as the Echidna® Validation Instrument (EVI, Strahler et al. (2008)), and as such only records samples (i.e. sampling blocks) of the returned waveform (Ullrich & Pfennigbauer, 2011). Figure 6.2 shows an example of a recorded RIEGL waveform with two discrete returns, each sampled by a sampling block of 2 ns (approximately 60 cm) (RIEGL, 2014). The previous section 6.2.1 discusses how additional intensity information can improve estimates of $P_{gap}$. It is hypothesised that waveform attributes such as width, amplitude (i.e. the intensity peak) and the energy distribution within the waveform will further improve these $P_{gap}$ estimates (Jupp et al., 2009).

TLS data is used to estimate AGB through quantitative structure models of LiDAR point clouds in chapter 4, and yields a 9.7% AGB overestimation. One of the potential error sources is identified as the geometric structure of cylinders versus the true leaf shape. A prior segmentation of the TLS point cloud in a woody and non-woody component may further improve AGB estimates. Chapter 5 suggests that estimating vegetation parameters on a larger scale using crown archetypes and radiative transfer modelling may be problematic when within-crown clumping is not accounted for. More explicit, realistic tree models could be generated from TLS data when intensity and waveform information

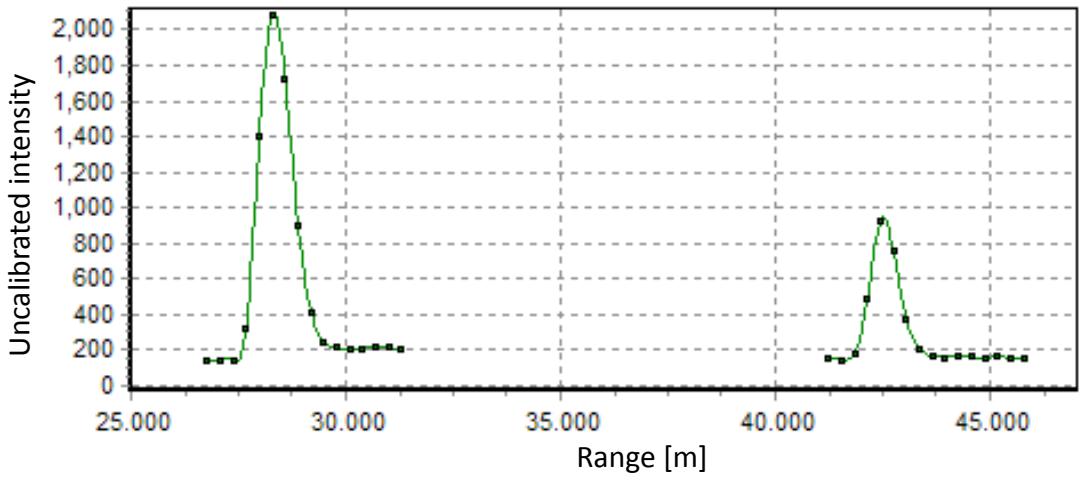


**Figure 6.2:** Example of a waveform recorded with the RIEGL VZ-400 in the RUSH07 study area (section 4.2.1). A single outgoing pulse recorded two returns: the first return was recorded at approximately 28.5 m and the second return at approximately 42.5 m.

is accounted for. Côté et al. (2009) presented an approach to reconstruct the 3D tree architecture which was a realistic representation with respect to structural attributes and their reflected and transmitted light signature (Côté et al., 2011). An intensity threshold was used to divide the point cloud into two subsets; foliage and woody components. The wood point cloud was then used to build the main branching structure and the foliage point cloud was used as attractor to grow the fine branches. The addition of leaves was based on light availability, derived from a light transition model. The intensity thresholds in this approach were chosen manually and it was difficult to infer typical values (Côté et al., 2009). Newnham et al. (2012b) used a Bayesian classification method to distinguish between different vegetation components. However, as discussed earlier in section 6.2.1, using a probabilistic framework or finding arbitrary thresholds will be more complex in multiple return TLS data because the intercepted laser energy from previous returns has to be accounted for.

Responses from canopy elements can be generalised into two categories: "hard targets" and "soft targets". "Hard targets" produce a waveform similar to the outgoing pulse (e.g. trunks), whereas "soft targets" are generated when the laser beam intersects a dispersed canopy constituent that is smaller than the beam cross-section (e.g. leaves in tree crowns) (Jupp et al., 2009). The differences in waveform characteristics are invaluable for separating woody components and foliage, which is one of the key areas for future work in terrestrial laser scanning.

Recent developments in full-waveform dual-wavelength scanners show great potential for separating woody and non-woody components. Using intensity information from a single wavelength scanner limits this separation because intensity is a function of the reflectance properties of the canopy constituents, the area of the beam that is intercepted and the local angle of incidence (Danson et al., 2014). The dual-wavelength scanners SALCA and DWEL try to overcome the limitations of a single-wavelength scanner by taking the spectral ratio of the two laser wavelengths at approximately 1064 and 1550 nm (Danson et al., 2014; Douglas et al., 2012; Hancock et al., 2012). However, it is important to acknowledge that both dual-wavelength scanners are currently research instruments that are being tested in field-based experiments and, unlike available commercial scanners, are not yet ready for deployment at large fieldwork campaigns or for operational use (Danson et al., 2014).

### 6.2.3 Forest monitoring

#### Forest degradation

This thesis demonstrates that TLS is an excellent tool for monitoring forests. However, one key area of future work is the extrapolation of these tree or plot based measures

to characterise change events and related emissions occurring over larger areas in the tropics due to forest degradation. Forest degradation refers to the loss of carbon stocks in forests, without reducing the forest cover below 10-30%. However, it represents at least 20 percent of forest carbon emissions and can act as a catalyst for deforestation (Griscom et al., 2009).

Terrestrial laser scanning offers opportunities for a consistent and robust framework to support REDD+ monitoring capacities in developing countries. Limited research has been carried out in these countries to reduce the uncertainty of emission estimates of forest degradation activities, such as selective logging. Improving emission estimates relating to forest change requires better biomass estimates before and after change events at local levels (Hill et al., 2013). Pre- and post-harvest TLS data will not only provide information about the harvested trees and related change, but it also quantifies the collateral damage caused by the harvesting activity. Chapter 4 presents a semi-automated method for improved AGB estimates using terrestrial LiDAR data. Further improvements towards a fully automated tree extraction method and objective parameter setting are essential for applying these methods in more challenging and complex biomes, such as tropical rainforests.

### Spatial variance

I have not addressed the issue of spatial variance in this work, but it is important for upscaling variables inferred from a single scan sample location to plot level and from plot level to regional level.

There is no consensus on classification schemes for many vegetation types, especially those in the tropics (Torello-Raventos et al., 2013). Vertical plant profiles are an excellent tool to assess the spatial variance in forest structure and may potentially guide us towards more robust and objective forest classification. The method of deriving vertical plant profiles does not require the registration of multiple scans and each scan location can be treated as a single sample. Further research is needed to assess the minimum number of scan locations and minimum plot size that is needed to account for this spatial variance. It is expected that spatial variance will be larger for more complex forest structures, such as an old-growth forest with a large species diversity compared to mono-dominant forests. This is important when determining the minimum plot size for ground-based assessment of AGB. Statistical errors in AGB estimates are related to the sampling uncertainty, which is related to the plot size (Chave et al., 2004; Clark & Clark, 2000). Uncertainty in plot level AGB estimates will increase when the plot size is too small, because methodological errors at tree level become more pronounced on this smaller scale. AGB is also not normally distributed among smaller plots since rare large trees contribute a large fraction of the overall AGB (Chave et al., 2004).

### 6.2.4 Outlook

This thesis demonstrates the potential use of 3D terrestrial LiDAR measurements in both a research and operational context for the monitoring of forests. In this thesis, methods are developed to analyse terrestrial LiDAR data to infer the vertical distribution of PAI and PAVD at plot level scales, as well as the above-ground biomass, height and diameter of individual trees. These TLS inferred metrics reduce uncertainties in reference data. Further testing of these methods in densely (tropical) forested environments is required in order to assess their true operational value, for example for REDD+ monitoring systems.

Data availability of terrestrial LiDAR is expected to increase over the next years. This will not only hold challenges, such as data and instrument intercomparison (Newnham et al., 2012a; Armston et al., 2013b), but also offer new opportunities. Plots may be revisited more frequently and an increased data availability will enable us to, inter alia, better study and compare similar forest types in different biomes. Chapter 3 demonstrates that terrestrial laser scanning is an excellent tool to study phenology, but insight in the effect of climate change on phenology can only be acquired by consistent and frequent data collection over a number of years. Optical remote sensing techniques have successfully been used to acquire long-term observations and monitor shifts in phenology (White et al., 2009), but such 2D data will greatly benefit from information inferred from terrestrial LiDAR data. Optical satellite data are unable to differentiate between under- and overstorey effects that influence phenology and the start of the growing season. An increase in TLS data should therefore not only focus on the spatial domain, but should also focus on better understanding the dynamics in multi-layered ecosystems.

Vegetation scatters radiation (i.e. energy emitted by the sun) anisotropically due to its 3D structure, which influences the spectral reflectance recorded with optical satellites. Little is known about how forest structure affects the anisotropy, described by the Bidirectional Reflectance Distribution Function (BRDF). Studies that relate the parameters and shape of the BRDF to vegetation structure are currently limited or non-existent, mainly due to inefficient understanding of the model parameters of the BRDF. Chapter 5 explores the potential of 3D data as input for realistic scene models to simulate real airborne or satellite data through radiative transfer modelling. The use of TLS to improve the understanding, calibration and validation of large scale optical remote sensing products is therefore a key area of future work.

Large footprint LiDAR sensors such as GLAS onboard ICEsat or LVIS can provide 3D information seen from above the canopy and allow 3D information to be used at large scale. A new large footprint spaceborne instrument, GEDI (Global Ecosystem Dynamics Investigation) LiDAR, is currently being developed and is scheduled for completion in 2018 (NASA, 2014). GEDI will sample forest structure between 50 degrees north and

50 degrees south latitudes, covering most of the tropical and temperate forests. The combination of detailed 3D forest stand models based on TLS data and radiative transfer models will provide a framework for testing the structural metrics derived from such large footprint sensors.

# References


Airborne Research Australia (2012). Airborne LiDAR 2012, version 1.0. Flinders University. Obtained from http://tern-auscover.science.uq.edu.au/thredds/catalog.html, made available by the AusCover facility (http://www.auscover.org.au) of the Terrestrial Ecosystem Research Network (TERN, http://www.tern.org.au). Accessed [07-05-2013].

Antonarakis, A. S. (2011). Evaluating forest biometrics obtained from ground lidar in complex riparian forests. *Remote Sensing Letters*, *2*, 61–70.

Armston, J., Disney, M., Lewis, P., Scarth, P., Phinn, S., Lucas, R., Bunting, P., & Goodwin, N. (2013a). Direct retrieval of canopy gap probability using airborne waveform lidar. *Remote Sensing of Environment*, *134*, 24–38.

Armston, J., Newnham, G., Strahler, A. H., Schaaf, C., Danson, M., Gaulton, R., Zhang, Z., Disney, M., Sparrow, B., Phinn, S. R., Schaefer, M., Burt, A., Counter, S., Erb, A., Goodwin, N. et al. (2013b). Intercomparison of terrestrial laser scanning instruments for assessing forested ecosystems: A brisbane field experiment. In *AGU fall meeting, 3-19 Dec. 2013, San Fransico, USA*.

Ashcroft, M. B., Gollan, J. R., & Ramp, D. (2014). Creating vegetation density profiles for a diverse range of ecological habitats using terrestrial laser scanning. *Methods in Ecology and Evolution*, *5*, 263–272.

Asner, G. P., Mascaro, J., Anderson, C., Knapp, D. E., Martin, R. E., Kennedy-Bowdoin, T., van Breugel, M., Davies, S., Hall, J. S., Muller-Landau, H. C., Potvin, C., Sousa, W., Wright, J., & Bermingham, E. (2013). High-fidelity national carbon mapping for resource management and redd+. *Carbon Balance and Management*, *8*, 7.

Avitabile, V., Baccini, A., Friedl, M. A., & Schmullius, C. (2012). Capabilities and limitations of Landsat and land cover data for aboveground woody biomass estimation of Uganda. *Remote Sensing of Environment*, *117*, 366–380.

Baccini, A., Goetz, S. J., Walker, W. S., Laporte, N. T., Sun, M., Sulla-Menashe, D., Hackler, J., Beck, P. S. A., Dubayah, R., Friedl, M. A., Samanta, S., & Houghton, R. A. (2012). Estimated carbon dioxide emissions from tropical deforestation improved by carbon-density maps. *Nature Climate Change*, *2*, 182–185.

Balduzzi, M. A. F., van der Zande, D., Stuckens, J., Verstraeten, W. W., & Coppin, P.

(2011). The properties of terrestrial laser system intensity for measuring leaf geometries: A case study with conference pear trees (pyrus communis). *Sensors*, *11*, 1657–1681.

Barbier, N., Proisy, C., Véga, C., Sabatier, D., & Couteron, P. (2011). Bidirectional texture function of high resolution optical images of tropical forest: An approach using LiDAR hillshade simulations. *Remote Sensing of Environment*, *115*, 167–179.

Bates, D. M., & Watts, D. G. (1988). *Nonlinear Regression Analysis and Its Applications*. New York: John Wiley & Sons. 365p.

Bequet, R., Campioli, M., Kint, V., Vansteenkiste, D., Muys, B., & Ceulemans, R. (2011). Leaf area index development in temperate oak and beech forests is driven by stand characteristics and weather conditions. *Trees - Structure and Function*, *25*, 935–946.

Bi, H., Turner, J., & Lambert, M. J. (2004). Additive biomass equations for native eucalypt forest trees of temperate australia. *Trees - Structure and Function*, *18*, 467–479.

Blair, J. B., & Hofton, M. A. (1999). Modeling laser altimeter return waveforms over complex vegetation using high-resolution elevation data. *Geophysical Research Letters*, *26*, 2509–2512.

Botta, A., Viovy, N., Ciais, P., Friedlingstein, P., & Monfray, P. (2000). A global prognostic scheme of leaf onset using satellite data. *Global Change Biology*, *6*, 709–725.

Boudon, F., Preuksakarn, C., Ferraro, P., Diener, J., Nacry, P., Nikinmaa, E., & Godin, C. (2014). Quantitative assessment of automatic reconstructions of branching systems obtained from laser scanning. *Annals of Botany*, . Doi:10.1093/aob/mcu062.

Brown, S., Gillespie, A. J. R., & Lugo, A. E. (1989). Biomass estimation methods for tropical forests with applications to forest inventory data. *Forest Science*, *35*, 881–902.

Bunting, P., Armston, J., Clewley, D., & Lucas, R. M. (2013a). Sorted pulse data (SPD) library. Part II: A processing framework for lidar data from pulsed laser systems in terrestrial environments. *Computers and Geosciences*, *56*, 207–215.

Bunting, P., Armston, J., Lucas, R. M., & Clewley, D. (2013b). Sorted pulse data (SPD) library. Part I: A generic file format for lidar data from pulsed laser systems in terrestrial environments. *Computers and Geosciences*, *56*, 197–206.

Burt, A., Disney, M. I., Raumonen, P., Armston, J., Calders, K., & Lewis, P. (2013). Rapid characterisation of forest structure from TLS and 3D modelling. In *IEEE International Geoscience and Remote Sensing Symposium (IGARSS)*. pp. 3387-3390.

Calders, K., Armston, J., Newnham, G., Herold, M., & Goodwin, N. (2014). Implications of sensor configuration and topography on vertical plant profiles derived from terrestrial lidar. *Agricultural and Forest Meteorology*, *194*, 104–117.

Calders, K., Lewis, P., Disney, M., Verbesselt, J., Armston, J., & Herold, M. (2012). Effects of clumping on modelling lidar waveforms in forest canopies. In *IEEE International Geoscience and Remote Sensing Symposium (IGARSS)*. pp. 3391-3394.

Calders, K., Lewis, P., Disney, M., Verbesselt, J., & Herold, M. (2013a). Investigating assumptions of crown archetypes for modelling lidar returns. *Remote Sensing of Environment*, *134*, 39–49.

Calders, K., Newnham, G., Herold, M., Murphy, S., Culvenor, D., Raumonen, P., Burt, A., Armston, J., Avitabile, V., & Disney, M. (2013b). Estimating above ground biomass from terrestrial laser scanning in Australian Eucalypt Open Forest. In *SilviLaser 2013, 9-11 Oct. 2013, Beijing, China*. pp. 90-97.

Calders, K., Verbesselt, J., Bartholomeus, H., & Herold, M. (2011). Applying terrestrial lidar to derive gap fraction distribution time series during bud break. In *SilviLaser 2011, 16-20 Oct. 2011, Hobart, Australia*.

Chave, J., Andalo, C., Brown, S., Cairns, M. A., Chambers, J. Q., Eamus, D., Folster, H., Fromard, F., Higuchi, N., Kira, T., Lescure, J.-P., Nelson, B. W., Ogawa, H., Puig, H., Riera, B. et al. (2005). Tree allometry and improved estimation of carbon stocks and balance in tropical forests. *Oecologia*, *145*, 87–99.

Chave, J., Condit, R., Aguilar, S., Hernandez, A., Lao, S., & Perez, R. (2004). Error propagation and scaling for tropical forest biomass estimates. *Philosophical Transactions of the Royal Society of London. Series B: Biological Sciences*, *359*, 409–420.

Chave, J., Réjou-Méchain, M., Búrquez, A., Chidumayo, E., Colgan, M. S., Delitti, W. B. C., Duque, A., Eid, T., Fearnside, P. M., Goodman, R. C., Henry, M., Martínez-Yrízar, A., Mugasha, W. A., Muller-Landau, H. C., Mencuccini, M. et al. (2014). Improved allometric models to estimate the aboveground biomass of tropical trees. *Global Change Biology*, . DOI: 10.1111/gcb.12629.

Che, M., Chen, B., Zhang, H., Fang, S., Xu, G., Lin, X., & Wang, Y. (2014). A New Equation for Deriving Vegetation Phenophase from Time Series of Leaf Area Index (LAI) Data. *Remote Sensing*, *6*, 5650–5670.

Chiang, J.-M., & Brown, K. J. (2007). Improving the budburst phenology subroutine in the forest carbon model PnET. *Ecological Modelling*, *205*, 515–526.

Chmielewski, F.-M., & Rotzer, T. (2001). Response of tree phenology to climate change across europe. *Agricultural and Forest Meteorology*, *108*, 101–112.

Clark, D. B., & Clark, D. A. (2000). Landscape-scale variation in forest structure and biomass in a tropical rain forest. *Forest Ecology and Management*, *137*, 185–198.

Côté, J.-F., Fournier, R. A., & Egli, R. (2011). An architectural model of trees to estimate forest structural attributes using terrestrial lidar. *Environmental Modelling and Software*, *26*, 761–777.

Côté, J.-F., Fournier, R. A., Frazer, G. W., & Niemann, K. O. (2012). A fine-scale architectural model of trees to enhance lidar-derived measurements of forest canopy structure. *Agricultural and Forest Meteorology*, *166-167*, 72–85.

Côté, J.-F., Widlowski, J.-L., Fournier, R. A., & Verstraete, M. M. (2009). The structural and radiative consistency of three-dimensional tree reconstructions from terrestrial lidar. *Remote Sensing of Environment*, *113*, 1067–1081.

Cushman, K. C., Muller-Landau, H. C., Condit, R. S., & Hubbell, S. P. (2014). Improving estimates of biomass change in buttressed trees using tree taper models. *Methods in Ecology and Evolution*, .

Danson, F. M., Gaulton, R., Armitage, R. P., Disney, M., Gunawan, O., Lewis, P., Pearson, G., & Ramirez, F. A. (2014). Developing a dual-wavelength full-waveform terrestrial laser scanner to characterize forest canopy structure. *Agricultural and Forest Meteorology*, *198-199*, 7–14.

Danson, F. M., Hetherington, D., Morsdorf, F., Koetz, B., & Allgöwer, B. (2007). Forest canopy gap fraction from terrestrial laser scanning. *IEEE Geoscience and Remote Sensing Letters*, *4*, 157–160.

Dantec, C. F., Vitasse, Y., Bonhomme, M., Louvet, J.-M., Kremer, A., & Delzon, S. (2014). Chilling and heat requirements for leaf unfolding in european beech and sessile oak populations at the southern limit of their distribution range. *International Journal of Biometeorology*, (pp. 1–12).

Dassot, M., Colin, A., Santenoise, P., Fournier, M., & Constant, T. (2012). Terrestrial laser scanning for measuring the solid wood volume, including branches, of adult standing trees in the forest environment. *Computers and Electronics in Agriculture*, *89*, 86–93.

De Sy, V., Herold, M., Achard, F., Asner, G. P., Held, A., Kellndorfer, J., & Verbesselt, J. (2012). Synergies of multiple remote sensing data sources for REDD+ monitoring. *Current Opinion in Environmental Sustainability*, *4*, 696–706.

DiMiceli, C. M., Carroll, M. L., Sohlberg, R. A., Huang, C., Hansen, M. C., & Townshend, J. R. G. (2011). Annual global automated modis vegetation continuous fields (mod44b) at 250 m spatial resolution for data years beginning day 65, 2000 - 2010, collection 5 percent tree cover. University of Maryland, College Park, MD, USA.

Disney, M., Lewis, P., & Raumonen, P. (2012). Testing a new vegetation structure retrieval algorithm from terrestrial lidar scanner data using 3d models. In *SilviLaser 2012, 16-18 Sep. 2012, Vancouver, Canada*.

Disney, M., Lewis, P., & Saich, P. (2006). 3D modelling of forest canopy structure for remote sensing simulations in the optical and microwave domains. *Remote Sensing of Environment*, *100*, 114–132.

Disney, M. I., Burt, A., Calders, K., Raumonen, P., Gonzalez de Tanago, J., Cuni Sanchez, A. et al. (2014). New applications of 3D measurements and modelling to quantifying forest structure and biomass. In *Global Vegetation Modelling and Measurement (GV2M) meeting, 3-7 Feb. 2014, Avignon, France*.

Disney, M. I., Kalogirou, V., Lewis, P., Prieto-Blanco, A., Hancock, S., & Pfeifer, M. (2010). Simulating the impact of discrete-return lidar system and survey characteristics over young conifer and broadleaf forests. *Remote Sensing of Environment*, *114*, 1546–1560.

Disney, M. I., Lewis, P., Bouvet, M., Prieto-Blanco, A., & Hancock, S. (2009). Quantifying surface reflectivity for spaceborne lidar via two independent methods. *IEEE Transactions on Geoscience and Remote Sensing*, *47*, 3262–3271.

Disney, M. I., Lewis, P., & North, P. R. J. (2000). Monte carlo ray tracing in optical canopy reflectance modelling. *Remote Sensing Reviews*, *18*, 163–196.

Douglas, E. S., Strahler, A., Martel, J., Cook, T., Mendillo, C., Marshall, R., Chakrabarti, S., Schaaf, C., Woodcock, C., Zhan, L., Xiaoyuan, Y., Culvenor, D., Jupp, D., Newnham, G., & Lovell, J. (2012). DWEL: A dual-wavelength echidna lidar for ground-based forest scanning. In *IEEE International Geoscience and Remote Sensing Symposium (IGARSS)*. pp. 4998-5001.

Drake, J. B., Dubayah, R. O., Clarck, D. B., Knox, R. G., Blair, J. B., Hofton, M. A., Chazdon, R. L., Weishampel, J. F., & Prince, S. D. (2002). Estimation of tropical forest structural characteristics using large-footprint lidar. *Remote Sensing of Environment*, *79*, 305–319.

DSITIA (2012). Protecting our coastal communities: South East Queensland coastal lidar data capture. Department of Science, Information Technology, Innovation and the Arts.

España, M. L., Baret, F., & Weiss, M. (2008). Slope correction for LAI estimation from gap fraction measurements. *Agricultural and Forest Meteorology*, *148*, 1553–1562.

FAO (2010). Global forest resources assessment 2010, Main report, FAO Forestry Paper 163. 378p.

FAO, JRC, SDSU, & UCL (2009). The 2010 global forest resources assessment remote sensing survey: an outline of the objectives, data, methods and approach. forest resources assessment working paper 155. Published by FAO with FRA RSS partners, Rome, 16p.

FARO (2014). FARO Laser Scanner Focus$^{3D}$ X 330 Technical Sheet. Available on www.faro.com, [date of visit: 24/08/2014].

Ferraz, A., Bretar, F., Jacquemoud, S., Gonçalves, G., Pereira, L., Tomé, M., & Soares, P. (2012). 3-D mapping of a multi-layered mediterranean forest using ALS data. *Remote Sensing of Environment*, *121*, 210–223.

Flood, M. (2004). ASPRS guidelines: Vertical accuracy reporting for lidar data. ASPRS.

Fu, Y. H., Campioli, M., Deckmyn, G., & Janssens, I. A. (2012). The impact of winter and spring temperatures on temperate tree budburst dates: Results from an experimental climate manipulation. *PLoS ONE*, *7*. E47324.

Garrity, S. R., Bohrer, G., Maurer, K. D., Mueller, K. L., Vogel, C. S., & Curtis, P. S. (2011). A comparison of multiple phenology data sources for estimating seasonal transitions in deciduous forest carbon exchange. *Agricultural and Forest Meteorology*, *151*, 1741–1752.

Gaulton, R., Danson, F., Ramirez, F., & Gunawan, O. (2013). The potential of dual-wavelength laser scanning for estimating vegetation moisture content. *Remote Sensing of Environment*, *132*, 32–39.

GDAL Development Team (2012). *GDAL - Geospatial Data Abstraction Library, Version 1.9.2*. Open Source Geospatial Foundation.

Goetz, S., Steinberg, D., Dubayah, R., & Blair, B. (2007). Laser remote sensing of canopy habitat heterogeneity as a predictor of bird species richness in an eastern temperate forest, USA. *Remote Sensing of Environment*, *108*, 254–263.

Gomes Pereira, L., & Gonçalves, G. (2010). Accuracy of a DTM derived from full-waveform laser scanning data under unstructured eucalypt forest: A case study. In *XXIV FIG International Congress*.

Gond, V., De Pury, D. G. G., Veroustraete, F., & Ceulemans, R. (1999). Seasonal variations in leaf area index, leaf chlorophyll, and water content; scaling-up to estimate fapar and carbon balance in a multilayer, multispecies temperate forest. *Tree Physiology*, *19*, 673–679.

Goodwin, N. R., Coops, N. C., & Culvenor, D. S. (2007). Development of a simulation model to predict LiDAR interception in forested environments. *Remote Sensing of Environment*, *111*, 481–492.

Griscom, B., Ganz, D., Virgilio, N., Price, F., Hayward, J., Cortez, R., Dodge, G., Hurd, J., Lowenstein, F. L., & Stanley, B. (2009). The hidden frontier of forest degradation: A review of the science, policy and practice of reducing degradation emissions. The Nature Conservancy, Arlington, VA. 76p.

Hamunyela, E., Verbesselt, J., Roerink, G., & Herold, M. (2013). Trends in spring phenology of western european deciduous forests. *Remote Sensing*, *5*, 6159–6179.

Hancock, S. (2010). *Understanding the measurement of forests with waveform lidar*. Ph.D. thesis University College London.

Hancock, S., Disney, M., Muller, J.-P., Lewis, P., & Foster, M. (2011). A threshold insensitive method for locating the forest canopy top with waveform lidar. *Remote Sensing of Environment*, *115*, 3286–3297.

Hancock, S., Essery, R., Reid, T., Carle, J., Baxter, R., Rutter, N., & Huntley, B. (2014). Characterising forest gap fraction with terrestrial lidar and photography: An examination of relative limitations. *Agricultural and Forest Meteorology*, *189-190*, 105–114.

Hancock, S., Lewis, P., Foster, M., Disney, M., & Muller, J.-P. (2012). Measuring forests with dual wavelength lidar: A simulation study over topography. *Agricultural and Forest Meteorology*, *161*, 123–133.

Hansen, M. C., DeFries, R. S., Townshend, J. R. G., Carroll, M., Dimiceli, C., & Sohlberg, R. A. (2003). Global percent tree cover at a spatial resolution of 500 meters: First results of the modis vegetation continuous fields algorithm. *Earth Interactions*, *7*, 1–15.

Hansen, M. C., Potapov, P. V., Moore, R., Hancher, M., Turubanova, S. A., Tyukavina, A., Thau, D., Stehman, S. V., Goetz, S. J., Loveland, T. R., Kommareddy, A., Egorov, A., Chini, L., Justice, C. O., & Townshend, J. R. G. (2013). High-resolution global maps of 21st-century forest cover change. *Science*, *342*, 850–853.

Herold, M., Román-Cuesta, R. M., Heymell, V., Hirata, Y., Van Laake, P., Asner, G., Souza, C., Avitabile, V., & MacDicken, K. (2011). A review of methods to measure and monitor historical carbon emissions from forest degradation. *Unasylva*, *62*, 16–24.

Herold, M., & Skutsch, M. (2011). Monitoring, reporting and verification for national REDD+ programmes: two proposals. *Environmental Research Letters*, *6*, 014002.

Hilker, T., Coops, N. C., Culvenor, D. S., Newnham, G., Wulder, M. A., Bater, C. W., & Siggins, A. (2012). A simple technique for co-registration of terrestrial LiDAR observations for forestry applications. *Remote Sensing Letters*, *3*, 239–247.

Hill, T. C., Williams, M., Bloom, A. A., Mitchard, E. T. A., & Ryan, C. M. (2013). Are inventory based and remotely sensed above-ground biomass estimates consistent? *PLoS ONE*, *8*, e74170.

Holmes, R. T., & Sherry, T. W. (2001). Thirty-year bird population trends in an unfragmented temperate deciduous forest: importance of habitat change. *The Auk*, *118*, 589–609.

Hopkinson, C., Chasmer, L., Young-Pow, C., & Treitz, P. (2004). Assessing forest metrics with a ground-based scanning lidar. *Canadian Journal of Forest Research*, *34*, 573–583.

Hosoi, F., Nakai, Y., & Omasa, K. (2013). 3-D voxel-based solid modeling of a broad-leaved tree for accurate volume estimation using portable scanning lidar. *ISPRS Journal of Photogrammetry and Remote Sensing*, *82*, 41–48.

Houghton, R., Hall, F., & Goetz, S. (2009). Importance of biomass in the global carbon cycle. *Journal of Geophysical Research: Biogeosciences*, *114*, G00E03.

Hyde, P., Dubayah, R., Peterson, B., Blair, J. B., Hofton, M., Hunsaker, C., Knox, R., & Walker, W. (2005). Mapping forest structure for wildlife habitat analysis using waveform lidar: Validation of montane ecosystems. *Remote Sensing of Environment*,

*96*, 427–437.

Jensen, J. R. (2007). *Remote Sensing of the Environment: An Earth Resource Perspective, Second Edition*. Prentice Hall. 608p.

Jeong, S.-J., Medvigy, D., Shevliakova, E., & Malyshev, S. (2012). Uncertainties in terrestrial carbon budgets related to spring phenology. *Journal of Geophysical Research, G: Biogeosciences*, *117*. http://dx.doi.org/10.1029/2011jg001868.

Jonckheere, I., Fleck, S., Nackaerts, K., Muys, B., Coppin, P., Weiss, M., & Baret, F. (2004). Review of methods for in situ leaf area index determination part i. theories, sensors and hemispherical photography. *Agricultural and Forest Meteorology*, *121*, 19–35.

Jupp, D. L. B., Culvenor, D. S., Lovell, J. L., Newnham, G. J., Strahler, A. H., & Woodcock, C. E. (2009). Estimating forest lai profiles and structural parameters using a ground-based laser called echidna®. *Tree physiology*, *29*, 171–181.

Jupp, D. L. B., & Lovell, J. L. (2007). Airborne and ground-based lidar systems for forest measurement: background and principles. *CSIRO Marine and Atmospheric Research paper 17*, (p. 151 p.).

Kaasalainen, S., Krooks, A., Liski, J., Raumonen, P., Kaartinen, H., Kaasalainen, M., Puttonen, E., Anttila, K., & Mäkipää, R. (2014). Change detection of tree biomass with terrestrial laser scanning and quantitative structure modelling. *Remote Sensing*, *6*, 3906–3922.

Kato, A., Moskal, L. M., Schiess, P., Swanson, M. E., Calhoun, D., & Stuetzle, W. (2009). Capturing tree crown formation through implicit surface reconstruction using airborne lidar data. *Remote Sensing of Environment*, *113*, 1148–1162.

Kearsley, E., De Haulleville, T., Hufkens, K., Kidimbu, A., Toirambe, B., Baert, G., Huygens, D., Kebede, Y., Defourny, P., Bogaert, J., Beeckman, H., Steppe, K., Boeckx, P., & Verbeeck, H. (2013). Conventional tree height-diameter relationships significantly overestimate aboveground carbon stocks in the central congo basin. *Nature Communications*, . DOI: 10.1038/ncomms3269.

Koch, B., Heyder, U., & Weinacker, H. (2006). Detection of individual tree crowns in airborne lidar data. *Photogrammetric Engineering and Remote Sensing*, *72*, 357–363.

Koetz, B., Sun, G., Morsdorf, F., Ranson, K. J., Kneubühler, M., Itten, K., & Allgöwer, B. (2007). Fusion of imaging spectrometer and LIDAR data over combined radiative transfer models for forest canopy characterization. *Remote Sensing of Environment*, *106*, 449–459.

Kotchenova, S. Y., Shabanov, N. V., Knyazikhin, Y., Davis, A. B., Dubayah, R., & Myneni, R. B. (2003). Modeling lidar waveforms with time-dependent stochastic radiative transfer theory for remote estimations of forest structure. *Journal of Geophysical*

*Research*, *108*(D15), 4484.

Leersnijder, R. P. (1992). Pinogram: a pine growth area model. *Ecological Modelling*, *61*, 1–147.

van Leeuwen, M., & Nieuwenhuis, M. (2010). Retrieval of forest structural parameters using lidar remote sensing. *European Journal of Forest Research*, *129*, 749–770.

Lefsky, M. A., Cohen, W. B., Acker, S. A., Parker, G. G., Spies, T. A., & Harding, D. (1999). Lidar remote sensing of the canopy structure and biophysical properties of douglas-fir western hemlock forests. *Remote Sensing of Environment*, *70*, 339–361.

Lefsky, M. A., Harding, D. J., Keller, M., Cohen, W. B., Carabajal, C. C., Espirito-Santo, F. D. B., Hunter, M. O., & de Oliveira Jr., R. (2005). Estimates of forest canopy height and aboveground biomass using icesat. *Geophysical Research Letters*, *32*, L22S02.

Leica Geosystems (2014). HDS7000 Data Sheet. Available on www.leica-geosystems.com, [date of visit: 24/08/2014].

Levenberg, K. (1944). A method for the solution of certain non-linear problems in least squares. *Quarterly of Applied Mathematics*, *2*, 164–168.

Lewis, P. (1999). Three-dimensional plant modelling for remote sensing simulation studies using the Botanical Plant Modelling System. *Agronomie, Agriculture and Environment*, *19*, 185–210.

Lim, K., Treitz, P., Baldwin, K., Morrison, I., & Green, J. (2003). Lidar remote sensing of biophysical properties of tolerant northern hardwood forests. *Canadian Journal of Remote Sensing*, *29*, 658–678.

Lin, L. (1989). A concordance correlation coefcient to evaluate reproducibility. *Biometrics*, *45*, 255–268.

Lovell, J. L., Haverd, V., Jupp, D. L. B., & Newnham, G. J. (2012). The Canopy Semi-analytic P gap And Radiative Transfer (CanSPART) model: Validation using ground based lidar. *Agricultural and Forest Meteorology*, *158-159*, 1–12.

Lovell, J. L., Jupp, D. L. B., Culvenor, D. S., & Coops, N. C. (2003). Using airborne and ground-based ranging lidar to measure canopy structure in Australian forests. *Canadian Journal of Remote Sensing*, *29*, 607–622.

Lovell, J. L., Jupp, D. L. B., van Gorsel, E., Jimenez-Berni, J., Hopkinson, C., & Chasmer, L. (2011a). Foliage profiles from ground based waveform and discrete point lidar. In *SilviLaser 2011, 16-20 Oct. 2011, Hobart, Australia*.

Lovell, J. L., Jupp, D. L. B., Newnham, G. J., & Culvenor, D. (2011b). Measuring tree stem diameters using intensity profiles from ground-based scanning lidar from a fixed viewpoint. *ISPRS Journal of Photogrammetry  Remote Sensing*, *66*, 46–55.

Marquardt, D. W. (1963). An algorithm for least-squares estimation of nonlinear param-

eters. *Journal of the Society for Industrial and Applied Mathematics*, *11*, 431–441.

Mitchard, E. T. A., Feldpausch, T. R., Brienen, R. J. W., Lopez-Gonzalez, G., Monteagudo, A., Baker, T. R., Lewis, S. L., Lloyd, J., Quesada, C. A., Gloor, M., ter Steege, H., Meir, P., Alvarez, E., Araujo-Murakami, A., Aragão, L. E. O. C. et al. (2014). Markedly divergent estimates of amazon forest carbon density from ground plots and satellites. *Global Ecology and Biogeography*, . DOI: 10.1111/geb.12168.

Mitchard, E. T. A., Saatchi, S. S., Baccini, A., Asner, G. P., Goetz, S. J., Harris, N. L., & Brown, S. (2013). Uncertainty in the spatial distribution of tropical forest biomass: A comparison of pan-tropical maps. *Carbon Balance and Management*, *8*, 10.

Murray, M., Cannell, M., & Smith, R. (1989). Date of budburst of fifteen tree species in britain following climatic warming. *Journal of Applied Ecology*, *26*, 693–700.

Muss, J. D., Mladenoff, D. J., & Townsend, P. A. (2011). A pseudo-waveform technique to assess forest structure using discrete lidar data. *Remote Sensing of Environment*, *115*, 824–835.

NASA (2014). Missions: GEDI. Available on http://science.nasa.gov/missions/gedi/, [date of visit: 15/09/2014].

Nelson, R. (1997). Modeling forest canopy heights: the effect of canopy shape. *Remote Sensing of Environment*, *60*, 327–334.

Newnham, G., Armston, J., Muir, J., Goodwin, N., Tindall, D., Culvenor, D., Püschel, P., Nyström, M., & Johansen, K. (2012a). Evaluation of terrestrial laser scanners for measuring vegetation structure. CSIRO Sustainable Agriculture Flagship, available on https://publications.csiro.au/rpr/pub?pid=csiro:EP124571.

Newnham, G., Goodwin, N., Armston, J., Muir, J., & Culvenor, D. (2012b). Comparing time-of-flight and phase-shift terrestrial laser scanners for characterising topography and vegetation density in a forest environment. In *SilviLaser 2012, 16-18 Sep. 2012, Vancouver, Canada*.

Ni-Meister, W., Jupp, D. L. B., & Dubayah, R. (2001). Modeling lidar waveforms in heterogeneous and discrete canopies. *IEEE transactions on geoscience and remote sensing*, *39*, 1943–1958.

Ni-Meister, W., Lee, S., Strahler, A. H., Woodcock, C. E., Schaaf, C., Yao, T., Ranson, K. J., Sun, G., & Blair, J. B. (2010). Assessing general relationships between aboveground biomass and vegetation structure parameters for improved carbon estimate from lidar remote sensing. *Journal of Geophysical Research*, *115*, G00E11.

North, P. R. J., Rosette, J. A. B., Suárez, J. C., & Los, S. O. (2010). A monte carlo radiative transfer model of satellite waveform LiDAR. *International Journal of Remote Sensing*, *31*, 1343–1358.

Optech (2014). ILRIS Terrestrial Laser Scanner Summary Specification Sheet. Available

on www.optech.com, [date of visit: 24/08/2014].

Parker, G. G., O'Neill, J. P., & Higman, D. (1989). Vertical profile and canopy organization in a mixed deciduous forest. *Vegetatio*, *85*, 1–11.

Paul, K. I., Roxburgh, S. H., England, J. R., Ritson, P., Hobbs, T., Brooksbank, K., Raison, R. J., Larmour, J. S., Murphy, S., Norris, J., Neumann, C., Lewis, T., Jonson, J., Carter, J. L., McArthur, G. et al. (2013). Development and testing of allometric equations for estimating above-ground biomass of mixed-species environmental plantings. *Forest Ecology and Management*, *310*, 483–494.

Pinty, B., Widlowski, J.-L., Taberner, M., Gobron, N., Verstraete, M. M., Disney, M., Gascon, F., Gastellu, J.-P., Jiang, L., Kuusk, A., Lewis, P., Li, X., Ni-Meister, W., Nilson, T., North, P. et al. (2004). Radiation transfer model intercomparison (RAMI) exercise: Results from the second phase. *Journal of Geophysical Research*, *109*, D06210.

Pirotti, F., Guarnieri, A., & Vettore, A. (2013). Ground filtering and vegetation mapping using multi-return terrestrial laser scanning. *ISPRS Journal of Photogrammetry Remote Sensing*, *76*, 56–63.

Polgar, C., & Primack, R. (2011). Leaf-out phenology of temperate woody plants: From trees to ecosystems. *New Phytologist*, *191*, 926–941.

Popescu, S. C., Zhao, K., Neuenschwander, A., & Lin, C. (2011). Satellite lidar vs. small footprint airborne lidar: Comparing the accuracy of aboveground biomass estimates and forest structure metrics at footprint level. *Remote Sensing of Environment*, *115*, 2786–2797.

Portillo-Quintero, C., Sanchez-Azofeifa, A., & Culvenor, D. (2014). Using VEGNET In-Situ monitoring LiDAR (IML) to capture dynamics of plant area index, structure and phenology in Aspen Parkland Forests in Alberta, Canada. *Forests*, *5*, 1053–1068.

Pueschel, P., Newnham, G., & Hill, J. (2014). Retrieval of gap fraction and effective plant area index from phase-shift terrestrial laser scans. *Remote Sensing*, *6*, 2601–2627.

R Development Core Team (2011). *R: A Language and Environment for Statistical Computing*. R Foundation for Statistical Computing Vienna, Austria. ISBN 3-900051-07-0.

Ramirez, F. A., Armitage, R. P., & Danson, F. M. (2013). Testing the application of terrestrial laser scanning to measure forest canopy gap fraction. *Remote Sensing*, *5*, 3037–3056.

Raumonen, P., Kaasalainen, M., Markku, A., Kaasalainen, S., Kaartinen, H., Vastaranta, M., Holopainen, M., Disney, M., & Lewis, P. (2013). Fast automatic precision tree models from terrestrial laser scanner data. *Remote Sensing*, *5*, 491–520.

Reitberger, J., Krzystek, P., & Stilla, U. (2008). Analysis of full waveform LIDAR data for the classification of deciduous and coniferous trees. *International Journal of Remote Sensing*, *29*, 1407–1431.

Riaño, D., Chuvieco, E., Condés, S., González-Matesanz, J., & Ustin, S. L. (2004). Generation of crown bulk density for *Pinus sylvestris* L. from lidar. *Remote Sensing of Environment*, *92*, 345–352.

Richardson, A. D., Keenan, T. F., Migliavacca, M., Ryu, Y., Sonnentag, O., & Toomey, M. (2013). Climate change, phenology, and phenological control of vegetation feedbacks to the climate system. *Agricultural and Forest Meteorology*, *169*, 156–173.

Richardson, A. D., & O'Keefe, J. (2009). Phenological differences between understory and overstory a case study using the long-term harvard forest records. chapter Phenology of Ecosystem Processes: Applications in Global Change Research. (pp. 87–117). New York: Springer.

RIEGL (2013). Datasheet RIEGL VZ-400. Available on www.riegl.com, [date of visit: 19/02/2013].

RIEGL (2014). RiWAVELib: waveform extraction library. Available on www.riegl.com, [date of visit: 24/08/2014].

ROAMES (2012). Ergon energy - remote observation automated modelling economic simulation.

Romijn, J. E., Herold, M., Kooistra, L., Murdiyarso, D., & Verchot, L. (2012). Assessing capacities of non-Annex I countries for national forest monitoring in the context of REDD+. *Environmental Science and Policy*, *19-20*, 33–48.

Ross, J. (1981). *The radiation regime and architecture of plant stands*. W. Junk Publishers, The Hague. 391p.

Rusu, R. B., & Cousins, S. (2011). 3D is here: Point Cloud Library (PCL). In *Proceedings of IEEE International Conference on Robotics and Automation (ICRA)*.

Saatchi, S. S., Harris, N. L., Brown, S., Lefsky, M., Mitchard, E. T. A., Salas, W., Zutta, B. R., Buermann, W., Lewis, S. L., Hagen, S., Petrova, S., White, L., Silman, M., & Morel, A. (2011). Benchmark map of forest carbon stocks in tropical regions across three continents. *Proceedings of the National Academy of Sciences of the United States of America*, *108*, 9899–9904.

Schaaf, C. B., Li, X., & Strahler, A. H. (1994). Topographic effects on bidirectional and hemispherical reflectances calculated with a geometric-optical canopy model. *IEEE Transactions on Geoscience and Remote Sensing*, *32*, 1186–1193.

Skowronski, N. S., Clark, K. L., Duveneck, M., & Hom, J. (2011). Three-dimensional canopy fuel loading predicted using upward and downward sensing lidar systems. *Remote Sensing of Environment*, *115*, 703–714.

Snowdon, P. (1991). A ratio estimator for bias correction in logarithmic regressions. *Canadian Journal of Forest Research*, *21*, 720–724.

Stark, S. C., Leitold, V., Wu, J. L., Hunter, M. O., de Castilho, C. V., Costa, F. R. C.,

Mcmahon, S. M., Parker, G. G., Shimabukuro, M. T., Lefsky, M. A., Keller, M., Alves, L. F., Schietti, J., Shimabukuro, Y. E., Brandão, D. O. et al. (2012). Amazon forest carbon dynamics predicted by profiles of canopy leaf area and light environment. *Ecology Letters*, *15*, 1406–1414.

Stephenson, N. L., Das, A. J., Condit, R., Russo, S. E., Baker, P. J., Beckman, N. G., Coomes, D. A., Lines, E. R., Morris, W. K., Ruger, N., Alvarez, E., Blundo, C., Bunyavejchewin, S., Chuyong, G., Davies, S. J. et al. (2014). Rate of tree carbon accumulation increases continuously with tree size. *Nature*, *507*, 90–93.

Strahler, A. H., Jupp, D. L. B., Woodcock, C. E., Schaaf, C. B., Yao, T., Zhao, F., Yang, X., Lovell, J., Culvenor, D., Newnham, G., Ni-Meister, W., & Boykin-Morris, W. (2008). Retrieval of forest structural parameters using a ground-based lidar instrument (Echidna®). *Canadian Journal of Remote Sensing*, *34*, 426–440.

Sun, G., & Ranson, K. J. (2000). Modeling lidar returns from forest canopies. *IEEE Transactions on Geoscience and Remote Sensing*, *38*, 2617–2626.

Tanaka, H. O., Yamane, S., & Itioka, T. (2010). Within-tree distribution of nest sites and foraging areas of ants on canopy trees in a tropical rainforest in borneo. *Population Ecology*, *52*, 147–157.

Tang, H., Dubayah, R., Swatantran, A., Hofton, M., Sheldon, S., Clark, D. B., & Blair, B. (2012). Retrieval of vertical lai profiles over tropical rain forests using waveform lidar at La Selva, Costa Rica. *Remote Sensing of Environment*, *124*, 242–250.

Tansey, K., Selmes, N., Anstee, A., Tate, N., & Denniss, A. (2009). Estimating tree and stand variables in a corsican pine woodland from terrestrial laser scanner data. *International Journal of Remote Sensing*, *30*, 5195–5209.

Torello-Raventos, M., Feldpausch, T. R., Veenendaal, E., Schrodt, F., Saiz, G., Domingues, T. F., Djagbletey, G., Ford, A., Kemp, J., Marimon, B. S., Hur Marimon Junior, B., Lenza, E., Ratter, J. A., Maracahipes, L., Sasaki, D. et al. (2013). On the delineation of tropical vegetation types with an emphasis on forest/savanna transitions. *Plant Ecology and Diversity*, *6*, 101–137.

Trimble (2014). Trimble TX8 Datasheet. Available on www.trimble.com, [date of visit: 24/08/2014].

Ullrich, A., & Pfennigbauer, M. (2011). Echo digitization and waveform analysis in airborne and terrestrial laser scanning. *Photogrammetric Week*, *11*, 217228.

United Nations (2014). UN-REDD Programme. Available on www.un-redd.org, [date of visit: 22/08/2014].

Vaccari, S., van Leeuwen, M., Calders, K., Coops, N. C., & Herold, M. (2013). Bias in lidar-based canopy gap fraction estimates. *Remote Sensing Letters*, *4*, 391–399.

Vauhkonen, J., Tokola, T., Maltamo, M., & Packalén, P. (2009). Applied 3D texture

features in ALS-based forest inventory. *European Journal of Forest Research*, *129*, 803–811.

Venables, W. N., & Ripley, B. D. (2002). *Modern Applied Statistics with S*. (4th ed.). New York: Springer. ISBN 0-387-95457-0.

Walther, G.-R., Post, E., Convey, P., Menzel, A., Parmesan, C., Beebee, T. J. C., Fromentin, J.-M., Hoegh-Guldberg, O., & Bairlein, F. (2002). Ecological responses to recent climate change. *Nature*, *416*, 389–395.

Wang, C., & Glenn, N. F. (2008). A linear regression method for tree canopy height estimation using airborne lidar data. *Canadian Journal of Remote Sensing*, *34*, S217–S227.

Wang, Q., & Li, P. (2013). Canopy vertical heterogeneity plays a critical role in reflectance simulation. *Agricultural and Forest Meteorology*, *169*, 111–121.

Warning, R. H., & Running, S. W. (2007). *Forest ecosystems analysis at multiple scales, Third Edition*. Elsevier. 420p.

Wehr, A., & Lohr, U. (1999). Airborne laser scanning - an introduction and overview. *ISPRS Journal of Photogrammetry  Remote Sensing*, *54*, 68–82.

White, M. A., de Beurs, K. M., Didan, K., Inouye, D. W., Richardson, A. D., Jensen, O. P., O'Keefe, J., Zhang, G., Nemani, R. R., van Leeuwen, W. J. D., Brown, J. F., de Wit, A., Schaepman, M., Lin, X., Dettinger, M. et al. (2009). Intercomparison, interpretation, and assessment of spring phenology in north america estimated from remote sensing for 1982-2006. *Global Change Biology*, *15*, 2335–2359.

Widlowski, J.-L., Pinty, B., Lopatka, M., Atzberger, C., Buzica, D., Chelle, M., Disney, M., Gastellu-Etchegorry, J. P., Gerboles, M., Gobron, N., Grau, E., Huang, H., Kallel, A., Kobayashi, H., Lewis, P. E. et al. (2013). The fourth radiation transfer model intercomparison (RAMI-IV): Proficiency testing of canopy reflectance models with ISO-13528. *Journal of Geophysical Research D: Atmospheres*, *118*, 6869–6890.

Widlowski, J.-L., Taberner, M., Pinty, B., Bruniquel-Pinel, D., Disney, M., Fernandes, R., Gastellu-Etchegorry, J. P., Gobron, N., Kuusk, A., Lavergne, T., Leblanc, S., Lewis, P. E., Martin, E., Mõttus, M., North, P. R. J. et al. (2007). Third radiation transfer model intercomparison (RAMI) exercise: Documenting progress in canopy reflectance models. *Journal of Geophysical Research*, *112*, D09111.

WMO (2011). Guide to Climatological Practices WMO-No. 100 (third edition). 117p.

Yang, X., Strahler, A. H., Schaaf, C. B., Jupp, D. L. B., Yao, T., Zhao, F., Wang, Z., Culvenor, D. S., Newnham, G. J., Lovell, J. L., Dubayah, R. O., Woodcock, C. E., & Ni-Meister, W. (2013). Three-dimensional forest reconstruction and structural parameter retrievals using a terrestrial full-waveform lidar instrument (echidna). *Remote Sensing of Environment*, *135*, 36–51.

Yao, T., Yang, X., Zhao, F., Wang, Z., Zhang, Q., Jupp, D., Lovell, J., Culvenor, D., Newnham, G., Ni-Meister, W., Schaaf, C., Woodcock, C., Wang, J., Li, X., & Strahler, A. (2011). Measuring forest structure and biomass in New England forest stands using Echidna ground-based lidar. *Remote Sensing of Environment*, *115*, 2965–2974.

Yin, X., Goudriaan, J., Lantinga, E. A., Vos, J., & Spiertz, H. J. (2003). A flexible sigmoid function of determinate growth. *Annals of Botany*, *91*, 361–371.

Van der Zande, D., Mereu, S., Nadezhdina, N., Cermak, J., Muys, B., Coppin, P., & Manes, F. (2009). 3D upscaling of transpiration from leaf to tree using ground-based LiDAR: Application on a Mediterranean Holm oak (Quercus ilex L.) tree. *Agricultural and Forest Meteorology*, *149*, 1573–1583.

Zhang, K., Chen, S.-C., Whitman, D., Shyu, M.-L., Yan, J., & Zhang, C. (2003a). A progressive morphological filter for removing nonground measurements from airborne LIDAR data. *IEEE Transactions on Geoscience and Remote Sensing*, *41*, 872–882.

Zhang, X., Friedl, M. A., Schaaf, C. B., Strahler, A. H., Hodges, J. C. F., Gao, F., Reed, B. C., & Huete, A. (2003b). Monitoring vegetation phenology using modis. *Remote Sensing of Environment*, *84*, 471–475.

Zhao, F., Strahler, A. H., Schaaf, C. L., Yao, T., Yang, X., Wang, Z., Schull, M. A., Román, M. O., Woodcock, C. E., Olofsson, P., Ni-Meister, W., Jupp, D. L. B., Lovell, J. L., Culvenor, D. S., & Newnham, G. J. (2012). Measuring gap fraction, element clumping index and LAI in Sierra Forest stands using a full-waveform ground-based lidar. *Remote Sensing of Environment*, *125*, 73–79.

Zhao, F., Yang, X., Schull, M. A., Román-Colón, M. O., Yao, T., Wang, Z., Zhang, Q., Jupp, D. L. B., Lovell, J. L., Culvenor, D. S., Newnham, G. J., Richardson, A. D., Ni-Meister, W., Schaaf, C. L., Woodcock, C. E. et al. (2011). Measuring effective leaf area index, foliage profile, and stand height in New England forest stands using a full-waveform ground-based lidar. *Remote Sensing of Environment*, *115*, 2954–2964.

Zhao, F., Yang, X., Strahler, A. H., Schaaf, C. L., Yao, T., Wang, Z., Román, M. O., Woodcock, C. E., Ni-Meister, W., Jupp, D. L. B., Lovell, J. L., Culvenor, D. S., Newnham, G. J., Tang, H., & Dubayah, R. O. (2013). A comparison of foliage profiles in the Sierra National Forest obtained with a full-waveform under-canopy EVI lidar system with the foliage profiles obtained with an airborne full-waveform LVIS lidar system. *Remote Sensing of Environment*, *136*, 330–341.

# List of publications

## Peer-reviewed journal publications

**Calders, K.**, Schenkels, T., Bartholomeus, H., Armston, J., Verbesselt, J. and Herold, M. (in review). Monitoring spring phenology with high temporal resolution terrestrial LiDAR measurements. *Agricultural and Forest Meteorology.*

Hofman, J., Bartholomeus, H., Janssen, S., **Calders, K.**, Wuyts K., Van Wittenberghe, S. and Samson, R. (in review). Application of ground-based LiDAR to improve 3D modelling of urban tree crowns and associated leaf deposition of atmospheric particulates. *Environmental Science and Technology.*

**Calders, K.**, Newnham, G., Burt, A., Murphy, S., Raumonen, P., Herold, M., Culvenor, D., Avitabile, V., Disney, M., Armston, J. and Kaasalainen, M. (2014). Nondestructive estimates of above-ground biomass using terrestrial laser scanning. *Methods in Ecology and Evolution*, DOI: 10.1111/2041-210X.12301

Hofman, J., Bartholomeus, H., **Calders, K.**, Van Wittenberghe, S., Wuyts K. and Samson, R. (2014). On the relation between tree crown morphology and particulate matter deposition on urban tree leaves; a ground-based LiDAR approach. *Atmospheric Environment, 99*, 130-139.

**Calders, K.**, Armston, J., Newnham, G., Herold, M. and Goodwin, N. (2014). Implications of sensor configuration and topography on vertical plant profiles derived from terrestrial LiDAR. *Agricultural and Forest Meteorology, 194*, 104-117.

**Calders, K.**, Lewis, P., Disney, M., Verbesselt, J. and Herold, M. (2013). Investigating assumptions of crown archetypes for modelling LiDAR returns, *Remote Sensing of Environment, 134*, 39-49.

Vaccari, S., van Leeuwen, M., **Calders, K.**, Coops, C. C. and Herold, M. (2013). Bias in lidar-based canopy gap fraction estimates. *Remote Sensing Letters 4*, 391-399.

# Other scientific publications

de Bruijn, E., **Calders, K.**, Bartholomeus, H., Bauwens, S. and Lejeune, P. (2014). Terrestrial LiDAR to Improve Efficiency of Forest Inventory: Comparison of Terrestrial LiDAR and Hand-Held Mobile LiDAR Scan Data. In *European LiDAR Mapping Forum*, 8-10 Dec. 2014, Amsterdam, The Netherlands.

Gonzalez de Tanago, J., Joseph, J., Herold, M., Goodman, R., Bartholomeus, H., Avitabile, V., Raumonen, P., **Calders, K.**, Lau Sarmiento, A. and Janovec, J. (2014). Terrestrial LiDAR and 3D tree reconstruction modeling for quantification of biomass loss and characterization of impacts of selective logging in tropical forest of Peruvian Amazon. In *ForestSAT2014*, 4-7 Nov. 2014, Riva del Garda, Italy.

Bauwens, S., Bartholomeus H., Piboule, A., **Calders, K.** and Lejeune, P. (2014). Forest inventory with Terrestrial LiDAR: what about Hand-Held Mobile LiDAR? In *ForestSAT2014*, 4-7 Nov. 2014, Riva del Garda, Italy.

Kalaitzoglou, P., **Calders, K.**, de Visser, P. H. B., Harbinson, J., van Ieperen, W., Onac, E. and Marcelis, L. F. M. (2014). Responses of growth and morphology of *Solanum lycopersicum* grown under different doses of blue light. In *Measuring the Photosynthetic phenome Symposium*, 7-9 July, 2014, Wageningen, The Netherlands.

Hamunyela, E., Verbesselt, J., Schultz, M., Penndorf, A., Frotscher, K., Herold, M., Reiche, J., De Vries, B., Dutrieux, L. and **Calders, K.** (2014). Tracking forest cover change using Landsat Rapid Eye towards S2. In *SENTINEL-2 for Science Workshop*, 20-22 May 2014, Frascati, Italy.

Avitabile V., Herold M., **Calders K.**, Lewis S., Phillips O., Newnham G., Murphy S., Aguilar-Amuchastegui N., Armston J., Asner G. P. et al. (2014). Multiple data sources for analyzing, integrating and validating biomass maps. In *EARSeL - Frontiers in Earth Observation for Land System Science*, 17-18 Mar. 2014, Berlin, Germany.

Avitabile V., Herold M., **Calders K.**, Lewis S., Phillips O., Newnham G., Murphy S., Aguilar-Amuchastegui N., Armston J., Asner G. P. et al. (2014). Integrating different data sources for validating large area biomass maps. In *ESA - Land Product Validation and Evolution*, 28-30 Jan. 2014, Frascati, Italy.

Bartholomeus, H. M., Gonzalez de Tanago, J., **Calders, K.**, Lau Sarmiento, A. and Herold, M. (2014). Acquisition of terrestrial LIDAR in tropical forest to support ecological research. In *Netherlands Annual Ecology Meeting*, 11-12 Feb. 2014, Lunteren, The Netherlands.

**Calders, K.**, Newnham, G., Herold, M., Murphy, S., Raumonen, P., Culvenor, D., Burt, A., Avitabile, V., Armston, J. and Disney, M. (2014). Non-destructive estimations of

above ground biomass using terrestrial lidar. In *Global Vegetation Monitoring and Modeling (GV2M)*, 3-7 Feb. 2014, Avignon, France.

Disney, M., Burt, A., **Calders, K.**, Raumonen, P., Gonzalez de Tanago, J., Cuni Sanchez, A., Avitabile, V., Herold, M., Armston, J., Lewis, S., Lines, E. and Lewis, P. (2014). New applications of 3D measurement and modelling for quantifying forest structure and biomass. In *Global Vegetation Monitoring and Modeling (GV2M)*, 3-7 Feb. 2014, Avignon, France.

Bartholomeus, H. and **Calders, K.** (2013). Monitoring the 'lungs of the earth'. In *2013 Yearbook of the Environmental Sciences Group : examples of research and education Wageningen*. p. 19

**Calders, K.**, Newnham, G., Herold, M., Murphy, S., Culvenor, D., Raumonen, P., Burt, A., Armston, J., Avitabile, V. and Disney, M. (2013). Estimating above ground biomass from terrestrial laser scanning in Australian Eucalypt Open Forest. In *SilviLaser 2013*, 9-11 Oct. 2013, Beijing, China. October 9-11. p. 90-97.

Vaccari, S., **Calders, K.**, Herold, M., Bartholomeus, H. and van Leeuwen, M. (2013). Terrestrial laser scanning for 3D forest modeling and reflectance simulation through radiative transfer. In *SilviLaser 2013*, 9-11 Oct. 2013, Beijing, China. p. 18-25.

Armston, J., Newnham, G., Strahler, A., Schaaf, C., Danson, M., Gaulton, R., Zhang, Z., Burt, A., **Calders, K.**, Disney, M. et al. (2013). Terrestrial Laser Scanning International Interest Group (TLSIIG): Brisbane Instrument Intercomparison. In *SilviLaser 2013*, 9-11 Oct. 2013, Beijing, China.

Fedrigo, M., Minnis, B., Newnham, G., Culvenor, D., **Calders, K.**, Roxburgh, S., Smith, B., Kasel, S., Bennett, L. and Nitschke, C. R. (2013). Structural Variables from Lidar for Improved Carbon Estimates in Rainforest Understory. In *SilviLaser 2013*, 9-11 Oct. 2013, Beijing, China.

Vaccari, S., **Calders, K.**, Herold, M., Bartholomeus, H., van Leeuwen, M. and Coops, N. (2013). Terrestrial Laser Scanning for Forest Structural Parameters Retrieval and 3D Forest Modelling. In *ESA Living Planet Symposiom 2013*, 9-13 Sept. 2013, Edinburgh, UK.

Burt, A., Disney, M. I., Raumonen, P., Armston, J., **Calders, K.** and Lewis, P. (2013). Rapid characterisation of forest structure using TLS and 3D modelling. In *IEEE International Geoscience and Remote Sensing Symposium (IGARSS 2013)*, 21-26 July 2013, Melbourne, Australia. p. 3387-3390.

**Calders, K.**, Newnham, G., Armston, J., Goodwin, N., Culvenor, D., Muir, J., Fedrigo, M., Nitschke, C. R. and Herold, M. (2012). Using terrestrial LiDAR to asses structural diversity across multiple forest types in Australia. In *SilviLaser 2012*, 16-18 Sept. 2012, Vancouver, Canada.

Fedrigo, M., **Calders, K.**, Newnham, G., Culvenor, D., Kasel, S., Bennett, L. and Nitschke, C. R. (2012). Contribution of ALS and TLS to structural profiles of complex, multi-strata cool temperate rainforest. In *SilviLaser 2012*, 16-18 Sept. 2012, Vancouver, Canada.

**Calders, K.**, Lewis, P., Disney, M., Verbesselt, J., Armston, J., and Herold, M. (2012). Effects of clumping on modelling lidar waveforms in forest canopies. In *IEEE International Geoscience and Remote Sensing Symposium (IGARSS 2012)*, 22-27 July 2012, Munich, Germany. p. 3391-3394.

Newnham, G., Armston, J., Muir, J., Goodwin, N., Culvenor, D., **Calders, K.**, Johansen, K., Tindall, D., Pschel P. and Nyström, M. (2012). Terrestrial Laser Scanners for Vegetation Parameter Retrieval. In *FUNGIS 2012*, 6-8 June 2012, Cairns, Australia.

**Calders, K.**, Verbesselt, J., Bartholomeus, H. and Herold, M. (2011). Applying terrestrial LiDAR to derive gap fraction distribution time series during bud break. In *SilviLaser 2011*, 16-20 Oct. 2011, Hobart, Australia.

Vaccari, S., **Calders, K.**, van Leeuwen, M., Bartholomeus, H., Coops, C. C. and Herold, M. (2011). Terrestrial LiDAR as tool for forest structural assessment. In *3rd Remote Sensing Symposium*, 8 Sept. 2011, Wageningen, The Netherlands.

**Calders, K.**, Verbesselt, J., Bartholomeus, H. and Herold, M. (2011). Terrestrial LiDAR as tool for improved tree modelling. In *1st EARSeL Workshop on Operational Remote Sensing in Forest Management*, 23 June 2011, Prague, Czech Republic.

**Calders, K.** (2010). Modelling LiDAR waveforms to solve for canopy properties. *MSc thesis, University College London*. 98 p.

**Calders, K.** (2008). Texture analysis of high resolution QuickBird satellite imagery. *MSc thesis, Katholieke Universiteit Leuven*. 71 p.

# Short biography

Kim Calders was born in Leuven, Belgium on May 17, 1985. He spent his childhood in Herselt and attended primary school in the nearby village of Baal. He completed secondary school at Sint-Jozefscollege in Aarschot, focussing on science and mathematics.

Kim commenced a Bachelor of Science degree in Bioscience Engineering in 2003 at the Katholieke Universiteit Leuven in Belgium. Upon completion, he then undertook a Masters of Science in Bioscience Engineering, graduating in 2008. During his masters studies, Kim specialised in land and forest management and also did an Erasmus exchange at the University of Natural Resources and Applied Life Sciences in Vienna. His MSc thesis concerned texture analysis on QuickBird imagery, for which he collaborated with research centre CSIRO in Australia, and spent some months in Melbourne, Australia, as a visiting researcher.

Thereafter, Kim commenced working at the Spatial Applications Division Leuven as a GIS analyst. In September 2009, Kim received a NERC grant to commence a Masters of Science degree in Remote Sensing at University College London. His UCL MSc thesis, entitled Modelling LiDAR waveforms to solve for canopy properties, was chosen as the recipient of the award for Best MSc Thesis in 2011 from RSPSoc. After finishing his degree in London, Kim moved to Wageningen in October 2010 to start his PhD in terrestrial LiDAR remote sensing. Over the course of his PhD, Kim has built up expertise in 3D measurements in both a research and operational context for the monitoring of vegetation dynamics.

Kim's current research interests are related to measurements of full 3D vegetation structure and how this is related to airborne or spaceborne signals. This includes analysing point clouds for deriving structural information in the context of forest inventories, as well as using detailed 3D information to generate explicit tree models that can assist in the validation and calibration of satellite data through radiative transfer modelling.

# PE&RC Training and Education Statement

With the training and education activities listed below the PhD candidate has complied with the requirements set by the C.T. de Wit Graduate School for Production Ecology and Resource Conservation (PE&RC) which comprises of a minimum total of 32 ECTS (= 22 weeks of activities)


**Review of literature (6 ECTS)**

- Applying terrestrial LiDAR to measure vegetation characteristics and improve remote sensing monitoring applications

**Writing of project proposal (4.5 ECTS)**

- Applying terrestrial LiDAR to measure vegetation characteristics and improve remote sensing monitoring applications

**Post-graduate courses (3 ECTS)**

- Entrepreneurial boot camp; University of Wisconsin-Madison & WUR (2011)

**Laboratory training and working visits (4.5 ECTS)**

- Terrestrial LiDAR; CSIRO & DSITTA, Australia (2012)

**Invited review of (unpublished) journal manuscript (2 ECTS)**

- Remote Sensing of Environment: terrestrial LiDAR (2012)
- Methods in Ecology and Evolution: LiDAR for ecological applications (2013)

**Deficiency, refresh, brush-up courses (1.5 ECTS)**

- Learning Python, tutorial UCL (2011)

**Competence strengthening / skills courses (3.3 ECTS)**

- Scientific writing; WUR (2011)
- Techniques for writing and presenting scientific papers; WUR (2011)
- Career assessment; WUR (2014)

**PE&RC Annual meetings, seminars and the PE&RC weekend (1.5 ECTS)**

- PE&RC Weekend (2010)
- PE&RC Day: selling science (2010)
- $3^{rd}$ Remote sensing symposium; organising committee (2011)

**Discussion groups / local seminars / other scientific meetings (6.4 ECTS)**

- Spatial methods discussion group, SPAM (2010)
- Mathematics, statistics and modelling in production ecology and resource conservation discussion group, Maths & Stats (2010-2011)
- Ecological theory and application discussion group (2013-2014)
- Terrestrial laser scanning international interest group (2013-2014)

**International symposia, workshops and conferences (9 ECTS)**

- SilviLaser; oral presentation; Hobart, Australia (2011)
- $1^{st}$ EARSeL Workshop on operational remote sensing in forest management; oral presentation; Prague, Czech Republic (2011)
- IGARSS; oral presentation; Munich, Germany (2012)
- SilviLaser; oral presentation; Beijing, China (2013)
- Global vegetation monitoring and modelling; poster presentation; Avignon, France (2014)

**Lecturing / supervision of practicals / tutorials (3 ECTS)**

- Advanced earth observation, LiDAR module (2011, 2013)

**Supervision of MSc students**

- Virtual forests: terrestrial LiDAR as tool for improved tree modelling
- Comparing autonomous low cost sensors with terrestrial LiDAR for monitoring spring phenology